UNIVERSITY OF OKLAHOMA

GRADUATE COLLEGE

MODE-RECONFIGURABLE BANDPASS FILTERS WITH LIQUID

METAL ENABLEMENT

A THESIS

SUBMITTED TO THE GRADUATE FACULTY

in partial fulfillment of the requirements for the

Degree of

MASTER OF SCIENCE

By

SARAH MCCLUNG
Norman, Oklahoma
2017

MODE-RECONFIGURABLE BANDPASS FILTERS WITH LIQUID
METAL ENABLEMENT

A THESIS APPROVED FOR THE
SCHOOL OF ELECTRICAL AND COMPUTER ENGINEERING

BY

_____

Dr. Hjalti H. Sigmarsson, Chair

_____

Dr. Ziho Kang, Co-Chair

_____

Dr. Shahrokh Saeedi

Dedicated to Mom...

For showing me how to live unbounded

You are my inspiration

To my amazing roomies

My dog Alex for her company through the late nights

My husband Dmi for his continuous support to follow my heart

Acknowledgments

There are many I wish to thank who helped me work towards this thesis, starting with my committee members. Dr. Kang offered plenty of guidance, advice, and encouragement during my first year. His insight has continued to be extremely valuable throughout my experiences, and I am especially thankful to him for believing in my potential. Dr. Saeedi took the time to explain theoretical concepts, processes, and reasons why certain actions were done in the lab. He is a fantastic mentor whose time I could not appreciate more, and I know I share these thoughts with many students who cross his path. Finally, Dr. Sigmarsson is an inspiring professor who takes genuine interest in his students and makes their goals his priority. It always surprised me how quickly he could guide me in the right direction when I found myself stuck on a problem for too long. When I came to him I was lost and confused, but he offered great experiences, and opened many opportunities which gave me confidence in my future career choices. I am truly grateful to have spent time with them all and hope that one day I can be as knowledgeable and helpful to others.

I would like to thank my family and friends for the support and great memories during my time in Norman. Grandma and Grandpa, my three parents, Dmi, Alex, Omar, Michael, my aunts, and my cousins: thank you all for

giving me so much to look up to, and for the surprise visits and open doors. Dim, thank you so much for all of your help and support. Thank you to my new friends at OU and fellow members at the RIL, especially for helping with fabrication, LaTeX, and offering advice. I wish you all the greatest success.

Table of Contents

List of Tables

List of Figures

Abstract

The RF spectrum grows increasingly crowded every year due to technological advancement and more accessibility to wireless devices. Overcrowding leads to the desire for frequency agile microwave systems with dynamic spectrum access. One way to achieve this agility is by changing the frequency band of operation with mode-reconfigurable devices. This thesis presents three unique Butterworth bandpass mode-reconfigurable filters, designed to be enabled with the use of non-toxic Galinstan liquid metal. Galinstan is used to fill or empty certain vias and channels which change SIW cavity boundaries and external excitation to achieve reversible and repeatable operation. There are three states available in the filters within the C-band of 4-8 GHz: dual band, low band, and high band operation. To achieve low band operation by turning off the high band, a transmission zero is generated and centered over the high band resonant frequency. To achieve high band operation by turning off the low band, the first mode is shifted up to overlap with the second mode resonant frequency. The simulated and measured results showed that either band could effectively be turned off to allow multiband access or switching between the individual bands. The reconfigurable filters offer a promising technique for dynamic frequency access in future wireless systems.

Chapter 1

Introduction and Background

Microwave frequencies constitute the higher portion of the radio frequency (RF) spectrum from 0.3-300 GHz, encompassing many applications in communication, navigation, and sensing with the use of radars, antennas, and satellites. Within these applications, wireless communications is the most common, but there are a wide variety of others from environmental readings to medical imaging [1]–[4]. Although the RF spectrum is a renewable resource, it must be divided into different frequency bands to service these growing demands while avoiding interference. This regulation is realized by government agencies such as the International Telecommunications Union (ITU), which determines the allocations for worldwide usage of the spectrum [5]. Operating only within certain bands of the spectrum is made possible with microwave filters.

Microwave filters are used to achieve desired frequency-dependent characteristics and prevent unwanted electromagnetic signals, making them a necessary components of RF systems [1], [3], [4]. Figure 1.1 represents the RF spectrum frequency allocations of 3 kHz to 300 GHz in the United States, which is dense with a variety of applications. As the spectrum becomes more congested,

1

Figure 1.1: Frequency allocations in the U.S. with the area of interest circled (original image from [6])

filters with high selectivity are needed to limit the operational bandwidths and improve rejection at the cutoff frequencies [4]. Most frequency bands are also associated with licensing fees that are becoming more costly with demand, leading to further motivation for narrower bandwidths and steeper roll-offs [5]. However, even if desired frequency characteristics are met, it is common for systems to experience difficulty operating at certain frequencies for different reasons. Some reasons include atmospheric conditions, which greatly attenuate electromagnetic radiation at higher frequencies, large obstructions like mountains or skyscrapers that can block radiation, or connection overload when too many users attempt to access the same frequency band.

There are several options available for mitigating these problems with tunable or reconfigurable filters, which can be used to alter frequency characteristics. Many types of tunable filters exist, such as those with adjustable cutoff frequencies, center frequencies, bandwidths, passband responses, rejection rates, and filter orders [7]–[23]. The first tunable electronic filters seemed to emerge in the early 1960s with magnetically tunable filters [24]. The filters were used to produce a bandpass response, with the resonant frequency adjustable across the X-band with a varying DC field. Many tunable filter designs have followed, differing in types of structures and the methods used to tune them.

This thesis applies mode-reconfigurability for achieving tunable operation. Mode-reconfigurability is a tuning method that allows switching between available resonant frequencies by moving the passband operation to different frequency bands. Three unique mode-reconfigurable filters are presented, each designed for liquid metal to enable the switching of two frequency bands. The filters are realized with substrate integrated waveguides (SIWs) and operate within the C-band of the super high frequency (SHF) band, both emphasized in Figure 1.1. The following sections review previous work and provide relevant background information on filters, reconfigurable technology, and the role of liquid metal in microwave applications.

1.1 Electronic Filters

Electronic filters alter the frequency response of an input signal by passing certain frequencies to the output and attenuating the rest. There are two types of filters: active and passive. Both affect the frequency response of the

input, but active filters also amplify the input, or provide gain. For example, one electronic device that uses filtering to identify wanted signals are heart rate monitors. Initially, their sensors can detect many input signals in the body that occur at different frequencies, but with the use of filters, the noise can be attenuated leaving only the heartbeat which occurs within certain frequency and amplitude ranges. The applications of electronic filters are vast, but many lie in computers, power, audio, communication, and wireless systems. The next section provides a background review on the basic theory of filters.

1.1.1 Basic Theory of Filters

Filters are often analyzed by their frequency responses in terms of amplitude or gain, usually scaled in decibels (dB). They have passbands, where the input signal passes to the output at 0 dB, and stopbands, where the input signal is attenuated and minimized at the output. There are four common types of filters, represented in Figure 1.2: lowpass (LPF), highpass (HPF), bandpass (BPF), and bandstop (BSF) or band reject [25]. The frequencies where switching between passbands and stopbands occur are called cutoff frequencies (f_c). In the realistic representations, the cutoff frequencies are commonly defined at -3 dB. Bandpass and bandstop filters have center frequencies (f_0) as well which are centered between the cutoff frequencies.

Furthermore, filter responses are commonly displayed in terms of their scatter parameters (S-parameters), which represent EM wave behavior at the ports of a network [2]. Figure 1.3 shows a representation of a two-port network with incident, reflected, and transmitted waves. The network can be modeled
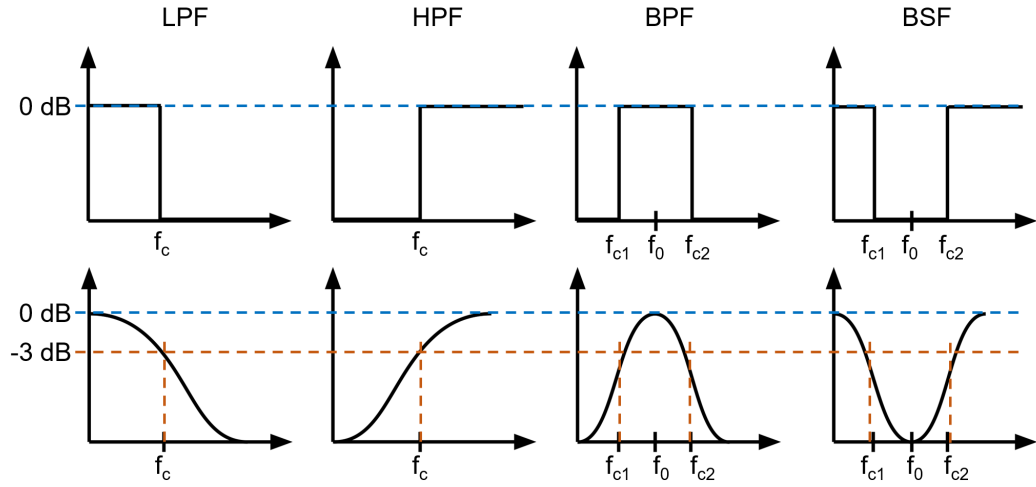
Figure 1.2: Filter categories with ideal (above) and realistic (below) representations
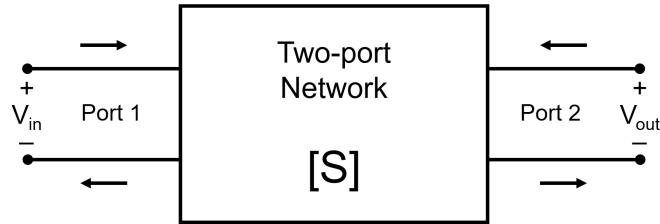
Figure 1.3: Two port network represented by an S-matrix

as an S-matrix, where

$$[S] = \begin{bmatrix} S_{11} & S_{12} \\ S_{21} & S_{22} \end{bmatrix}. \tag{1.1}$$

The S_{11} parameter represents what is received at port 1 from port 1, while the S_{21} parameter represents the signal received at port 2 from port 1. In other words, S_{11} represents the reflection and S_{21} represents the transmssion. In many cases, these two parameters are enough to analyze a two-port network, given that the S-matrix is reciprocal ($S_{21} = S_{12}$) and symmetrical ($S_{11} = S_{22}$). Results throughout this thesis are consistently evaluated by the S_{11} and S_{21} parameters, typically shown in blue and red, respectively.

There are also many different types of behaviors that filters can follow, two of which are compared in Figure 1.4 (made with [26]). Butterworth filters are known as maximally flat because they produce a smooth response in the passband, while Chebyshev filters have better roll-off behavior at the cutoff frequencies, but produce ripples in the passband [2]. Note that the cutoff frequencies of Chebyshev filters occur at the bottom of the passband ripple, but the responses in Figure 1.4 were aligned by their -3 dB points to clearly show the better roll-off, or steeper slope, in the Chebyshev filter. Elliptic filters are less common and more complex to design, but are similar to Chebyshev behavior with better roll-off. Bessel filters are known for relatively better phase response and have no ripple, but have worse roll-off than Butterworth filters.

All of the filter characteristics discussed are shown in Figure 1.5. An analog or digital (A/D) signal is inputted into a filter that is either passive or active, has one of the passband categories, and has a unique behavior such as Butterworth or Chebyshev. After passing through the filter, a corresponding A/D signal is outputted with a frequency response based on the filter characteristics.

Besides the type of filter, another common way to improve roll-off and reduce loss around the cutoff frequencies is by increasing the order. The order of a filter can be increased by cascading multiple filters together [25]. For example, one filter could produce a first-order response while four could create a fourth-order response. Figure 1.6 (made with [26]) shows the trend of an ideal Butterworth bandpass filter as the order increases; the slope becomes steeper resulting in less loss near the cutoff frequency and faster attenuation, making the response closer to ideal filter behavior.

Finally, transfer functions are used to mathematically represent filter re-
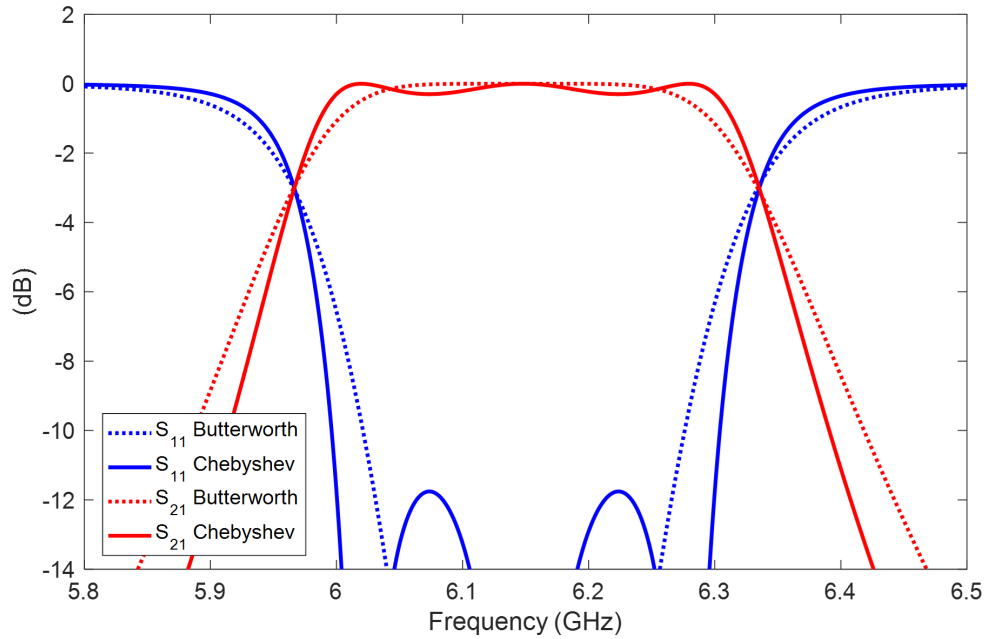
Figure 1.4: Comparison between ideal Butterworth and Chebyshev bandpass filter responses

sponses [25]. Typically, transfer functions are written in the frequency domain in terms of

$$s = j\omega, \tag{1.2}$$

where

$$j = \sqrt{-1}, \tag{1.3}$$

also represented by i (an imaginary number), and ω is frequency in radians per second (rad/s). The transfer function ($H(s)$) of a filter is equal to the output ($Y(s)$) over the input ($X(s)$), or

$$H(s) = \frac{Y(s)}{X(s)}. \tag{1.4}$$

Figure 1.7 shows a graphical representation of the transfer function. As filters
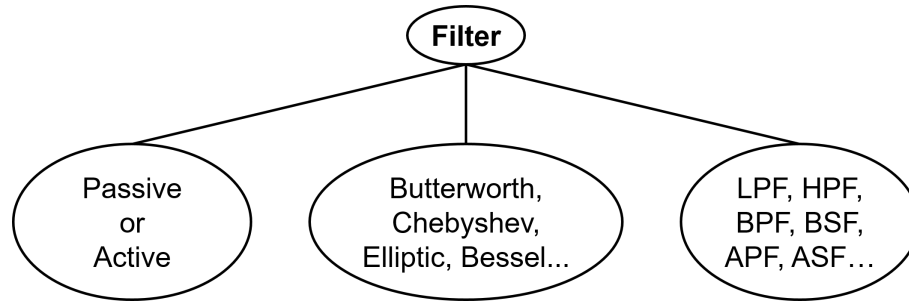
Figure 1.5: Filter characteristics block diagram

are cascaded and increase in order, the transfer function of each filter can be conveniently multiplied together in the frequency domain to find the total transfer function of the entire system.

This reviews the basic concepts of electronic filter theory, relevent to this thesis. The following section explores filters that operate in microwave frequencies with the ability to change their characteristics. These are often referred to as tunable or reconfigurable filters.

1.1.2   Reconfigurable Microwave Filters

Designing reconfigurable filters involves two levels: the circuit topology that affects the transfer function, and the tuning mechanism [7]. In other words, the type of filter must first be chosen. Microwave filters are usually made with coupled resonators since they handle high frequencies well. There are many types of resonators such as lumped element, transmission line, cavity, dielectric, and acoustic [2], [27]–[33]. Each have their own advantages and disadvantages, but cavity resonators are chosen in this work due to their relative simplicity and high quality factor. They are also known for high power handling capabilities, however that is not a requirement for the filters presented in this thesis. A series or parallel RLC circuit, shown in Figure 1.8 (made with

8
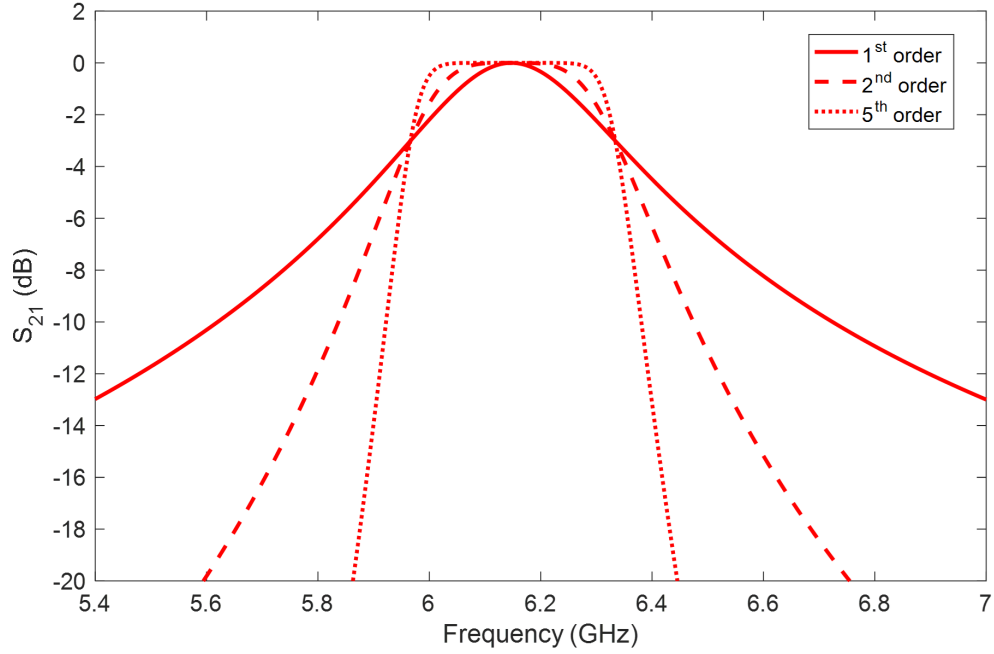
Figure 1.6: Ideal Butterworth bandpass response with different filter orders
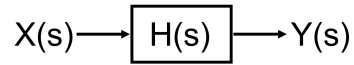
Figure 1.7: Transfer function representation in the frequency domain

[34]), can be used to represent a basic resonator with a center frequency of

$$\omega_0 = \frac{1}{\sqrt{LC}}, \tag{1.5}$$

where ω_0 is the resonant frequency in rad/s, R is resistance, L is inductance, and C is capacitance [2].

The filters in this thesis were designed as SIW structures for similar reasons. SIWs are implemented with a relatively simple planar fabrication process, and are known for high quality factor, linear behavior, and power capacity [19], [35]–[37]. Another advantage of SIW structures is durability because the
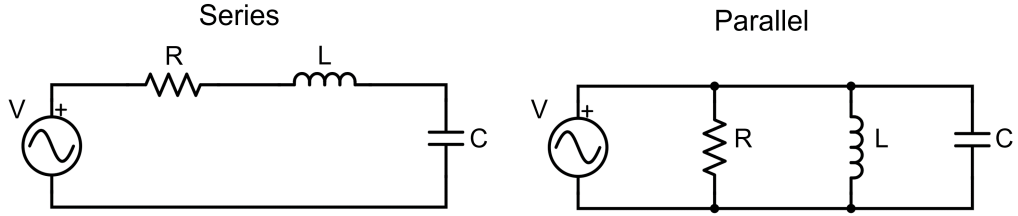
Figure 1.8: RLC circuits representing basic resonators
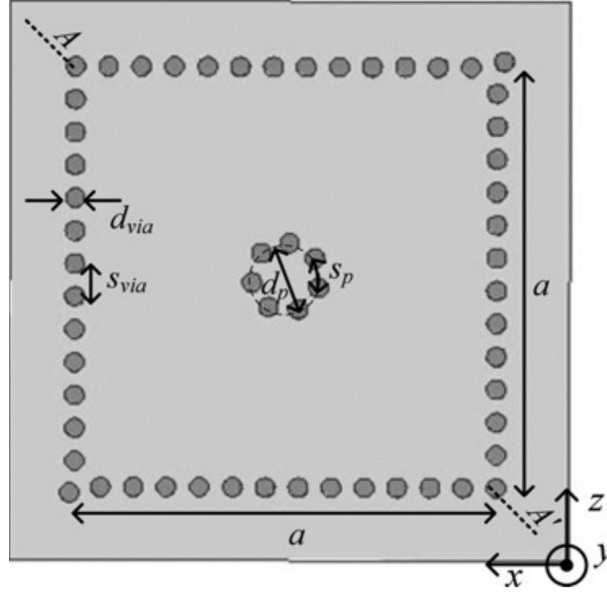
Figure 1.9: Example of a square SIW structure (from [39])

outside borders of the substrates can be any shape (such as rectangular), but the cavity walls can be abstract to outline the actual filter. The periodic metallic vias that construct the outside of the filter simply need to be close enough to block the EM waves from passing through, minimizing radiation loss. The diameter of the vias is recommended to be less than one fifth of the guided wavelength, and the gaps between the vias should be less than or equal to the diameter [38]. Figure 1.9 shows an example of an SIW structure, displaying the vias that construct the square cavity resonator boundary [39].

For the second aspect of reconfigurable filters, the tuning mechanism, many

different methods have been explored including p-i-n or varactor diodes, RF-MEMS switches, ferrite metamaterials, tuning screws, and microfluidics [19], [20], [24], [40]. Varactor diodes have been used to adjust the center frequency response or bandwidth of filters [8]–[11], [14], and capacitive loading posts have been used to change the center frequency [12], [13], [21]. Some tuning methods can affect several aspects; for example by changing an applied voltage in an acoustic resonator, the impedance, center frequency, quality factor, and coupling coefficient can each be tuned [15]. There are other unique methods such as using the optical pump power in a photonic filter to change the state [16], using an RF superconducting quantum interference device (SQUID) to alter the mutual inductance between two transmission line resonators which tunes the frequency [17], or using a shunt transmission line to change the coupling strength and quality factor in superconducting resonators [18]. A few examples of reconfigurable filters are shown in Figure 1.10. An example of a frequency-tunable SIW filter using lumped elements is shown in Figure 1.10(a) [41]. The coupled SIW cavity filter has a tunable passband center frequency. The filters in Figure 1.10(b) can be bandpass (BPF) or bandstop (BSF) with tunable center frequency, transmission zeros (TZs), and bandwidth (BW). Microfluidic techniques are growing in popularity as well following the discovery of nontoxic liquid metals, which are further discussed in the following section.

1.2 Room Temperature Liquid Metals

Selecting liquid metal as a tuning method has many advantages compared to those mentioned in the previous section. Liquid metal allows for continuous tuning, reversible and repeatable operation, flexible and stretchable devices,
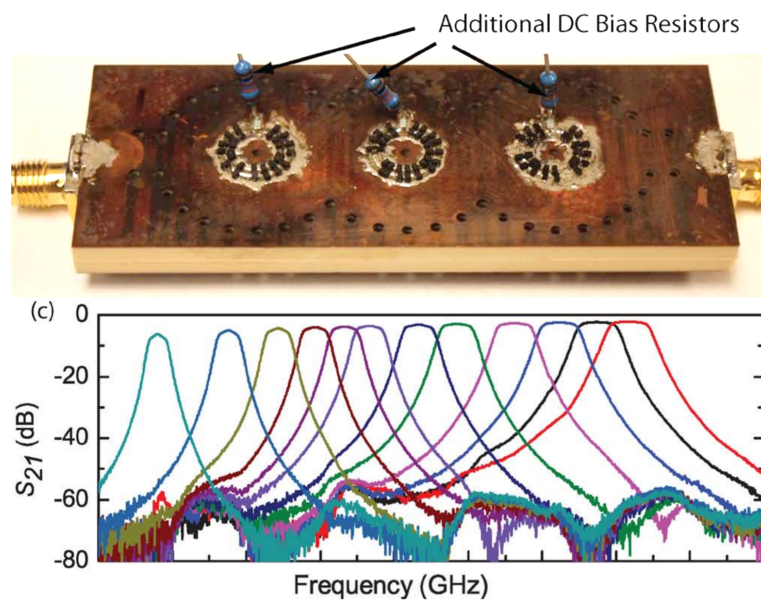
(a) Frequency-tunable SIW filter
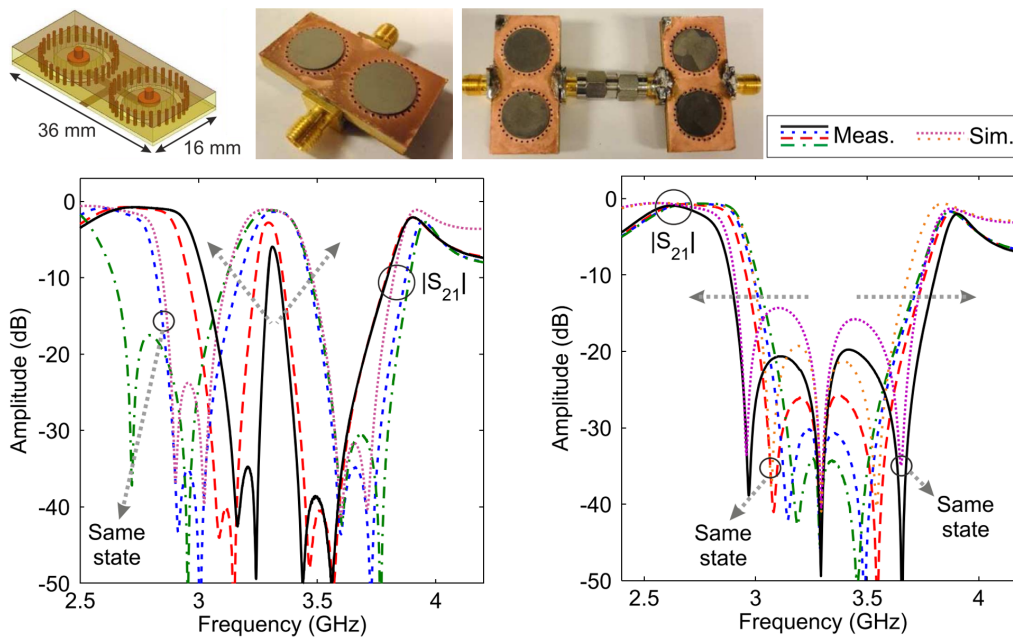
(b) BPF/BSF with tunable center frequency and BW

Figure 1.10: Examples of reconfigurable filters (from [41] and [23], respectively)

design simplification through minimizing the number of passive components, a possibly quicker fabrication process, and it has highly linear behavior [42], [43]. Yet despite the potential benefits of liquid metal in reconfigurable devices, for a long time mercury was the only standard option available. Its toxic properties made it a dangerous and undesirable choice compared to other tuning methods, and most believed the severe health risks of handling mercury were not worth the gains [44]. Mercury also has unusual properties that can make it difficult to integrate into certain applications. For example, at 25°C its surface tension is 0.426 N/m and its viscosity is 1.53 centipoise, which are relatively high compared to water which are 0.072 N/m and 0.89 centipoise, respectively [45]–[48].

After the discovery of nontoxic gallium-based liquid metals, such as eutectic gallium indium (EGaIn) and Galinstan (GaInSn), liquid metal tuning methods became more common and explorative [42], [43]. More research groups started incorporating these alloys into tunable and reconfigurable devices since they are much safer to handle [49]. However, gallium-based liquid metals come with challenges as well, specifically in terms of oxidation and corrosion.

The outer layer of EGaIn and Galinstan oxidize almost instantaneously when they are exposed to air [42], [50], and the oxidation layer has a much lower conductivity than the pure form of the alloy. If the layer is too thick or blocks the liquid metal from making direct contact with another metal, the functionality of the system can be compromised. Figure 1.11 shows a comparison between clean and oxidized Galinstan. When the metal is cleaner, it curves near the surface of the container because of the high surface tension. On the contrary, when the outer layer oxidizes, the metal becomes flat along the surface of the container. The oxide skin can also wrinkle and stick
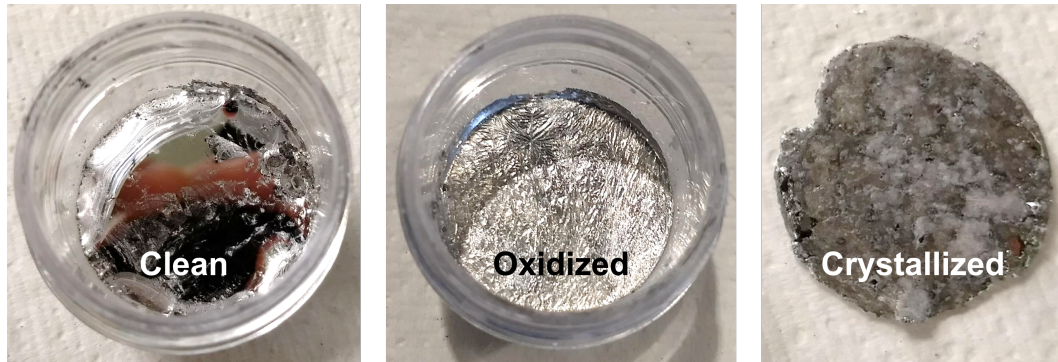
Figure 1.11: The appearance of Galinstan when clean, oxidized, or crystallized

to other surfaces. Another limitation of working with EGaIn or Galinstan is their reaction with other metals. In many research studies, the liquid metal must contact another metal to change the device configuration, but over long periods of time it eventually corrodes other metals such as copper [49]. Therefore, oxidation and corrosion must eventually be addressed when working with gallium-based liquid metals.

There are some strategies already known to address these challenges, or sometimes use them as advantages. To keep the liquid metal from oxidizing, a closed system can be constructed with certain carrier fluids. There are some electrolyte solutions that can remove the oxide layer with a reduction reaction, such as sodium hydroxide (NaOH) or hydrochloric acid (HCl) [37], [50], [51]. Applied voltage can then be used to add or remove the oxide layer, which is useful for several actuation methods [42]. However, liquid metal should not be stored in certain fluids for long periods of time because of the reactions that occur between both of them, and the oxygen in the air. An example of this reaction is shown in Figure 1.11 of a hardened crystallized layer that formed between Galinstan and NaOH after they were stored together for about six months. The hardened layer had to be removed from the top of the Galinstan
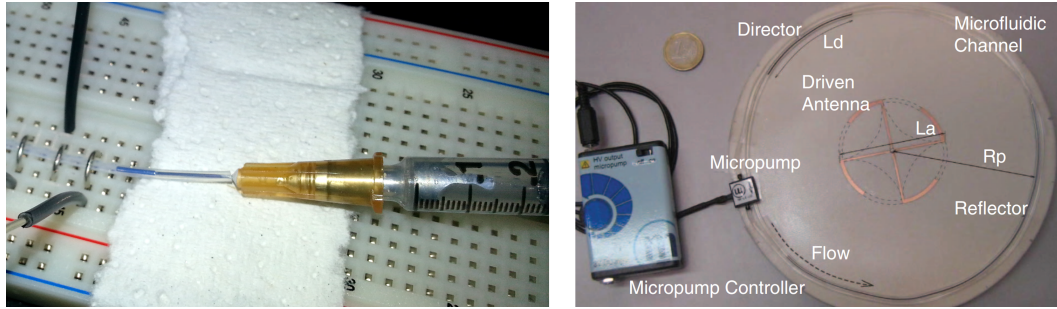
Figure 1.12: Moving liquid metal with a syringe or micropump (micropump from [63]), respectfully

to expose the clean liquid that remained underneath. In practice, crystallized Galinstan could block channels or degrade the electrical conductivity of the metal, which can be highly undesirable.

In terms of carrier fluids, there are gentler options available such as Teflon solution or oil to simply keep the liquid metal moving through channels without leaving residue behind [52], [53]. Finally, if the liquid metal must make contact with another metal, it is possible that corrosion may be mitigated by coating the surface of the solid contact [54]–[57], but types of conductive coatings that specifically protect against gallium-based liquid metals should be explored.

1.2.1 Actuation Methods for Gallium-Based Liquid Metals

The most basic form of moving liquid metal is with a syringe [42], [52], [58]–[60], which works for proof of concept, but is not reliable or practical enough for commercial applications. Micropumps are a better option since they support closed loop systems, increase automation, and are easier to control than manual injections. Many research groups incorporate micropumps into their designs as an alternative to manual injections [42], [61]–[64]. Examples of using manual injections or pumping to move liquid metal are shown in Figure 1.12.

15

Another option is applying voltage potentials to electrically actuate the liquid metal by using either surface oxidation, continuous electrowetting (CEW), or recapillarity [51], [65]–[69]. It should be noted that CEW depends on the electrocapillarity phenomenon, and recapillarity stands for reductive capillarity. Examples of each electrical actuation method are visually displayed in Figure 1.13. A detailed comparison is also shown between the methods in Table 1.1, where each method involves placing one probe in EGaIn and the other in NaOH [51]. Then a positive or negative voltage is applied, influencing the surface tension of the EGaIn. When the oxide layer is present, the surface tension of the metal is greatly reduced to near zero, and the metal wets to surfaces. When the oxide layer is removed, the surface tension becomes ten times higher than water and is less likely to stick to the surroundings. The metal has been shown to move through channels, withdraw out of channels into reservoirs, spill out of tubes, or gather as droplets at the end of tubes. Gravity is the dominant force during oxidation, and the surface tension of the liquid metal is the dominant force during reduction [70]. These electrical actuation methods are more automated, low voltage, and allow for more compact systems [51], [61], [71], [72], however they are currently in the early stages of research.

1.2.2   *Microwave Applications for Gallium-Based Liquid Metals*

Gallium-based liquid metals have been successfully integrated into different devices, many of them being antennas or filters [42], [73]. Monopoles or Yagi-Uda antennas have been made of Galinstan to tune frequency, gain, and beam steering by adjusting their lengths [63], [74]–[77]. Slot antennas have used Galinstan to control the length of the radiating aperture, or for capacitive load-
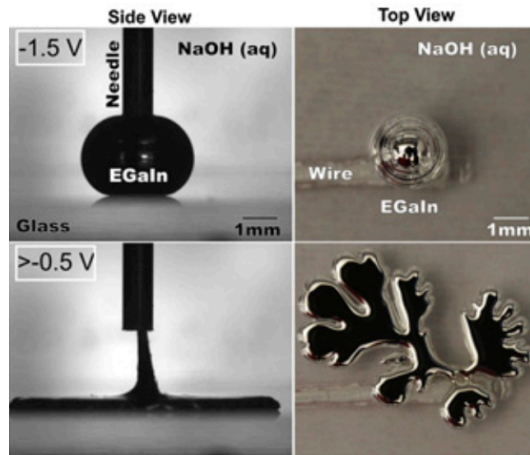
(a) Surface oxidation
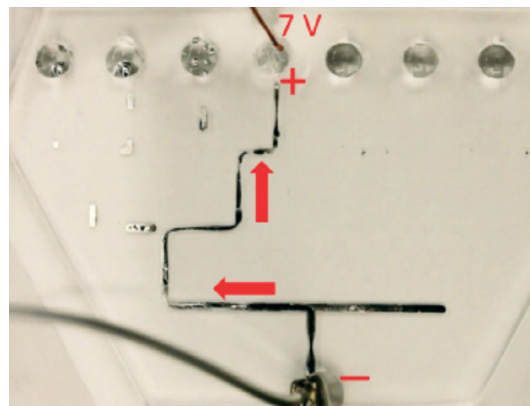
(b) CEW
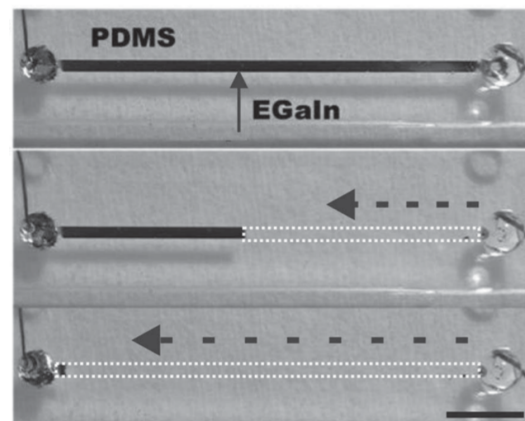
(c) Recapillarity

Figure 1.13: Electrical actuation methods for liquid metal (from [68], [51], and [69], respectively)

Table 1.1: Electrical Actuation Methods for EGaIn

	Surface Oxidation	CEW	Recapillarity
Set-up	Anode in EGaIn Cathode in NaOH Apply +V to EGaIn	Anode in NaOH Cathode in EGaIn Apply +V to NaOH	Anode in NaOH Cathode in EGaIn Apply -V to EGaIn
Surface Tension	Weak	Weak at interface	Strong
Results	EGaIn spreads or falls due to gravity	EGaIn flows toward anode	EGaIn withdraws from channels and forms sphere
Benefits	EGaIn stays connected	Low voltage requirements and quick movement	EGaIn retracts into reservoir

ing to tune frequency [58], [71], [78], [79]. In a flexible patch antenna, EGaIn made up the antenna itself and the ground plane then showed similar results in the relaxed or bent state [80]. Figure 1.14 shows the Yagi-Uda monopole, slot antenna, and flexible patch antenna, respectively. Many characteristics of the Yagi-Uda antenna could be tuned, but one plot of the unnormalized E-plane radiation patterns is shown with different numbers of parasitic elements. The plot of the slot antenna shows its center frequency ranging between approximately 2.5 to 2.9 GHz. Lastly, the performance of the patch antenna was tested at different radii of curvature, showing that although the return loss differed, the resonant frequency remained the same. This only reviews a few examples of many useful applications of gallium-based liquid metals integrated into antennas.

Regarding filters, EGaIn and Galinstan were commonly used to fill or empty vias that functioned as capacitive loading posts or SIW boundaries [37],
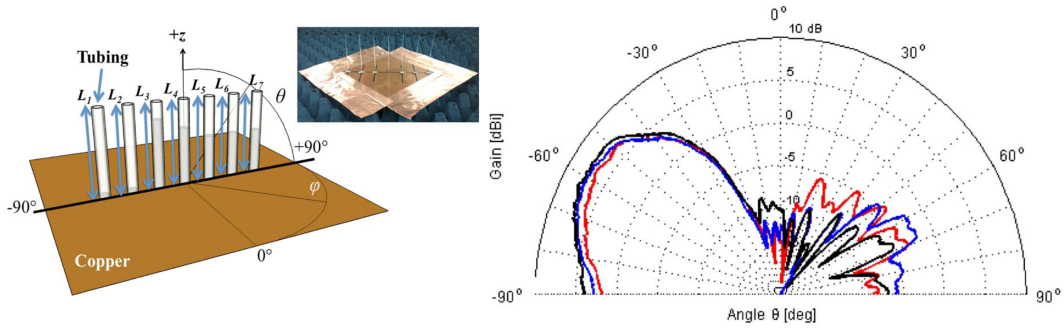
(a) Yagi-Uda monopole antenna with tunable frequency, gain, and beam steering
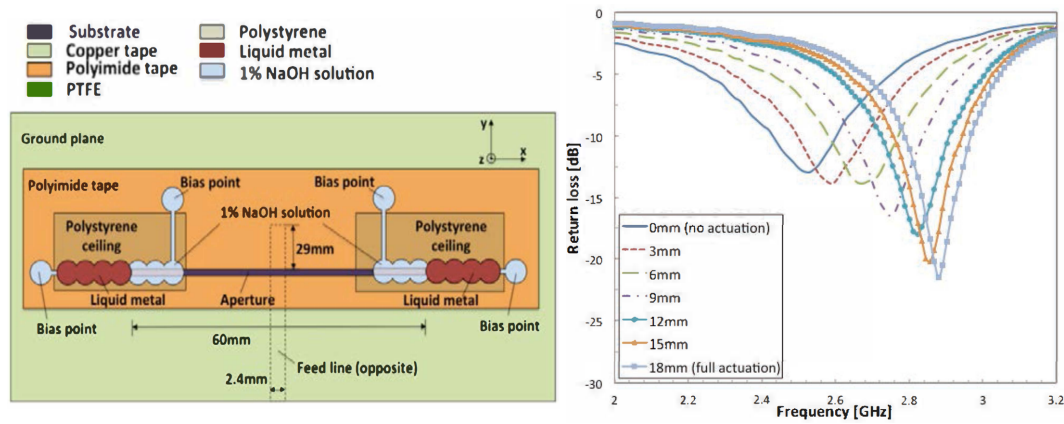
(b) Slot antenna with tunable frequency
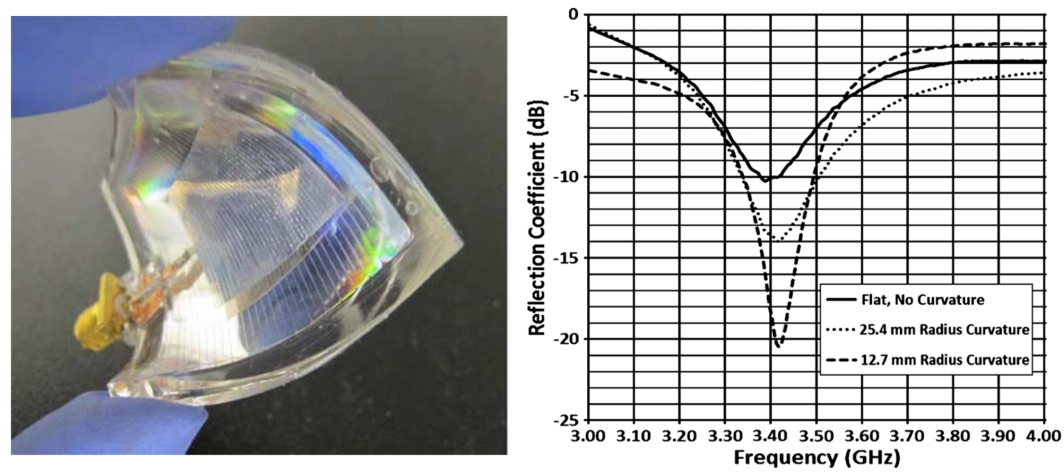
(c) Flexible patch antenna

Figure 1.14: Examples of antennas using gallium-based liquid metals with corresponding results (from [77], [71], and [80], respectively)

[81], [82]. Galinstan was used to fill or empty a defective ground structure to change the cutoff frequency of a lowpass filter [83], [84]. Galinstan was also used to tune a frequency selective surface in the X-band with a second-order bandpass filter response [85]. One implementation constructed stacked resonators for a bandpass filter with tunable frequency, where the top resonator border was completely made of Galinstan [86]. Another design incorporated EGaIn to fill posts that acted as impedance inverters and switched the state of a filter between bandpass and bandstop, or tuned a transmission zero (TZ) [87]. Galinstan was even used to load metallized plate resonators to construct a frequency tunable fourth-order Chebyshev bandpass filter [61]. Some of these examples are displayed in Figure 1.15 with their corresponding results.

In a more basic sense, gallium-based liquid metals have been used as wires, contacts, or switches. EGaIn was injected into ultrastretchable fibers and remained connected and conductive during and after stretching [88]. The self-healing property of gallium-based metals is also beneficial because if it is bent or disconnected it can be reconnected without wearing out, unlike solid metals [89]. Despite the high surface tension and low viscosity, EGaIn has been 3D-printed into different structures due to its microscopic oxide skin. It has been printed into wires, structures out of stacked droplets, and abstract shapes using molds, as shown in Figure 1.16 [90]. EGaIn and Galinstan have demonstrated many possible uses in high frequency electronic applications, and more are being explored. Based on the previous research presented, both liquid metals are promising tuning mechanisms to incorporate into reconfigurable microwave filters.
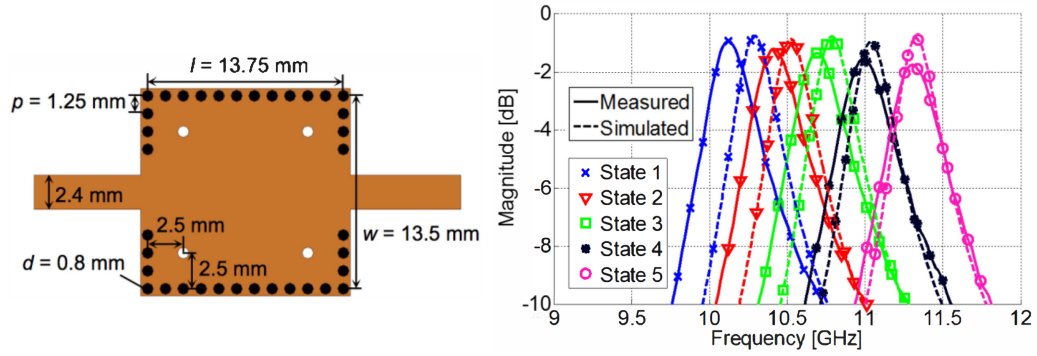
(a) SIW bandpass filter with tunable frequency
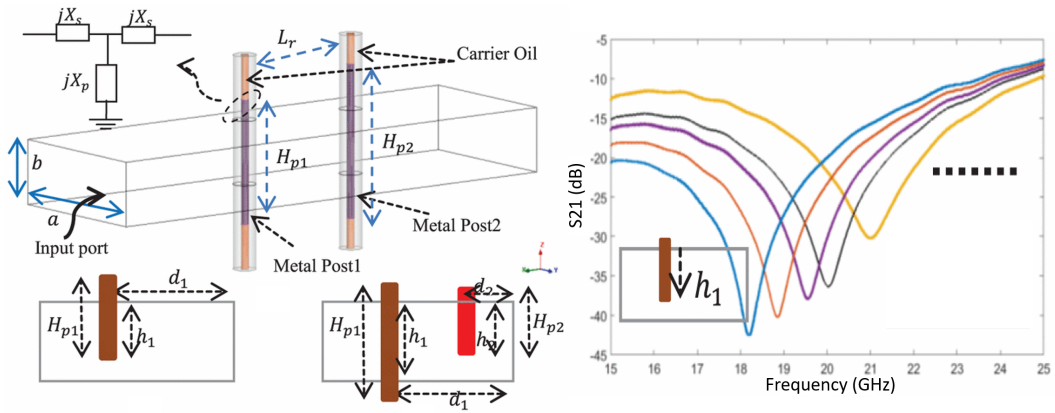
(b) Bandpass to bandstop filter with tunable TZ
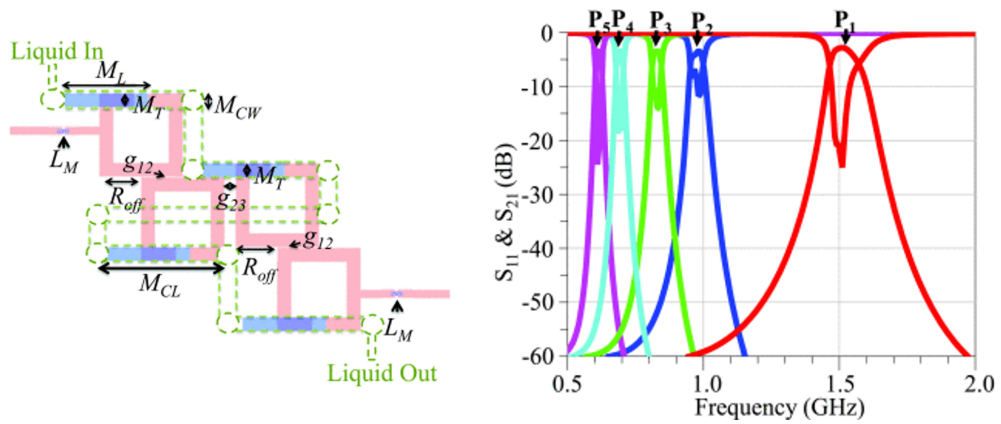
(c) Fourth-order bandpass filter with tunable frequency

Figure 1.15: Examples of filters using gallium-based liquid metals with corresponding results (from [37], [87], and [61], respectively)
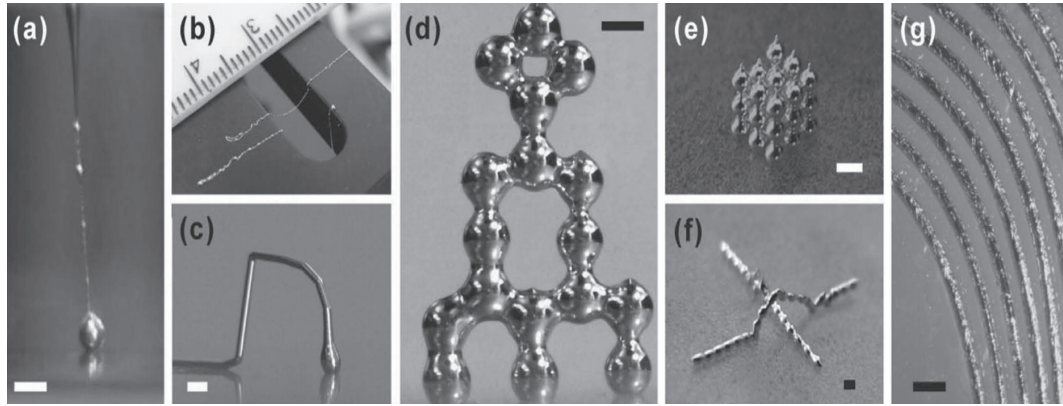
Figure 1.16: 3D-printed EGaIn structures (from [90])
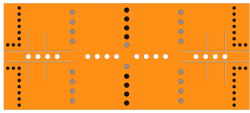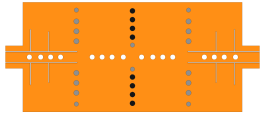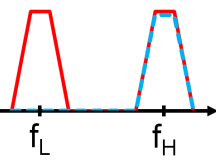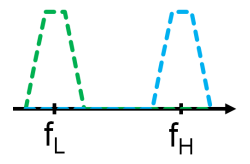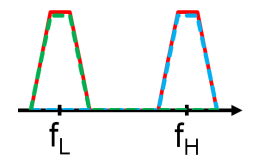
1.2.3 Galinstan Liquid Metal

Between the two gallium-based liquid metals discussed in the previous sections, Galinstan was chosen over EGaIn to manipulate the filters in Chapters 3-5 because of the low melting point. The melting point of EGaIn is only 15.5°C, which is easily attainable and not dramatically far from room temperature [50], while Galinstan has a much lower melting point of -19°C. Galinstan is a nontoxic liquid metal alloy that commonly consists of 68.5% gallium, 21.5% indium, and 10% tin, made by heating the ratio of metals to 100°C in a beaker and mixing them with a magnetic stirrer [43], [91], [92]. The metal has a boiling point of over 1300°C and an electrical conductivity of 2.3×10^6 S/m to 3.46×10^6 S/m in its pure state [43], [91], [93]. Although Galinstan is able to handle high temperatures, its properties make it a convenient choice for room temperature microwave applications, exceeding the requirements of the low power filters in this thesis.

1.3   Thesis Overview

The purpose of this thesis is to present mode-reconfigurable filters that allow dynamic spectrum access, in the case that one frequency band experiences issues such as overcrowding. Galinstan liquid metal is chosen to change the configuration of three unique bandpass filters operating in the C-band of 4-8 GHz, therefore Chapter 2 tests how Galinstan performs compared to copper with monopole antennas. Chapter 3 presents the first implementation of a mode-reconfigurable filter that switches between dual band and high band operation. The next two chapters implement higher-order filters; Chapter 4 demonstrates a low to high band filter and Chapter 5 combines all the configurations of dual, low, and high band operation. Table 1.2 shows a comparison summary of the three mode-reconfigurable filters. There are three different types of vias in the filter layout row represented as circles: white are empty, black are copper plated, and gray are either empty or filled with Galinstan and used to enable switching between configurations. In the frequency response row, red represents the dual band, blue-dashed represents the high band, and green-dashed represents the low band. All of the simulations were executed using ANSYS High Frequency Structure Simulator (HFSS) software [94] prior to fabrication and testing. Lastly, Chapter 6 concludes with a summary and discussion on the future direction of the work presented.

Table 1.2: Summary of Filters Presented

	Ch. 3: Dual to High Band	Ch. 4: Low to High Band	Ch. 5: Dual to Single Band
Filter Layout			
Freq Response			
Filter-Order	Dual band: 1st Low band: N/A High band: 2nd	Dual band: N/A Low band: 2nd High band: 4th	Dual band: 2nd Low band: 2nd High band: 4th
Benefits	Smaller size	Higher-order, sturdier structure, equal fractional bandwidths	Higher-order, includes all configurations

Chapter 2

Monopole Antennas with Liquid Metal

2.1 Introduction

Antennas are transducers most commonly used for communication applications that can transmit and/or receive wireless RF signals. Antennas convert between EM waves on guided transmission lines and EM waves that travel through unbounded media [2], [95], [96]. There are many types of antennas, but the dipole antenna is widely considered to be one of the most fundamental.

The dipole consists of transmission lines (T-lines) with both ends bent outwards $90°$ for a total length of l_d, as shown in Figure 2.1. For a half-wave dipole,

$$l_d = \frac{\lambda}{2},\tag{2.1}$$

where λ is the wavelength [95]. The transmission lines are fed alternating current (AC) so that the top and bottom portions of the dipole have current moving upwards that add in phase, as indicated in Figure 2.1. Since the endpoints of the antenna are open-circuited, the current is zero at the ends
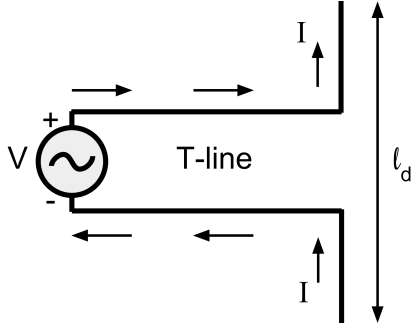
Figure 2.1: Representation of a dipole antenna

and maximized at the center. According to Ohm's law,

$$Z = \frac{V}{I},$$ (2.2)

where Z is impedance, V is voltage, and I is current [95]. Therefore, maximizing the current at the center of the dipole can minimize the imaginary part of the impedance. This makes the antenna purely resistive and causes it to radiate from the center. The half-wave dipole radiates at $\lambda/2$ and at every other consecutive cycle, such as $3\lambda/2$, $5\lambda/2$, and so forth. Considering that

$$\lambda = \frac{c}{f},$$ (2.3)

where c is the speed of light taken as 299,792,458 m/s, and f is the frequency in Hz, each resonant frequency of the antenna can be calculated.

The concepts of a dipole antenna can be used to explain a monopole antenna. A quarter-wave monopole antenna has a length of l_m, where

$$l_m = \frac{l_d}{2} = \frac{\lambda}{4}.$$ (2.4)

By applying image theory, the quarter-wave monopole resembles the behavior

of a half-wave dipole. Image theory states that a power source placed above a perfectly conductive infinite ground plane is electrically equivalent to the source combined with its image [95]. This phenomenon is due to the reflection of waves above the ground plane. In the case of electric current, if an upwards electric current is placed above the ground plane, it produces an image of an upwards electric current below the ground plane [2], [96]. Therefore, the quarter-wave monopole antenna is electrically equivalent to the half-wave dipole antenna above the ground plane, in certain aspects. A comparison of the antenna cross-sectional radiation patterns are shown in Figure 2.2. The antennas are represented as lines with the radiation originating from the centers to make ring-shaped patterns, after considering the 360° rotation. Since the bottom portion of the monopole is an image, the radiation only exists above the ground plane.

There are a few trade-offs between dipoles and monopoles. Dipole antennas radiate in twice as much space as monopoles, therefore they have double the input impedance, half the directivity of monopoles, and are double the size of monopoles. One challenge with monopoles is that they are not realistically placed on infinite ground planes. This causes non-ideal values in practice. The radiation pattern of monopoles on finite ground planes also bend upwards, changing the directivity.

A single monopole antenna is simple to construct compared to many other microwave devices. Therefore, monopoles were chosen to conduct several experiments, and the results were compared to simulations in HFSS. First, the performance of Galinstan liquid metal was compared with copper, which is a common metal used for antennas. Then a tunable Galinstan monopole was tested to observe the performance of the liquid metal across the C-band.
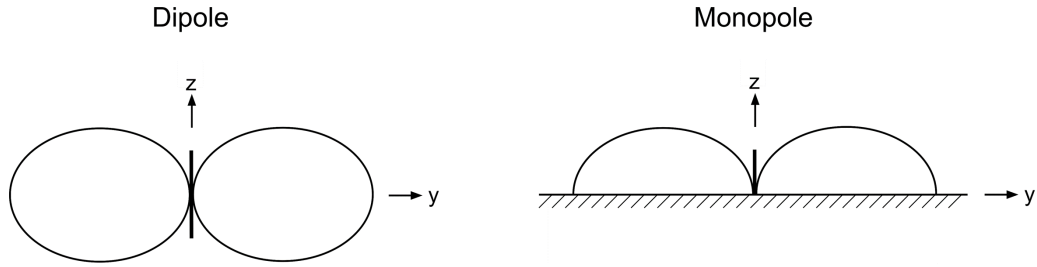
Figure 2.2: Cross-sectional representation of antenna radiation patterns
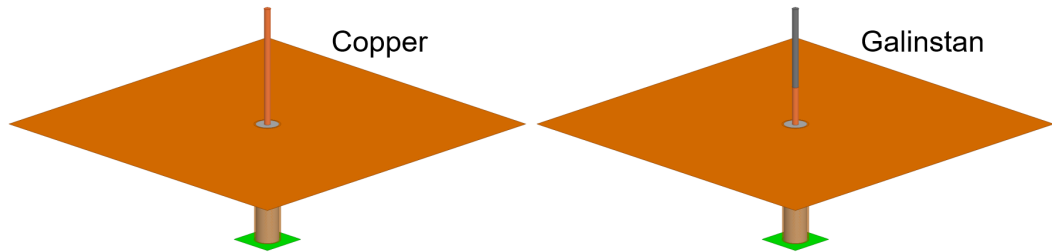
Figure 2.3: Copper and Galinstan monopole antenna structures

2.2 Simulation and Experimental Results

2.2.1 Copper vs. Galinstan Monopole Antennas

A simulation for comparing the performance of Galinstan with copper was created in HFSS. Since Galinstan was not an available material in the software, the electrical properties of Galinstan were stored to define a custom material. Two monopoles were constructed as shown in Figure 2.3, and their S_{11} parameters were checked around the fundamental frequency. Ideally, S_{11} should approach negative infinity at the resonant frequency. This indicates no reflection where the antenna radiates, but that does not occur in reality. In this set-up, a return loss of at least 10 dB was considered acceptable.

The monopole antennas were designed for a fundamental center frequency of 3.3 GHz. By applying (2.3) and (2.4), the desired lengths were calculated to be 23 mm long. However in practice, the monopole lengths were slightly
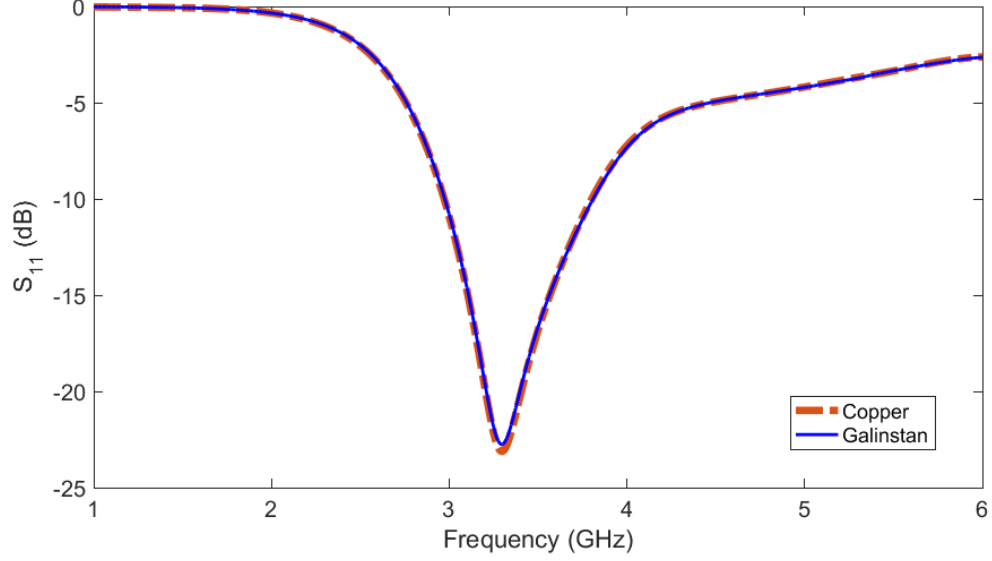
Figure 2.4: Simulated results of the copper and Galinstan monopole antennas

decreased to 0.23λ, or 21 mm, which raised the frequencies closer to the goal. There were several non-ideal aspects that contributed to the need for shorter lengths, such as the finite ground planes and the non-zero antenna diameters. The ground planes were also defined as copper instead of perfect electric conductors (PECs), resulting in less conductivity and therefore less reflection. If the ideal antenna length is used, it can cause an impedance mismatch at the ground plane, resulting in an antenna that is not purely resistive at resonance [97]. The need for the length adjustment was confirmed by observing the S_{11} parameters in Figure 2.4. The simulations resulted in the desired resonant frequencies of 3.3 GHz for both the copper and Galinstan monopoles.

To test the simulation results, three monopoles were used and are shown in Figure 2.5. Two of the antennas were copper (labeled Cu1 and Cu2) and the third was Galinstan (labeled Gal), as indicated in Figure 2.5(a). They each had the same total length, and the distance between Cu1 and Cu2 equaled

the distance between Cu1 and Gal. To set up the monopoles for experimental measurements, the copper antennas were made of 1 mm diameter wires that were cut to the desired lengths. However, the Galinstan antenna required a Teflon tube to vertically contain the liquid metal. To accomplish a stable structure for the Galinstan antenna, copper wire was cut to 7 mm and a Teflon tube was slid over the wire, as shown in Figure 2.5(b). A syringe was placed into the tube to fill it with Galinstan so that the total height of the antenna equaled the height of the copper monopoles. This explains why the Galinstan antenna in Figure 2.3 was created with a bottom copper portion, so that the simulation would closely match the realistic experiment. The set-up allowed for continuous electrical contact at the boundary between the copper and Galinstan, and for stable tube support.

Measurements were taken with a network analyzer and compared to the Galinstan simulation from Figure 2.4. Since the copper and Galinstan simulations were almost identical, only the Galinstan simulation was used for the comparison, which is shown in Figure 2.6. The experimental results are labeled in the legend and the simulation is marked in blue.

The simulated results showed 23 dB return loss at resonance, while the measured results showed approximately 15 dB return loss. The simulations indicated less reflection, but all of the results had more than 10 dB return loss, as desired. According to the simulations, the Galinstan monopole produced almost identical results as the copper monopole, despite the lower electrical conductivity of Galinstan. This was consistent with the measured results where Cu1, Cu2, and Gal produced similar output signals at the resonant frequency. Overall, the differences between the copper and Galinstan monopole antennas were insignificant.
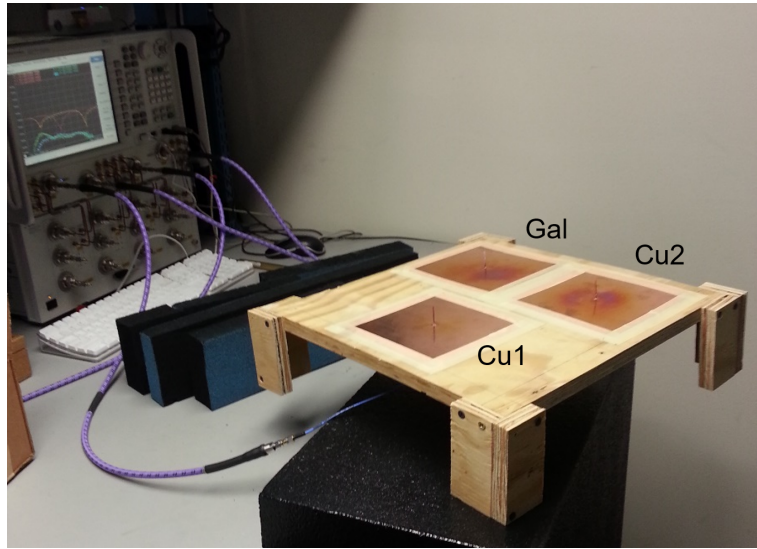
(a) Copper (Cu1 and Cu2) and Galinstan (Gal) monopole antennas
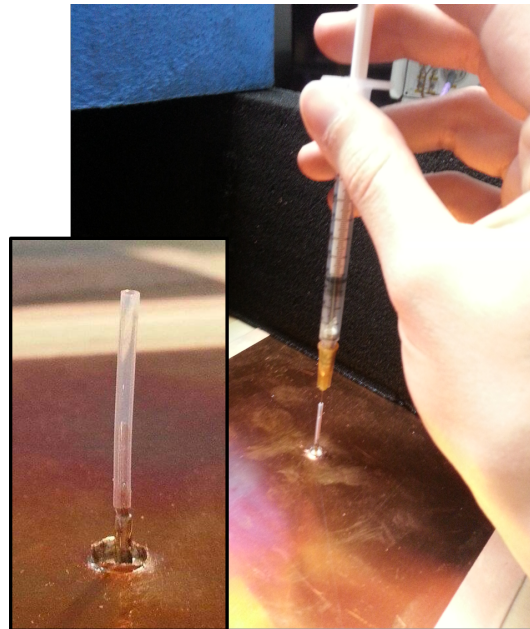
(b) Galinstan monopole antenna

Figure 2.5: Experimental set-up of two copper antennas (Cu1 and Cu2) and one Galinstan antenna (Gal) with close-ups of the Galinstan monopole
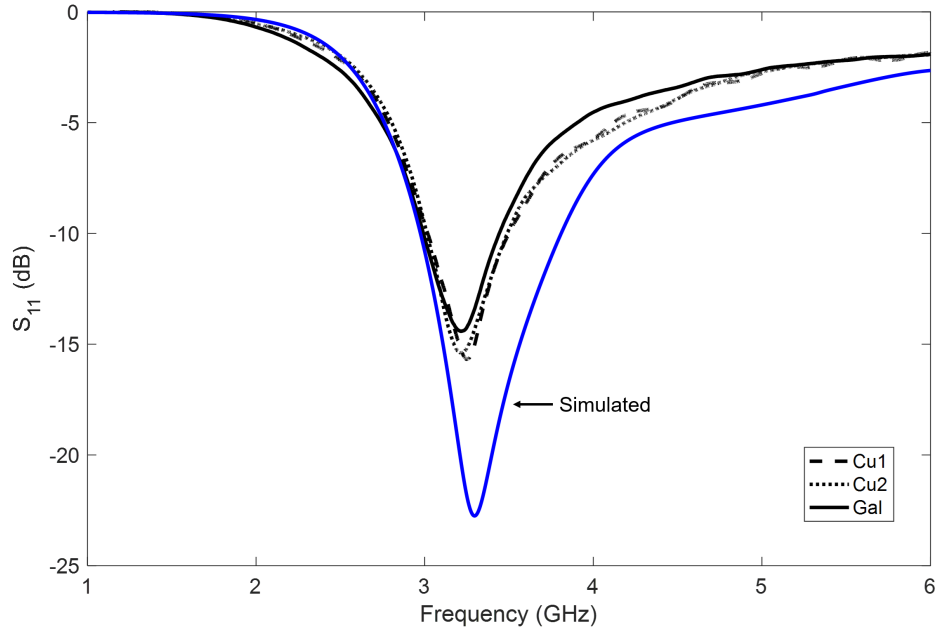
Figure 2.6: Simulated (blue) and measured (black) results of the copper (Cu1 and Cu2) and Galinstan (Gal) monopoles

2.2.2 *Tunable Galinstan Monopole Antenna*

The Galinstan antenna was ranged to four different lengths to tune its frequency from 2.5 to 8 GHz. The simulated and measured results are compared in Figure 2.7, and are in good agreement. The discrepancies between the simulated and measured results were mainly due to the imperfect experimental lengths resulting from manual injections of the Galinstan with a syringe. However, the comparison of the four fundamental frequencies are closely aligned. Consistent with (2.3) and (2.4), as the length of the antenna was increased, the resonant frequency decreased.

The experimental set-up was also used to calculate the gain of the Cu2 copper and Galinstan antennas since they were each an equal distance away from the Cu1 copper antenna. The gain was extracted from the transmission
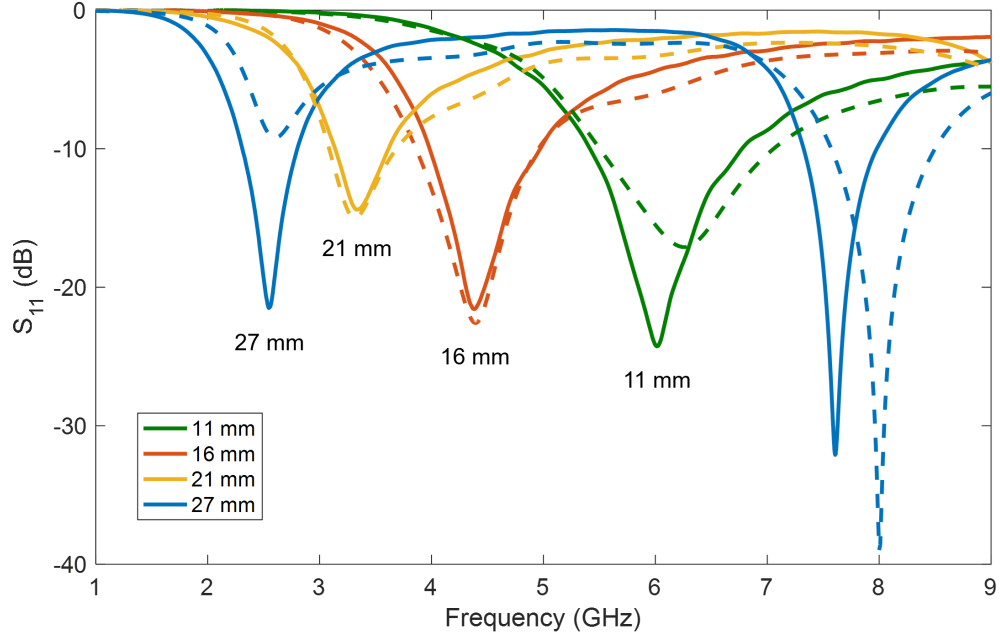
Figure 2.7: Galinstan monopole simulated (dashed) and measured (solid) results at different lengths

to the antennas received from Cu1, and by applying Friis equation from [2]:

$$\frac{P_r}{P_t} = G_t G_r \left(\frac{\lambda}{4\pi R}\right)^2,\qquad(2.5)$$

where P_r is the power received, P_t is the power transmitted, G_r is the gain received, G_t is the gain transmitted, and R is the distance between the antennas. The gain of the copper antenna was calculated as 2.632 dB and the gain of the Galinstan antenna was calculated as 1.162 dB. Therefore, the Galinstan antenna received 71.3% of the gain that was received by the copper antenna.

2.3 Conclusion

Since Galinstan was chosen to enable the switching of the mode-reconfigurable filter designs in Chapters 3-5, the performance of the liquid metal was com-

pared with copper. The electrical conductivity of Galinstan is significantly lower than copper, which can lead to concern in choosing Galinstan as an acceptable substitute for copper. However, the simulated and measured results of monopole antennas showed almost identical output signals from both metals in terms of the S_{11} parameters. A tunable Galinstan monopole antenna was also tested between 2.5 to 8 GHz, since the filters in Chapters 3-5 were designed to operate in the C-band. The measured results of the tunable Galinstan monopole were in good agreement with the simulated results after comparison at four different antenna lengths. Therefore, considering that the Galinstan monopole performance was similar to copper, and after testing its functionality across the C-band, it was recognized as a suitable replacement for copper for integration into the mode-reconfigurable filters.

Chapter 3

Dual to High Band Bandpass Filter with Liquid Metal

3.1 Introduction

The dual to high band bandpass filter is a mode-reconfigurable Butterworth filter that allows control of the low band by effectively turning it on or off. By applying mode-shifting to the low band, the first resonant frequency is increased until it occurs at the second resonant frequency. This design was initially presented in [98], where it was called the single-mode-dual-band (SMDB) to dual-mode-single-band (DMSB) bandpass filter. The filter was called SMDB when the first mode was on, resulting in two passbands, and it was called DMSB when the first mode was off, resulting in one passband of higher-order. In this thesis, the designs supporting the two operational states are referred to as dual band configuration (DBC) and high band configuration (HBC) instead. The filter is realized in a single square cavity resonator, and to achieve mode-shifting certain vias are filled with Galinstan liquid metal. Filling the vias switches the first-order square filter to a second-order filter made of two triangular SIW cavities coupled together.
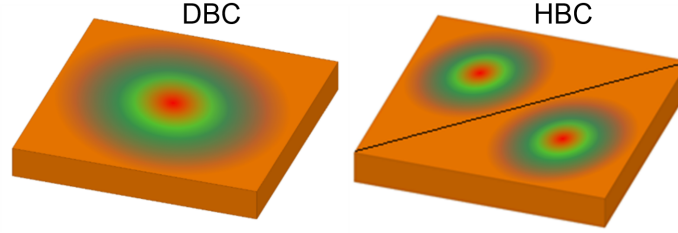
Figure 3.1: E-field distribution representation of the DBC and HBC

3.2 Theoretical Concepts of Mode-Shifting

The electric field (E-field) distribution of both configurations is represented in Figure 3.1, where the E-field is at its maximum in the red area. The DBC is a square cavity resonator, or first-order filter, with the strongest point of the E-field in the center. The HBC uses vias along the diagonal line to split the resonator into two triangular SIW cavities, which resembles the second mode of the square cavity. It therefore becomes a second-order filter with cavities that are half the original size.

The first step in designing the cavity is to use

$$f_{mnp} = \frac{c}{\sqrt{\epsilon_r \mu_r}} \sqrt{\left(\frac{m}{a}\right)^2 + \left(\frac{n}{b}\right)^2 + \left(\frac{p}{d}\right)^2} \tag{3.1}$$

to determine the size, where f is frequency, c is the speed of light, ε_r is the relative permittivity, μ_r is the relative permeability, m, n, and p represent the mode number, and a, b, and p represent the cavity dimensions [95]. A Rogers TMM3 substrate was chosen as the dielectric ($\varepsilon_r = 3.27$, $\mu_r = 1$, $\tan(\delta) = 0.002$ at 10 GHz) with a thickness of 3.175 mm. Since the frequency range of interest is across the C-band, the first two frequency bands should be between 4-8 GHz. Therefore, the cavity dimensions chosen were 25 x 25

x 3.175 mm³. This results in the first five modes as follows: the first mode is TE₁₀₁ at 4.69 GHz, the second and third modes are TE₁₀₂ and TE₂₀₁ at 7.42 GHz, and the fourth and fifth modes are TE₁₀₃ and TE₃₀₁ at 10.5 GHz. This meets the specifications since only the first two frequency bands should be in range; the remaining modes exceed 8 GHz, as they should.

After choosing the dimensions of the cavity, Eigen-mode simulations were checked in HFSS to study the E-field distribution of each configuration, displayed in Table 3.1. The first three rows show the E-field pattern inside the cavity at the first three resonant modes. In the last row, a depiction of the frequency response from 4-8 GHz is sketched.

The first column shows a basic unperturbed square cavity with two resonant frequencies, as expected. The second and third columns show different versions of the DBC design, which should imitate the unperturbed cavity. However, they imitate different aspects; the second column displays the same E-field pattern, and the third column displays the same frequency response. The second column has six air vias placed diagonally across. Based on the perturbation method, perturbing the cavity with a different material causes a shift in resonant frequency [39], indicated by

$$\frac{\omega - \omega_0}{\omega_0} \simeq \frac{\int_{\Delta V}(\mu|\overline{H}_0|^2 - \varepsilon|\overline{E}_0|^2)dv}{\int_{V_0}(\mu|\overline{H}_0|^2 + \varepsilon|\overline{E}_0|^2)dv}, \tag{3.2}$$

where ω is the resonant frequency of the perturbed cavity, ω_0 is the resonant frequency of the original cavity, ΔV is the change in volume, V_0 is the original cavity volume, μ is the magnetic permeability, ε is the electric permittivity, H_0 is the H-field (magnetic field) of the original cavity, and E_0 is the E-field of the original cavity [2]. The approximate change in resonant frequency can
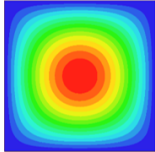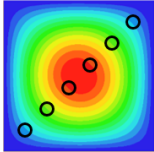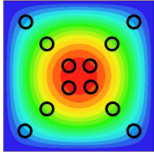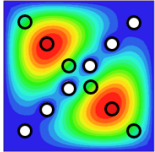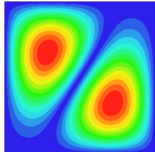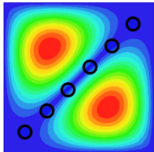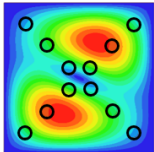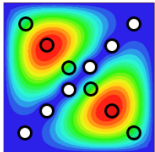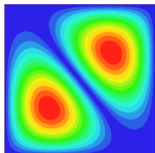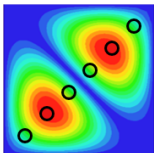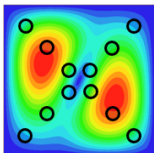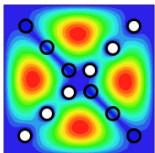
be calculated with (3.2) based on knowing the characteristics of the original cavity and change in volume, since the characteristics of the perturbed cavity are often unknown [2].

The perturbation method explains why the second and third modes slightly separate in the frequency response of the second column. The second mode is not affected by the vias because they are located where the E-field is minimum, but the third mode is affected and shifts up in frequency, causing pole splitting in the high band. Although the E-field pattern imitates the unperturbed cavity, the mode splitting in the second frequency band must be addressed. Therefore, six more vias were added that mirror the original six to make the cavity design symmetrical.

As shown in the third column, this solves the problem and the second and third modes overlap to imitate the unperturbed cavity. Modes that overlap and share the same frequency are referred to as degenerate modes. With twelve vias, the second and third modes become degenerate and match the unperturbed cavity frequency behavior, as desired. It can be observed that the E-fields in the second and third modes slightly rotate compared to the E-field patterns in the unperturbed cavity, but the rotation does not cause a negative effect. Since the frequency behaves as desired, the E-field rotation is not a concern. Lastly, the fourth column tests the HBC behavior by filling a line of vias with liquid metal. The first and second modes should resonate like the second mode in the DBC high band, which is observed. The third mode becomes irrelevant because it resonates above 10 GHz and is therefore out of range.

The response of the HBC can also be explained by the perturbation method because the first mode frequency is increased to the second mode frequency.

Table 3.1: E-Field Distribution of Cavities for Dual to High Band Filter

	Unper-turbed Cavity	DBC		HBC
# of vias	0	6	12	12
1st mode TE_{101}				
2nd mode TE_{102}				
3rd mode TE_{201}				
Frequency Response				

When the six vias are filled one at a time, the available volume decreases and the first frequency band increases until all of the vias are full, leaving the first mode frequency to reside in the high band. Since the HBC functions as triangular SIW cavities, it becomes a higher-order filter with improved rejection. In summary, twelve vias were chosen for the design of the DBC and HBC, with the E-field distributions and frequency depictions shown in the last two columns of Table 3.1.

Note that the twelve perturbations in the resonator design shift both the low and high frequency bands slightly higher compared to the unperturbed cavity. However, if lower resonant frequencies are desired, the frequency shift

from the vias can be compensated for by increasing the total size of the cavity.

3.3 Design Process

The filter was designed to have a Butterworth bandpass response, therefore methods from [99] and [2] were closely followed. Driven-mode simulations in HFSS were used to verify the design, starting with the unloaded quality factor (Q_u), which was used to characterize the filter. Eigen-mode simulations provided the theoretical Q_u values before driven-mode simulations were used. From the driven-mode results of a resonator weakly coupled into,

$$Q_u \approx Q_L = \frac{f_0}{\Delta f} \tag{3.3}$$

was applied to extract Q_u of each configuration, where Q_L is the loaded quality factor, f_0 is the resonant frequency, and Δf is the bandwidth at 3 dB below the resonance. Since the resonator is weakly coupled, the resonance occurs between -30 to -40 dB. This weakly coupling allows Q_L to be used as an approximation for Q_u because the effect from the coplanar waveguide (CPW) used to excite the resonator is minimized. This is further explained with the relationship

$$\frac{1}{Q_L} = \frac{1}{Q_u} + \frac{1}{Q_{ex}}, \tag{3.4}$$

where Q_{ex} is the external quality factor. If the external quality factor is minimized with weakly coupling, the unloaded quality factor is approximately equal to the loaded quality factor.

The CPW was designed with 50 Ω characteristic impedance to excite the filter. Figure 3.2 shows the different transmission line distances from the res-
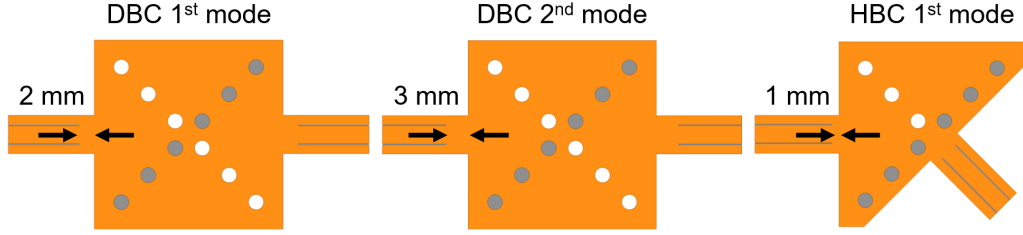
Figure 3.2: Layouts of the DBC and HBC resonators

onator that were required for each configuration (DBC first and second modes and HBC first mode) to weakly couple into the resonator for more accurate approximations of Q_u. The vias are color-coded where white represents only air and gray represents either air or Galinstan. Since Q_u was being obtained from the designs in Figure 3.2, the gray vias in the first two resonators were full of air while the gray vias in the last resonator were full of Galinstan.

After designing the resonator, external and internal coupling were considered. Assuming there is no cross-coupling, external coupling occurs between the CPWs and adjacent resonators, while internal coupling occurs between adjacent resonators in higher-order filters. A 2% fractional bandwidth (FBW) was chosen to calculate the remaining theoretical values. The external quality factor (Q_{ex}) was used to achieve a Butterworth response, which is maximally flat because it has no passband ripple. The coupling coefficient (k) was used to adjust the bandwidth. They are determined with

$$Q_{ex,in} = \frac{g_0 g_1}{FBW}, \tag{3.5a}$$

$$Q_{ex,out} = \frac{g_N g_{N+1}}{FBW}, \tag{3.5b}$$

and
$$k_{i,j} = \frac{FBW}{\sqrt{g_i g_j}}, \qquad (3.6)$$

where i and j represent the resonators, N is the filter order, and the g variables represent the Butterworth lowpass prototype coefficients from [2], which are as follows for a second-order filter.

$$g_0 = 1$$
$$g_1 = 1.4142$$
$$g_2 = 1.4142$$
$$g_3 = 1$$

Since the design is symmetrical, the external coupling is the same at the input and output, or (3.5a) and (3.5b) are equal. Equation 3.6 only applies to the HBC because at least two resonators are required for internal coupling.

To verify the calculations, the driven-mode results were checked with

$$Q_{ex} = \frac{\pi f_0 t_d}{2} \qquad (3.7)$$

and
$$k_{i,j} = \frac{f_2^2 - f_1^2}{f_2^2 + f_1^2}, \qquad (3.8)$$

where t_d is the time delay of each single resonator with strong coupling, and f_1 and f_2 are the separated peaks of the weakly-coupled HBC resonators.

The final filter layout is shown in Figure 3.3 with corresponding dimensions in Table 3.2. Consistent with the previous convention, the white vias are always empty with air and the gray vias are air in the DBC and Galinstan in the HBC. The transmission lines of the CPW were enhanced to increase visibility in both Figures 3.2 and 3.3.
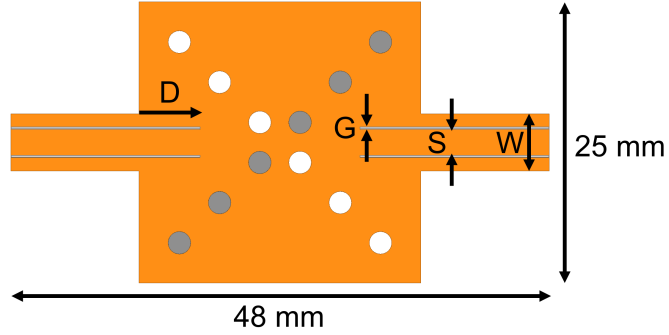
Figure 3.3: Layout of the dual to high band filter

Table 3.2: Filter Dimensions for the Dual to High Band Filter

Distance of CPW into cavity ($\boldsymbol{D}$)	5.4 mm
CPW total width ($\boldsymbol{W}$)	5.1 mm
CPW track conductor width ($\boldsymbol{S}$)	2.3 mm
CPW gap width ($\boldsymbol{G}$)	0.2 mm
Via radii ($\boldsymbol{R}$)	1 mm

3.4   Simulation and Experimental Results

The filter, fabricated with an LPKF prototype machine, is displayed in Figure 3.4 with the gray vias full of Galinstan. A picture of the test environment is in Figure 3.5, where a structure is connected to the two-port calibrated Keysight PNA network analyzer.

The simulated and measured results of both configurations are compared in Figures 3.6 and 3.7. The simulated results were from the filter in Figure 3.3, and the measured results were from the fabricated filter in Figure 3.4. Figure 3.6 shows the comparison between the DBC and the HBC. The low band is effectively turned off for the HBC, but the high band resonant frequencies are not completely aligned. The alignment of the frequency bands can be cor-
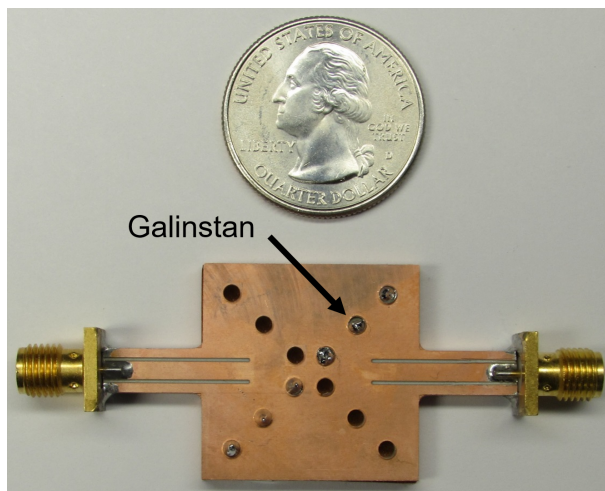
Figure 3.4: Fabricated dual to high band filter with Galinstan vias

rected by filling selected vias, for the response shown in Figure 3.8. To achieve alignment of the high band frequencies, the DBC was simulated with the four outer corner vias full of Galinstan to increase the resonant frequency. This demonstrates a useful method for centering the frequency bands for practical purposes.

Figure 3.7 shows the comparison between the simulated and measured responses. The behavior of the DBC and the HBC were as expected, however the resonant frequencies of the measured results were slightly lower. One contributor to this occurrence could be that the fabricated filter has slightly larger volume, although it was not large enough to be confidently confirmed through manual measurements. Another contributor could be that the air inside the vias in reality had higher relative permittivity than 1, where a value of 1 is ideal. If the permittivity inside the vias was closer to the value of the dielectric, that would cause a decrease in resonant frequency because it would reduce the effect of the perturbation method.

A summary is shown in Table 3.3 of a comparison between the theoretical,

44
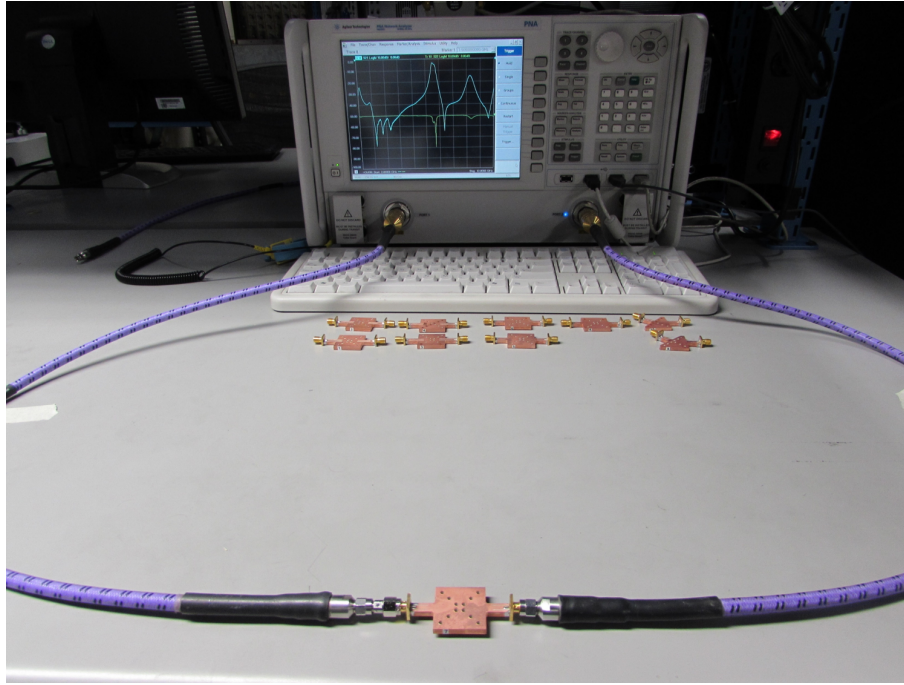
Figure 3.5: Test environment for measuring the filter and resonators

simulated, and measured results of the DBC and HBC, where f_L represents the low band frequency, f_H represents the high band frequency, IL is insertion loss, and BW is bandwidth. The theoretical values were calculated and taken from HFSS Eigen-mode simulations, the simulated values were extracted from HFSS driven-mode simulations, and the measured values were obtained from the network analyzer from Figure 3.5. Overall, there was good agreement between the values. The highest discrepancy was with the Q_u of the HBC, due to the resonator layout and oxidation of Galinstan.

Concerning the resonator layout, the theoretical Q_u of the HBC was based on a perfect triangular design with no vias. However, the simulated Q_u was from the layout design in Figure 3.2. The design was extended larger than one triangular resonator to include the diagonal vias full of Galinstan, which would characterize the effect of the liquid metal. The added volume and
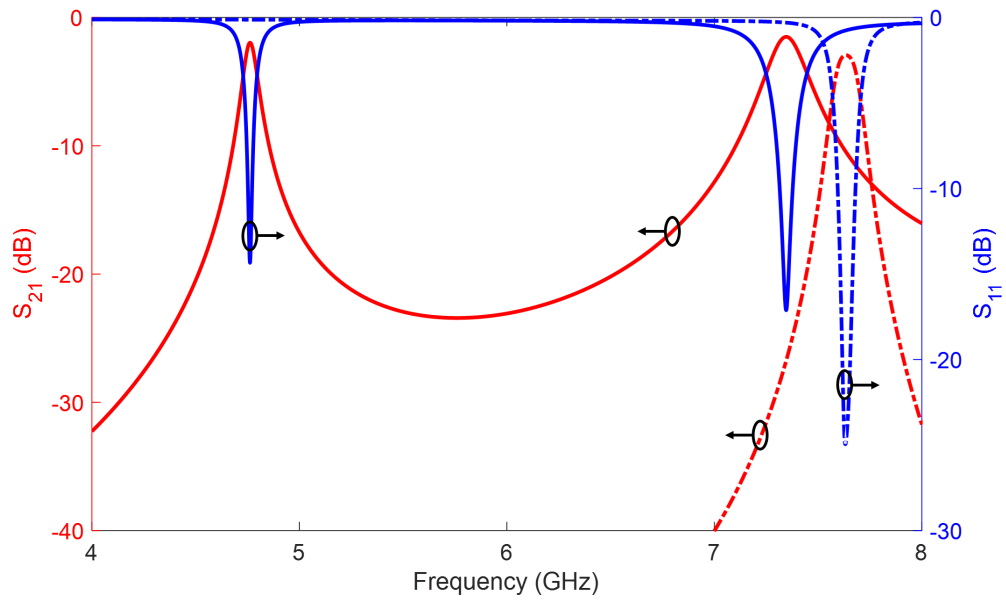
(a) Simulated results of the DBC (solid) and HBC (dot-dashed)
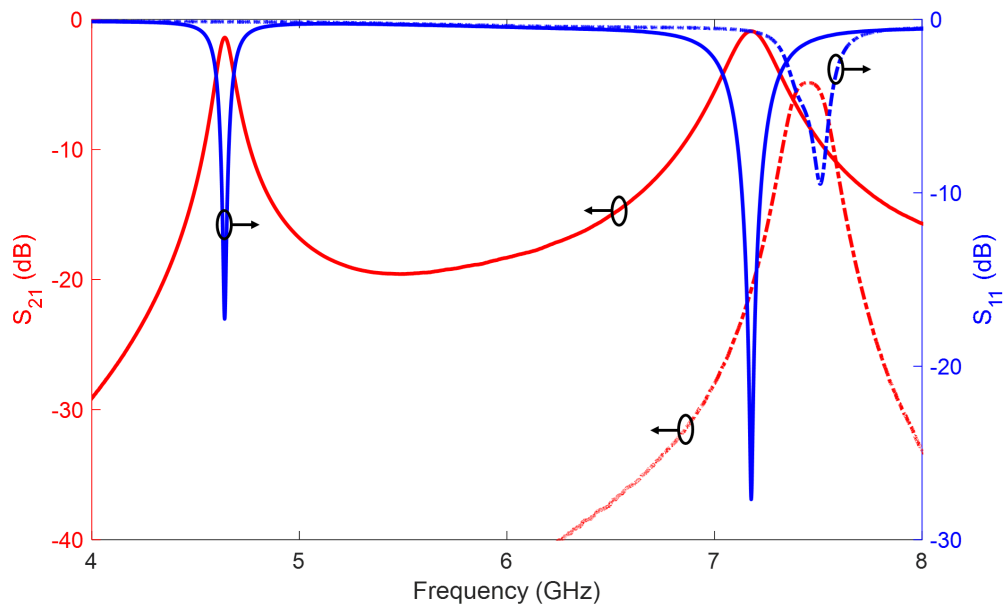
(b) Measured results of the DBC (solid) and HBC (dot-dashed)

Figure 3.6: Comparison of the DBC and HBC results of the dual to high band filter
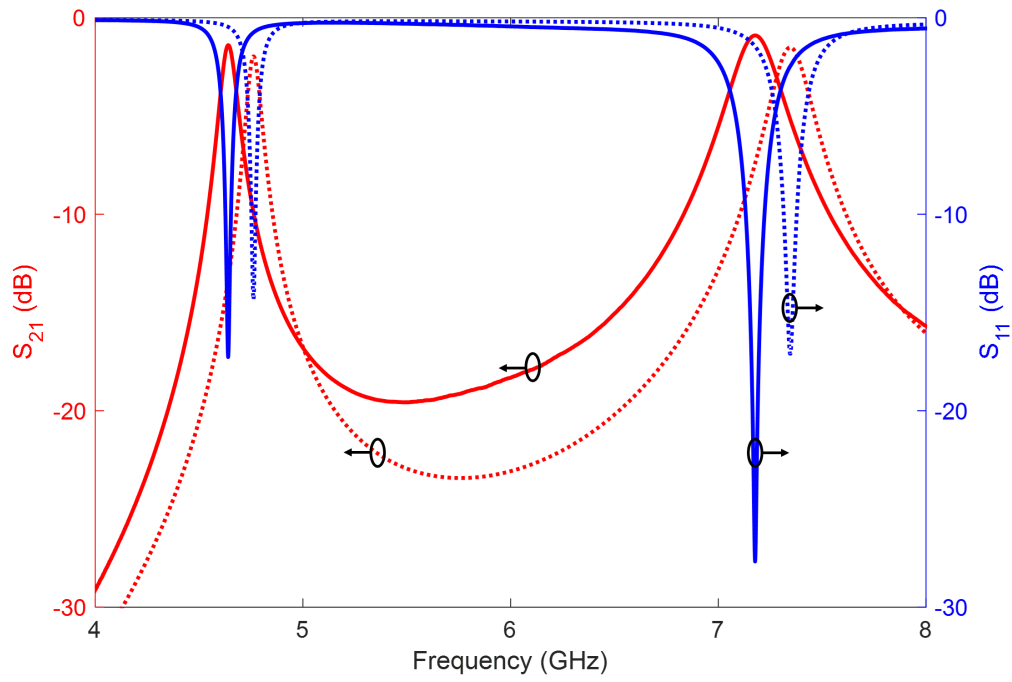
(a) DBC simulated (dotted) and measured (solid)
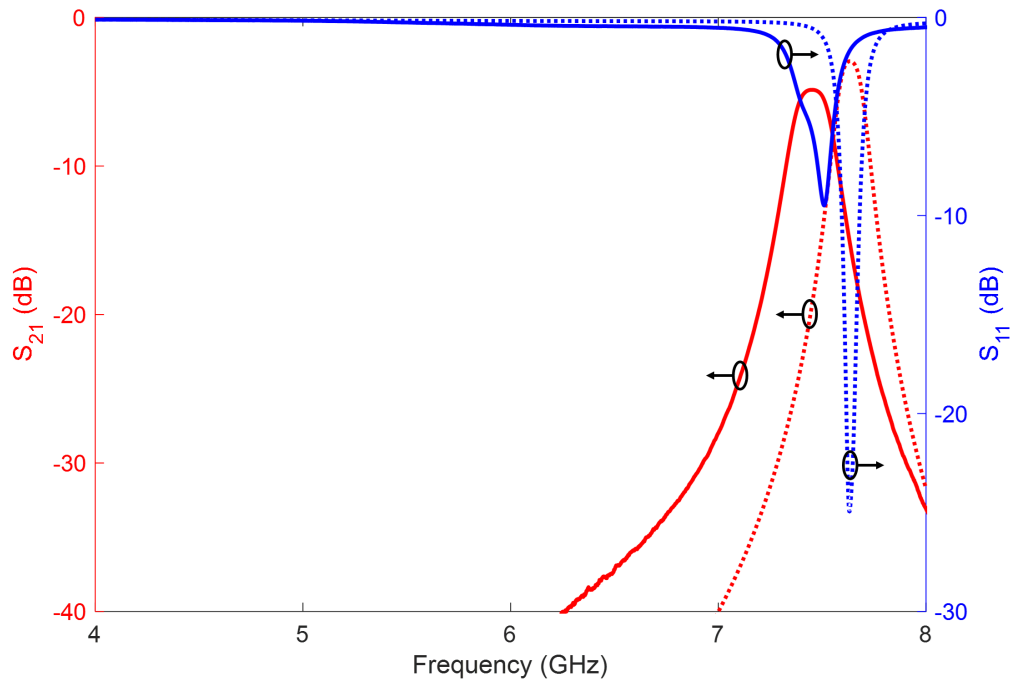
(b) HBC simulated (dotted) and measured (solid)

Figure 3.7: Comparison of the simulated and measured results of the dual to high band filter
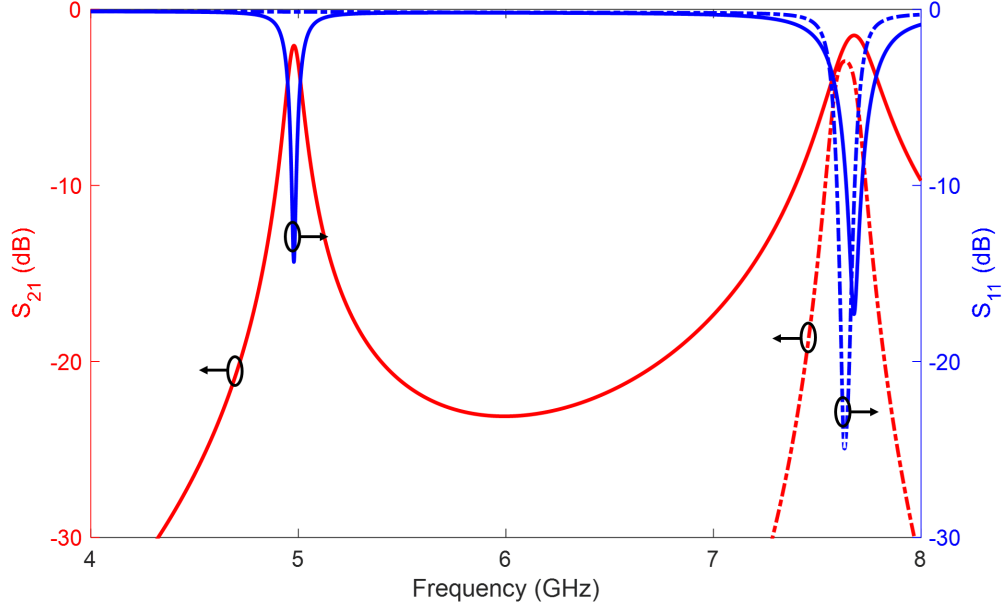
Figure 3.8: Simulation of DBC aligned with HBC by filling selective vias

metallic vias significantly lowered the Q_u to 253 because the E-field around the vias was minimized, which accounted for a large portion of the resonator. This was however useful for comparing simulated and measured Q_u when using Galinstan. This explains the difference between the theoretical and simulated values. The difference between the simulated and measured values depends on oxidation, which is explained further in Section 3.5.

3.5 Discussion on Capabilities and Improvements

The dual to high band filter functioned successfully by turning on or off the first mode, as demonstrated in Figure 3.6. There were however, several improvements that could be made to increase the capabilities and enhance the response. Regarding the design, it was a lower-order filter that could easily be raised by cascading multiple resonators. Additionally, only the low band

Table 3.3: Filter Summary for Dual to High Band Filter

	DBC ($N = 1$)			HBC ($N = 2$)		
	Theoretical	Simulated	Measured	Theoretical	Simulated	Measured
f_L *(GHz)*	4.7 GHz	4.8 GHz	4.7 GHz	-	-	-
Q_{uL}	420	430	410	-	-	-
IL *(dB)*	~0	2.0	1.4	-	-	-
BW *(MHz)*	94	75	85	-	-	-
FBW *(%)*	2.0	1.6	1.8	-	-	-
f_H *(GHz)*	7.4 GHz	7.3 GHz	7.2 GHz	7.4 GHz	7.6 GHz	7.5 GHz
Q_{uH}	434	437	412	426	253	123
IL *(dB)*	~0	1.5	0.9	~0	2.9	4.9
BW *(MHz)*	150	210	250	150	130	200
FBW *(%)*	2.0	2.8	3.5	2.0	1.7	2.7

was controllable while the high band always remained on. Another method could be used to turn on or off the high band as well to make the filter more frequency agile. The filter would then be prepared to handle overcrowding of either band, for example. These improvements are implemented in Chapters 4 and 5 with the remaining two filter designs.

In the HBC when Galinstan was used, there was an increase in the measured insertion loss and a decrease in the measured Q_u, which can be seen in Figure 3.7 and Table 3.3. This loss was caused by the outer oxidation layer which had significantly lower conductivity and resulted in a weaker electrical connection to the copper plating. HFSS was used to find the conductivity of Galinstan after it had oxidized, resulting in a Q_u of 123, which is about half of the expected value reached using pure Galinstan. The simulation im-
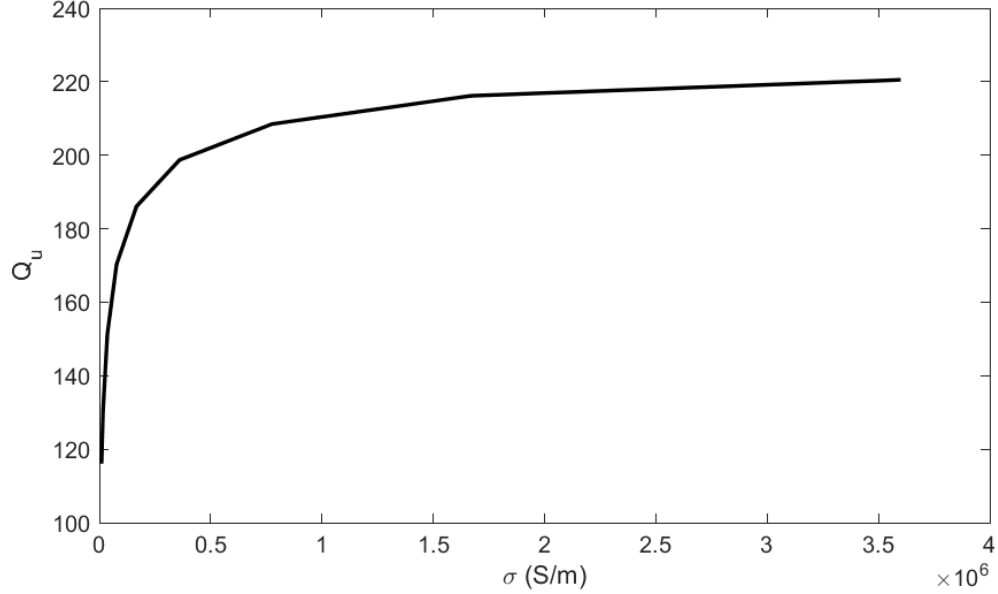
Figure 3.9: The effect of oxidized Galinstan on the Q_u of the HBC

plied that the oxidized Galinstan had approximately 1% of the conductivity of pure Galinstan. Figure 3.9 shows the effect that oxidized Galinstan can have on the Q_u, indicating that the relationship is logarithmic. The oxidation could be cleaned with a solution such as NaOH, but then it must make direct contact with the copper plating. If there is a layer of NaOH between the Galinstan and copper, that could also degrade the electrical connection and raise the loss. A closed loop system for the Galinstan could be implemented to minimize oxidation, ensure connectivity, and increase automation.

Referring again to Figure 3.6, the second mode in the DBC did not perfectly overlap with the first mode of the HBC. That was because the E-field of the second mode of the DBC could exist inside the vias, which was not the case for the first mode of the HBC since the vias were full of metal, as revealed in Table 3.3. One solution is to fill the corner vias in the DBC with Galinstan to slightly decrease the available volume and increase the resonant

frequency up to overlap with the HBC first mode. This solution was presented in Figure 3.8, and can be applied to other configurations that need alignment.

3.6 Conclusion

The dual to high band bandpass filter demonstrated a design for reversible and repeatable mode-reconfigurability. It could switch between multi-band and single-band operation by applying the concept of mode-shifting, which was accomplished by filling certain vias with Galinstan liquid metal. The dual band configuration (DBC) was a first-order bandpass filter realized in a square cavity resonator. The high band configuration (HBC) was a second-order bandpass filter in coupled triangular resonators, which effectively turned off the low band. Since the HBC was higher-order, it had better roll-off at the cutoff frequencies, which improved the rejection. This demonstrated mode-reconfigurability with an SIW filter that utilized liquid metal for reversible switching. The simulated and measured results for the dual to high band filter were in good agreement.

Chapter 4

Low to High Band Bandpass Filter

4.1 Introduction

The purpose of the low to high band bandpass filter is to operate in one frequency band at a time, either in low band configuration (LBC) or high band configuration (HBC). In practice, if one band becomes too crowded, the filter can switch to the other frequency band. The filter switches between second-order in the low band with two square cavities, to fourth-order in the high band with four rectangular cavities. To turn off the low band, the concept of mode-shifting from Chapter 3 is applied by filling certain vias with Galinstan liquid metal. To switch off the high band, a transmission zero (TZ) is generated and centered at the high band center frequency to suppress the resonance. Each configuration was designed for a Butterworth bandpass response with the same fractional bandwidth (FBW) of 2.3% with at least 30 dB return loss. Switching between the states also required different external coupling, so metal was used to change the active slots of a coplanar waveguide (CPW). Finally, the filter structure was designed to be more sturdy by making it perfectly rectangular. SIW vias outlined the CPW as well as the cavities, further simplifying the fabrication process and making the filter less susceptible

to breaking under stress. The design was simulated with Galinstan liquid metal to enable reversible switching between configurations. However since Chapters 2 and 3 demonstrated that the measured results from Galinstan are comparable to copper, the fabricated low to high band filter was measured with copper.

4.2   Theory and Design

The low to high band filter builds on the theoretical concepts from Chapter 3. It is a higher-order filter that switches between second-order in the LBC and fourth-order in the HBC. Since the filters in Chapters 4 and 5 both switch between second-order and fourth-order filters, they require different Butterworth lowpass filter prototype coefficients when applying (3.5) and (3.6). The coefficients listed in Section 3.3 apply to the second-order configurations, but the fourth-order configurations use the following coefficients.

$$g_0 = 1$$
$$g_1 = 0.7654$$
$$g_2 = 1.8478$$
$$g_3 = 0.7654$$
$$g_4 = 1.8478$$
$$g_5 = 1$$

The 50 Ω CPW was designed with the same G, S, and W values from Table 3.2, but D was changed as well as the distance the CPW extends outside of the filter. Compared to the filter in Chapter 3, the vias and distances between them were made much smaller. The radii were reduced to 0.5 mm and the spaces ranged from 0.7 mm to 1 mm, which allowed the first and

Table 4.1: Conditions of Each Configuration for the Low to High Band Filter

	LBC	HBC
Gray vias	Air	Galinstan
Channels 1-2	Galinstan	Air
Channels 3-4	Air	Galinstan

second modes of the HBC to align more. These changes were implemented for the filter in Chapter 5 as well since they are improvements of the previous design in Chapter 3.

Figure 4.1 shows the complete filter layout, with the same convention as in Chapter 3; the black vias are copper plated, the white vias are always empty, and the gray vias are either empty or full of Galinstan. The design is symmetrical about the central black vias, but the right side shows the top dielectric piece while it is hidden on the left side in order to make the filter completely visible. The top dielectric is the same material as the filter substrate (Rogers TMM3), with vias and trenches that act as channels for the liquid metal. Table 4.1 corresponds to the labels in Figure 4.1(a) to show which vias and transmission line paths must be empty or full to excite the LBC or HBC. The transmission lines are covered with channels 1-4, numbered and circled in yellow. Figure 4.1(b) shows a different perspective of the filter for height indication.

Table 4.2 corresponds to the variables in Figure 4.1(a), where L represents the low band, H represents the high band, IL stands for insertion loss, and BW stands for bandwidth. The table lists the distances and how the filter is affected when the values are lowered or raised too much. Generally, the external coupling controls the TZ and matching to the CPW, while the gaps between
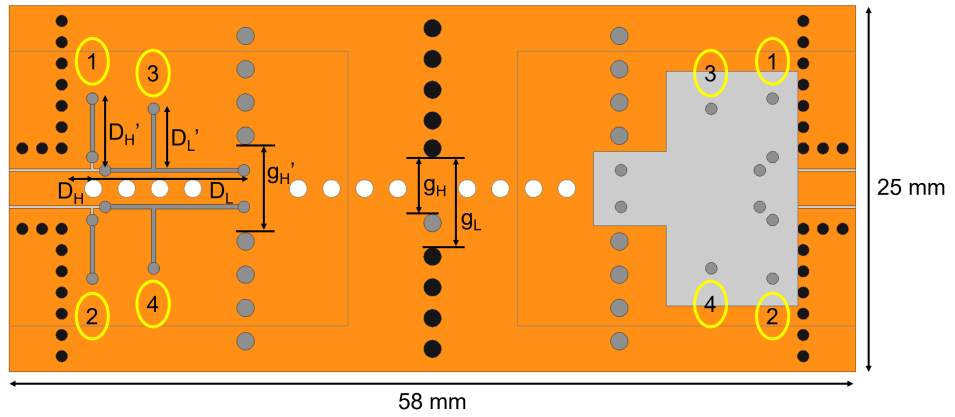
(a) Top view with liquid metal channels numbered 1-4
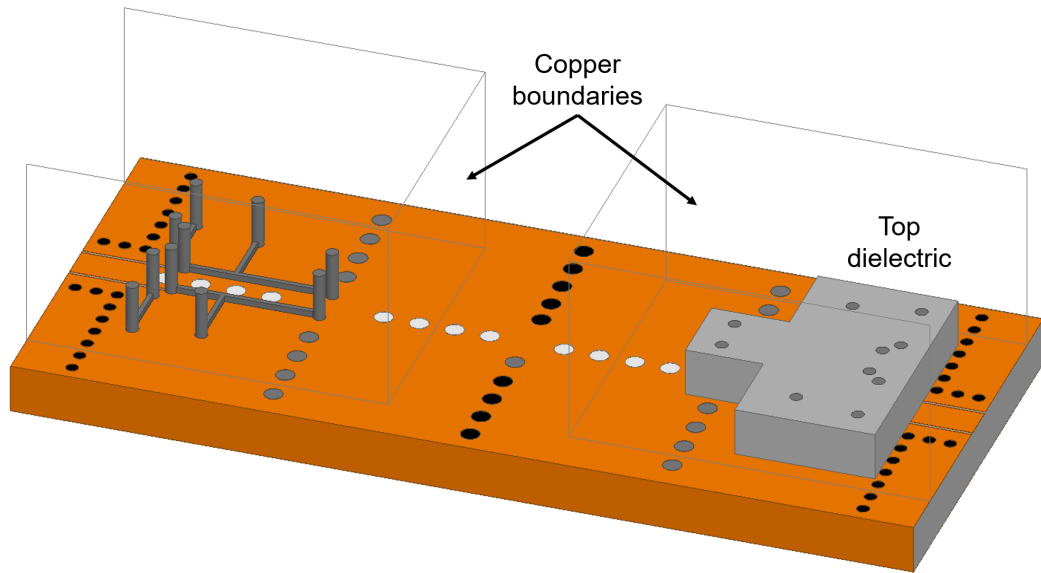
(b) Angled view

Figure 4.1: Layout of the low to high band filter

Table 4.2: Filter Tuning Trends for the Low to High Band Filter

Variable	Value (mm)	Value too High	Value too low
D_L	12.4	Decreases TZ frequency	Increases TZ frequency
D_L'	4.4	Creates ripple	Increases IL
D_H	1.8	Increases IL	Creates ripple
D_H'	5.1	Creates ripple	Increases IL
g_L	6.2	Increases BW	Decreases BW
g_H	3.9		
g_H'	6.0		

the vias control the internal coupling between the resonators. When the external coupling is not matched, either a ripple is generated or the insertion loss greatly increases, whereas the gaps affect the bandwidths. The horizontal position of D_L' did not have a large effect, but the length was similar to the effect of D_H. Weakening the external coupling by making the transmission lines shorter caused higher insertion loss, and moving them further into the filter had the same effect. This is why D_H had an opposite effect from D_L' and D_H'. The resonators were magnetically coupled, so moving the transmission lines towards the ends where the E-field was weaker, positioned them where the H-field was stronger, and therefore strengthened the coupling.

One of the changes made from the filter in Chapter 3 was the design of the resonator. Previously, the gray vias were placed diagonally across the resonator which resulted in triangular cavities, but the higher-order filters in Chapters 4 and 5 have perpendicularly placed vias for simplification reasons. Splitting the square resonators into rectangles simplified the internal coupling. The coupling gaps did not need to be off-centered in the higher-order design to excite each resonator. Although using a higher-order design adds complexity, choosing

rectangular cavities instead of triangular simplified the design process.

However, the higher-order design resulted in an unwanted resonance between the two frequency bands. This explains why the copper boundary marked in Figure 4.1(a) was added. The boundary suppressed the strong, undesired resonance at 6.5 GHz, shown in the solid red plot in Figure 4.2(a). The plot shows a dual band response for the purpose of demonstrating this concept, although the low to high band filter did not include a DBC. A dual band response was chosen for displaying the extra resonance at 6.5 GHz between the bands, which was also present in both the LBC and HBC. The black dashed plot resulted from adding the copper boundaries, which successfully suppressed the spurious resonance.

Initially, the unwanted resonance was thought to come from cross-coupling between the source and load, or input and output CPWs. However, cross-coupling was not apparent by displaying the E-field. Figure 4.2(b) shows the E-field distribution inside the cavity at the low band and high band resonances, respectfully. Figure 4.2(c) shows the E-field distribution at 6.5 GHz where the spurious resonance occurs.

The corresponding coupling routing diagrams are displayed in Figure 4.3, showing direct coupling between adjacent resonators. Each circle in Figure 4.3 represents a structure: S is the source, L is the load, and 1-4 represent each resonator. The routing diagrams apply to the filters in Chapters 4 and 5 since they both switch between second-order and fourth-order filters. It appears that the routing diagram in Figure 4.3(a) applies to the unwanted resonance in Figure 4.2(c). The source and load occupy more space and therefore the resonators are smaller than they were at the low band frequency in Figure 4.2(b). This causes the filter to resonate at a higher frequency of 6.5 GHz. Adding

57

the copper boundaries solved this issue by blocking any leakage and removing the spurious resonance.

Lastly, the characteristic impedance (Z_0) at the boundary of the CPW and top dielectric piece was checked. This is because air is above the filter except where the top dielectrics are placed that have the Galinstan channels. The dielectric has a higher permittivity than air ($\varepsilon_r = 3.27$), and since it is above the CPW, it can cause an impedance mismatch between the boundaries. However, the transmission line was well matched to 50 Ω across the boundary. If the mismatch is dramatic, it can be addressed by either redesigning the transmission lines at the boundary, or by fine tuning the coupling of the filter with the variables listed in Table 4.2 to output a matched response. Although the top dielectric did not cause a significant change, the filter was slightly tuned to eliminate the effect by using the later option.

Following the same method as before, the resonators were checked in HFSS Eigen-mode, and then the resonators and filter were verified in HFSS driven-mode simulations. The following two sections elaborate on the design of the LBC and HBC.

4.2.1 Low Band Configuration

Consistent with Chapter 3, the resonator was used to extract the unloaded quality factor (Q_u). The layout is shown in Figure 4.4, where the gray vias are always air because the LBC uses the square structures. The variable D from Figure 4.4 is 2 mm away from the cavity boundary. The CPW that extends from the structure was elongated from 4 mm to 7 mm to give the EM wave enough distance to fully generate before entering the cavity. Since the transmission lines ended further away from the cavity for weakly coupling, the
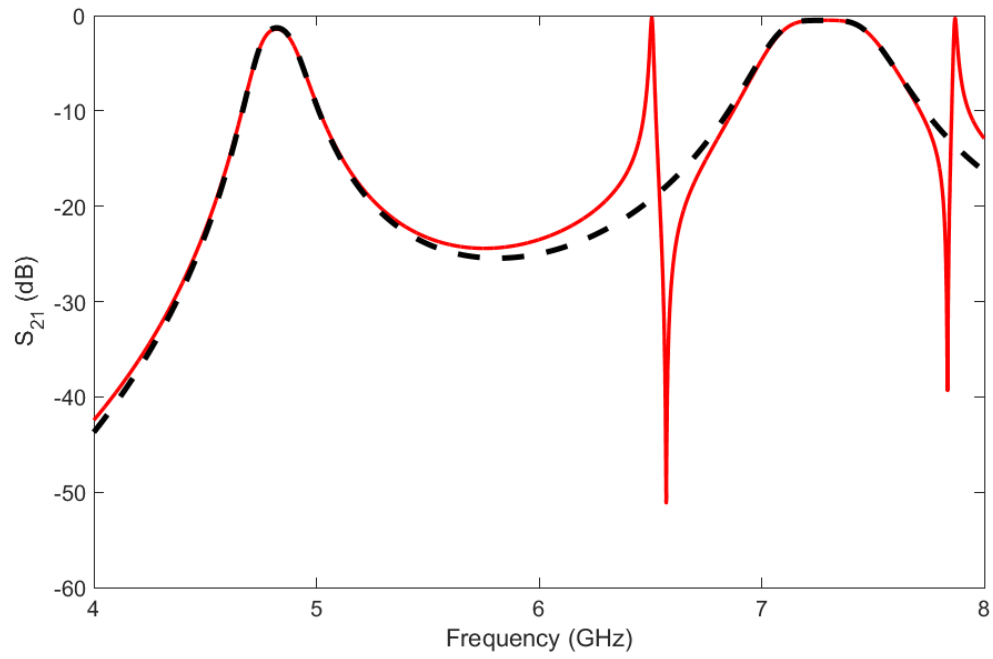
(a) DBC of filter with unwanted resonance between low and high bands
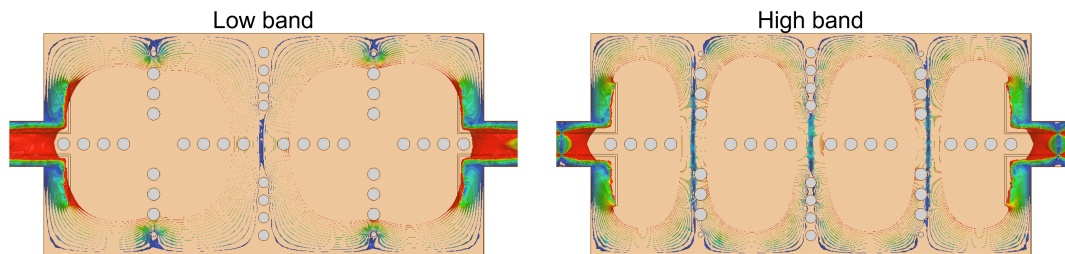
(b) E-field distribution of the low and high bands
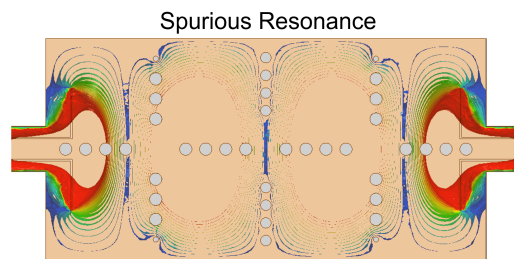
(c) E-field distribution of the spurious resonance

Figure 4.2: Simulated results with and without the copper boundaries to observe the occurrence of an unwanted resonance at 6.5 GHz

(a) Low frequency band

(b) High frequency band
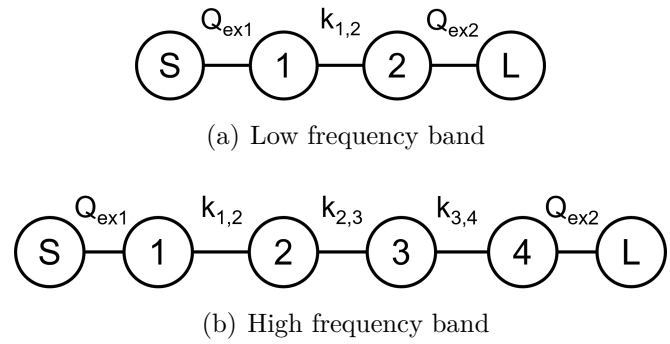
Figure 4.3: Routing diagrams for the low and high frequency bands
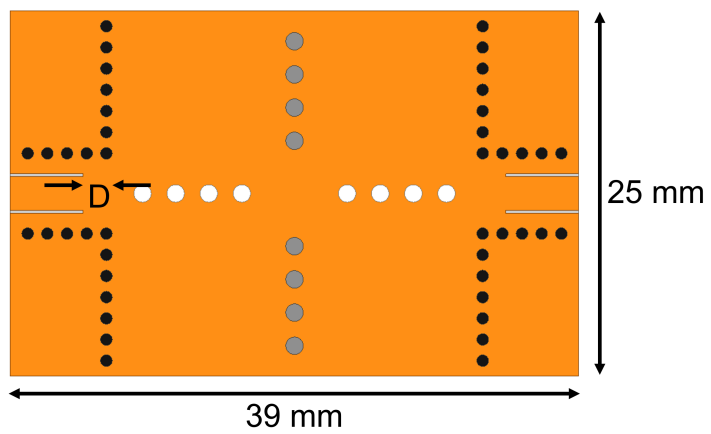
Figure 4.4: Layout of the LBC resonator

input and output structures were lengthened to make the transmission lines of the CPW long enough to excite the resonator.

The LBC was made possible by a strategically placed TZ, therefore it required stronger external coupling with channels 3-4 from Figure 4.1(a). The transmission lines underneath channels 3-4 reached over halfway through the first resonator, so the LBC required at least two resonators. That is, if only one resonator was used, the transmission lines would overlap. This problem did not occur for the LBC because it is a second-order filter made of two resonators, unlike the filter in Chapter 3 which was of lower-order.
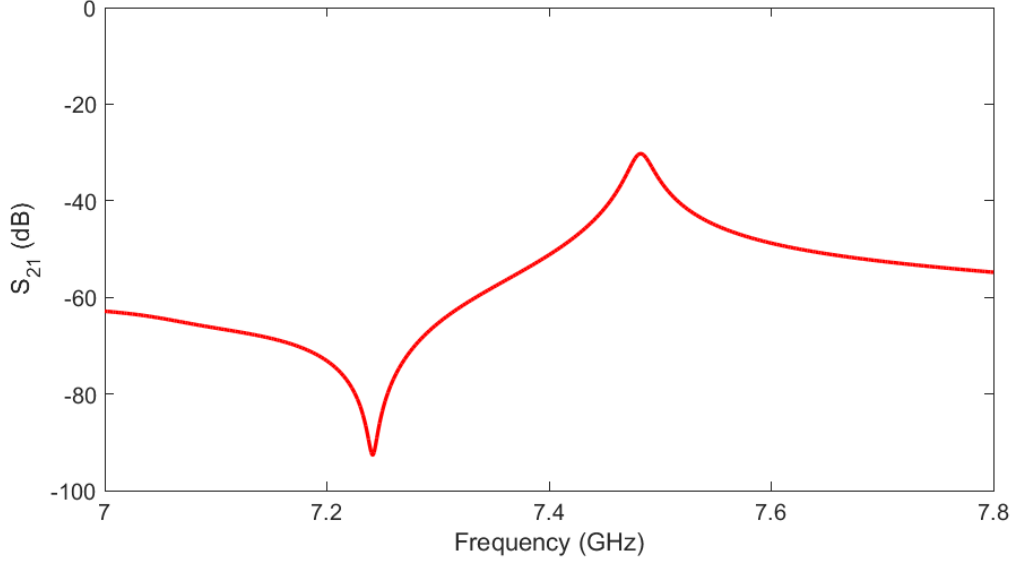
Figure 4.5: High band frequency of the LBC successfully suppressed

The TZ had an inverse relationship with D_L from Figure 4.1(a); when the length was increased, the frequency of the TZ decreased, making it relatively simple to tune. The TZ was positioned over the high frequency band, suppressing the resonance to -30 dB and successfully turning it off as shown in Figure 4.5. This initially resulted in a response that resembled a Chebyshev filter in the low band because there was a large ripple, but adding D_L' from 4.1(a) was used to tune the response to a Butterworth filter, as desired.

4.2.2 High Band Configuration

For the HBC, Q_u was extracted using the layout design from Figure 4.6 of a single rectangular cavity, where D was set to 4 mm and the CPW distance away from the cavity boundary was 6 mm. Although the transmission lines required a longer distance away from the resonator than for the LBC, the CPW did not need to be as long to achieve weakly coupling.

61
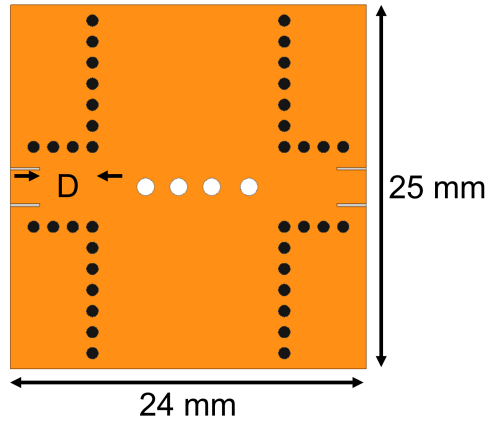
Figure 4.6: Layout of the HBC resonator

Overall, the HBC followed the same design method outlined in Chapter 3, however there were some additional considerations. As previously mentioned, the filter was designed for equal FBWs in both configurations. Initially, they were given equal bandwidths of 100 MHz, but the HBC displayed too much insertion loss of 2.5 dB. Regarding the simulated design, the specification for maximum insertion loss was chosen as 2 dB. There was more transmission loss at higher frequencies because at a fixed bandwidth, the FBW lowers as the frequency increases. Furthermore, in referring back to (3.5) and (3.6), the filter design parameters depend on FBW, not bandwidth. According to [4], the passband insertion loss is inversely proportional to the FBW and Q_u, while it is proportional to the number of resonators used, or filter order. This means that if the FBW is decreased too much, the insertion loss can become too high.

The 100 MHz bandwidth was too small for the fourth-order filter. Therefore, the bandwidth of the LBC was slightly increased to 111 MHz resulting in a FBW of 2.3%. This was then matched for the HBC with a bandwidth of 179 MHz and FBW of 2.4%, compared to 1.4% before, which significantly reduced the loss.
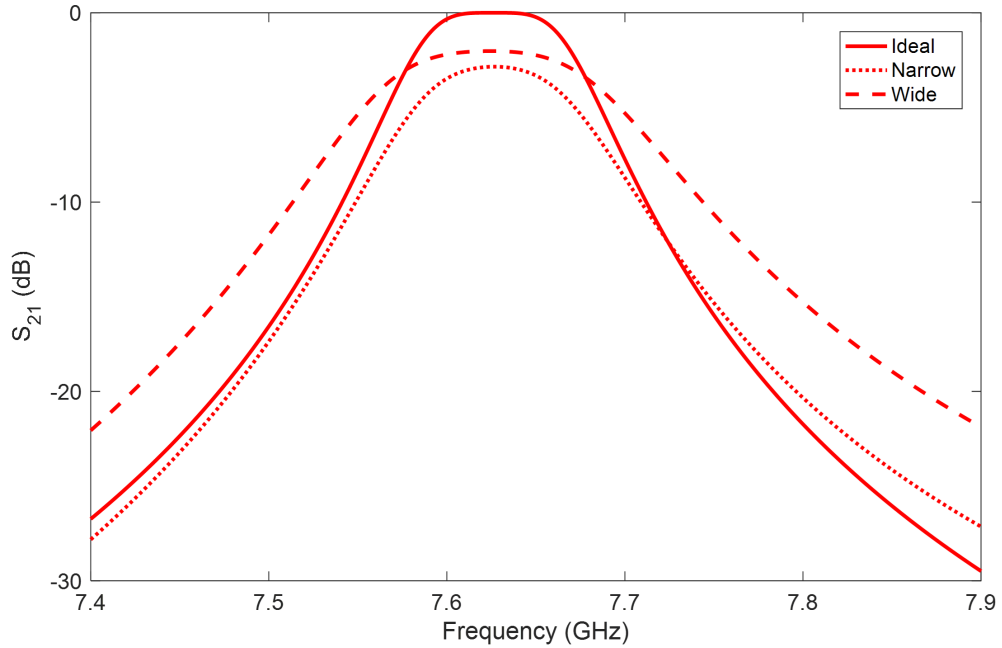
Figure 4.7: Butterworth bandpass filter responses with different bandwidths

This concept is shown in Figure 4.7 with a second-order microstrip filter on AWR Design Environment [26]. The filter is designed with a 100 MHz bandwidth (labeled narrow), and compared to an ideal Butterworth response given the same bandwidth (labeled ideal). With the narrow bandwidth, an insertion loss of 3 dB is observed, but then the bandwidth is increased to 150 MHz (labeled wide). The wide bandwidth response has an insertion loss of 2 dB, demonstrating that as the bandwidth and FBW increase, the insertion loss decreases.

One more challenge arose when designing the HBC, visible in Figure 4.8. Two of the poles were too low and not aligned with the other two poles in the plots from Figure 4.8(a). In referring to Figure 4.8(b), which corresponds to the separated poles plot, the first and last resonators had weaker E-fields and therefore resulted in the lower resonant frequency. To compensate for

the difference, the gray vias were moved as the arrows indicate to decrease the outer resonator volumes and raise their frequency, meanwhile increasing the inner resonator volumes and lowering their frequency. This combined the poles at the same resonant frequency to create the plot with all four poles aligned. The difference in rectangular cavity sizes could have been due to the CPW structures. The input and output structures that guide the CPW could add volume to the outer resonators, making them larger than the perfect rectangular structures. Moving the vias that constructed the SIW boundaries resulted in equal cavity sizes for each resonator.

4.3 Simulation and Experimental Results

A picture of the fabricated low to high band filter is shown in Figure 4.9. The vias were all empty, with the black vias from Figure 4.1 all copper plated. The transmission lines were visible because the top dielectric pieces were not placed over them, in order to show the entire body.

The LBC and HBC simulated and measured results are compared in Figure 4.10, where switching between configurations can be observed. To directly compare between the simulated and measured results, the configuration plots are displayed in Figure 4.11. The filters were measured by covering the appropriate transmission lines with copper tape in place of Galinstan. The top dielectric pieces were placed over the tape, but did not affect the results significantly.

The LBC was measured without the upper black via above g_L in Figure 4.1(a) filled. This achieved better impedance matching in the fabricated filter and widened the bandwidth like the HBC. When it was empty as shown in Figure
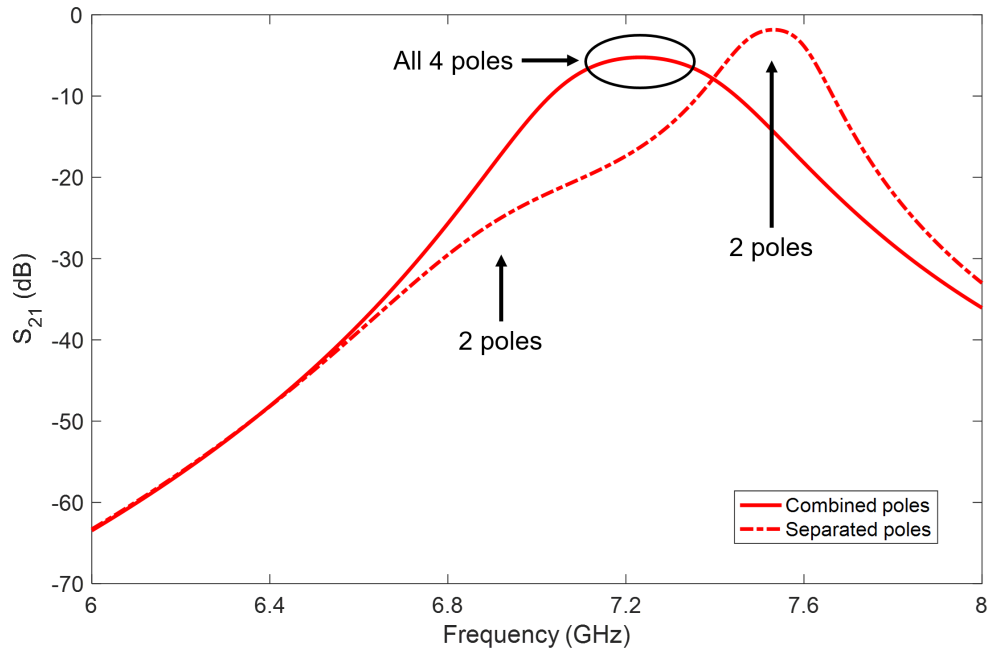
(a) HBC of filter with split poles
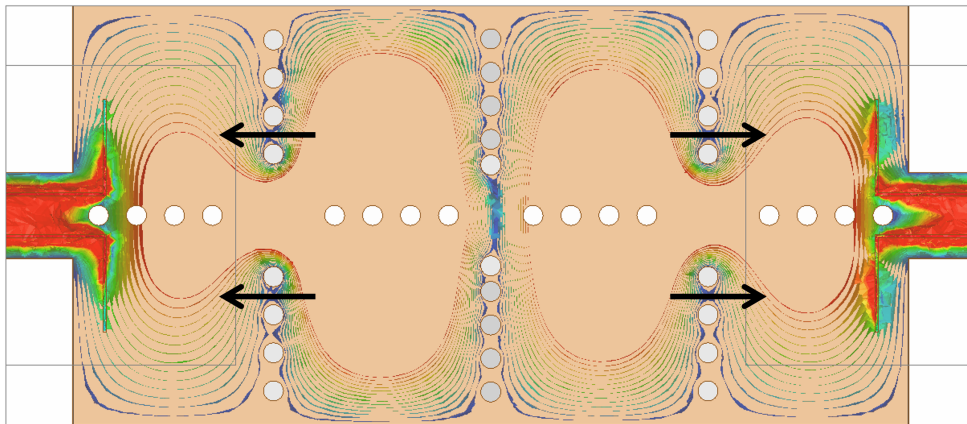
(b) E-field distribution of filter with split poles before changing the cavity sizes

Figure 4.8: Cavity size adjustments to combine the poles in the HBC
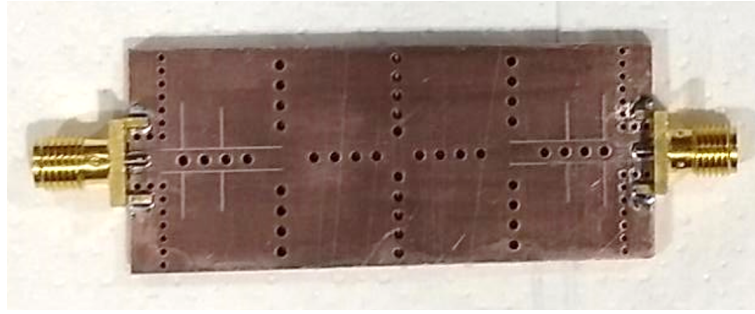
Figure 4.9: Fabricated low to high band filter

4.11(a), a ripple was generated, resembling a Chebyshev response instead of a Butterworth response. However, in the low band the insertion loss was 1.4 dB and the return loss was more than 10 dB. In the high band the insertion loss approached 15 dB, so the LBC performed generally well in terms of functionality. There was resonance near 8 GHz, but the transmission was very low so the high band was off. When the black via was filled and the bandwidth decreased, the measured insertion loss was over 5 dB, but there was no ripple. When comparing the two outputs, the response in Figure 4.11(a) was chosen by leaving the black via empty because the insertion loss was much lower.

Then attempts were made to fill the gray vias with Galinstan for the HBC, but due to the smaller vias, high surface tension, and stronger attraction to the syringe tip, the vias could not be manually filled. This was not a challenge for the filter in Chapter 3 because the via diameters were double the size. Since Galinstan could not fill the vias, measurements were only taken with copper. Copper wires were soldered between the top and bottom copper plating to test the HBC as a proof of concept. As shown in Figure 4.11(b), the poles slightly separated because the fabricated filter did not perfectly match the simulated design in terms of the external coupling and the sizes of the cavities. Regarding the cavity sizes, the wire used inside the vias did not fill the entire
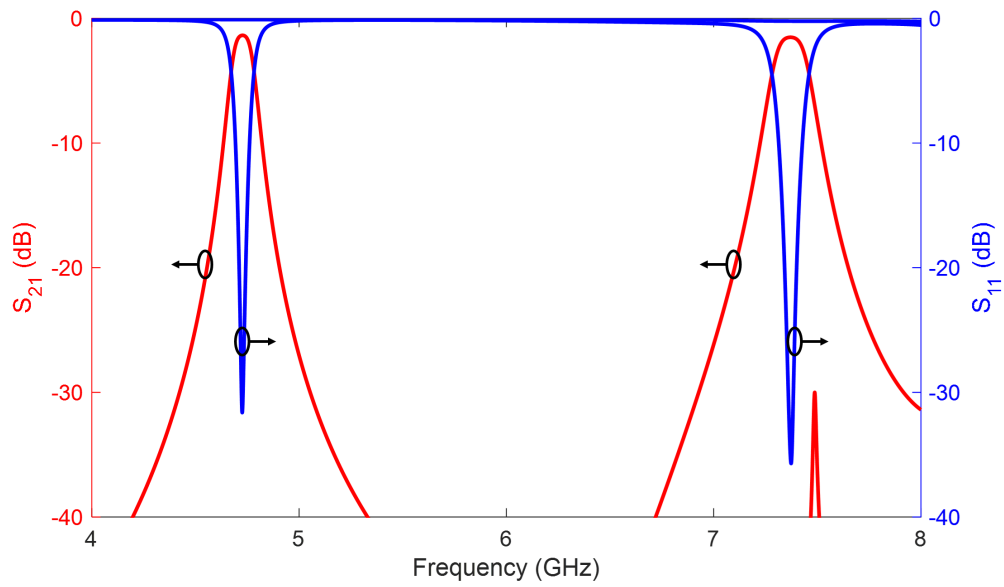
(a) Simulated results of the LBC and HBC
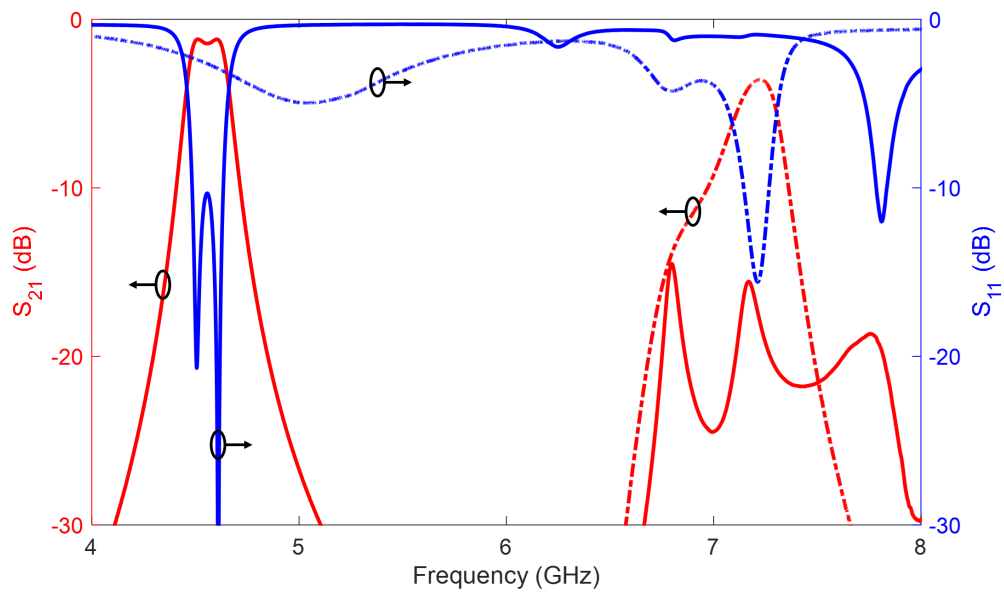
(b) Measured results of the LBC (solid) and HBC (dot-dashed)

Figure 4.10: Comparison of the LBC and HBC results of the low to high band filter
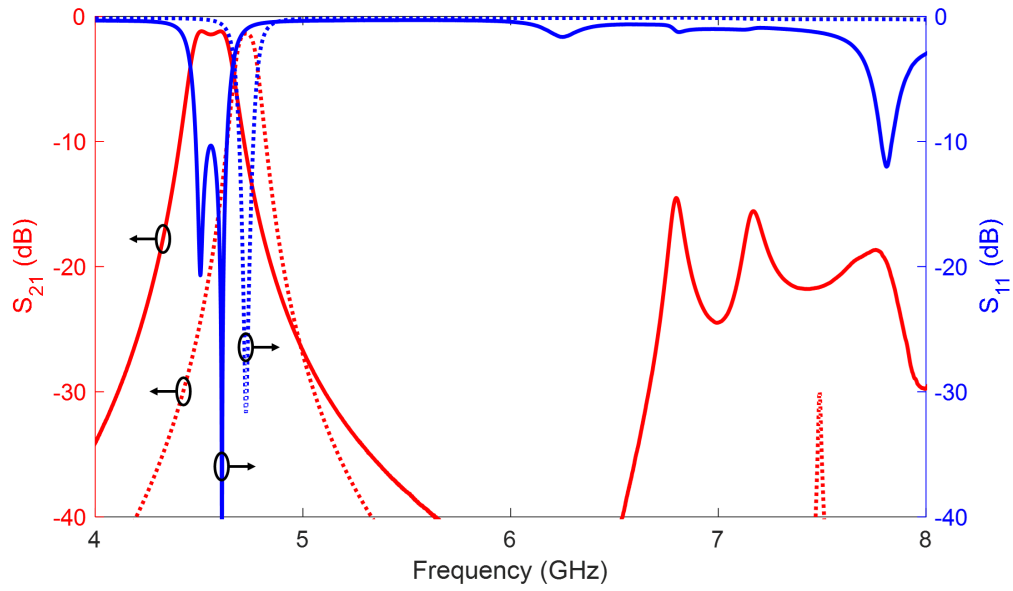
(a) LBC simulated (dotted) and measured (solid)
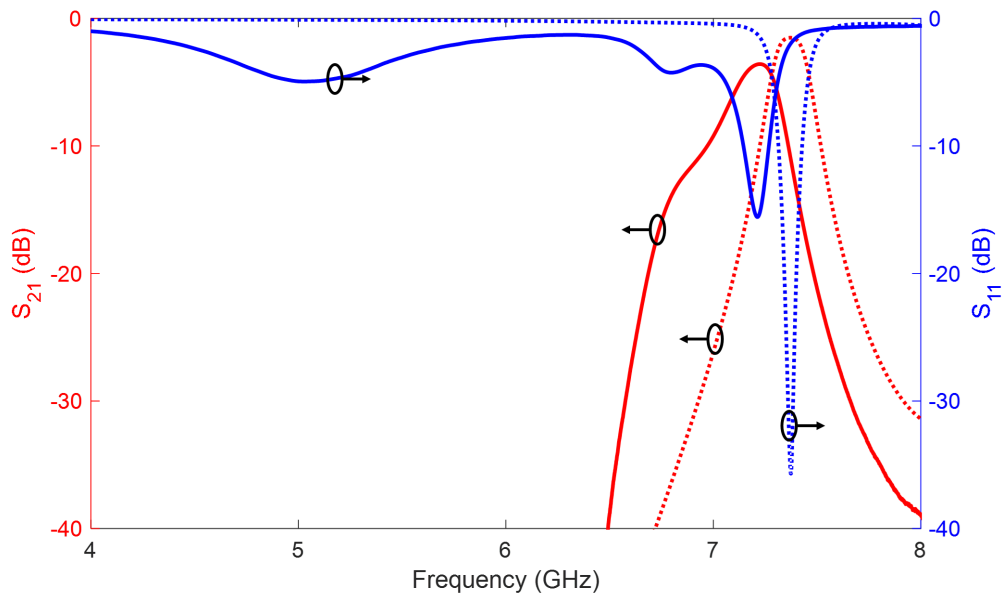
(b) HBC simulated (dotted) and measured (solid)

Figure 4.11: Comparison of the simulated and measured results of the low to high band filter

circumferences, causing the cavity sizes to be disproportionately larger than designed for all four poles to combine.

However, the cavity sizes did not significantly contribute to the mismatch, compared to the CPWs. Due to fabrication tolerances, the transmission lines were not as wide as they were designed, so manual removal of copper plating and addition of copper tape were used to tune the filter. These methods were not as precise as using the LPKF machine, resulting in measurements that were not perfectly matched. The measured insertion loss at the high band was 2.7 dB, and the reflection indicated some radiation in the off band, but the transmission was minimized, so the low band was off.

Overall, the measured results have slightly lower resonant frequencies and are not matched as well as the simulated results, but despite any differences compared to the simulations, the measured results show correct switching between the two frequency bands by accurately shifting or suppressing the off band. Copper was able to work as a Galinstan substitute to demonstrate the functionality of the filter.

The theoretical, simulated, and measured results were compared and are listed in Table 4.3, where f_L refers to the low band, f_H refers to the high band, IL is insertion loss, and BW is bandwidth. Although the measured results could have been further tuned, the resonant frequencies and quality factors were close to the expected values. As previously mentioned, for the measured LBC, the top black via in Figure 4.1(a) above g_L was left empty to obtain better measured results, closer to the simulated behavior. A wider bandwidth was needed because the external coupling was different in the fabricated filter, so it required inter-resonator tuning. This resulted in a Chebyshev response, but it displayed low insertion loss of 1.4 dB and a bandwidth similar to the

Table 4.3: Filter Summary for the Low to High Band Filter

	LBC ($N = 2$)			HBC ($N = 4$)		
	Theoretical	Simulated	Measured	Theoretical	Simulated	Measured
$\boldsymbol{f_L}$ *(GHz)*	4.8	4.7	4.6	-	-	-
$\boldsymbol{Q_{uL}}$	443	415	436	-	-	-
$\boldsymbol{IL}$ *(dB)*	~ 0	1.4	1.4	-	-	-
$\boldsymbol{BW}$ *(MHz)*	110	110	200	-	-	-
$\boldsymbol{FBW}$ *(%)*	2.3	2.3	4.3	-	-	-
$\boldsymbol{f_H}$ *(GHz)*	-	-	-	7.5	7.4	7.1
$\boldsymbol{Q_{uH}}$	-	-	-	431	405	349
$\boldsymbol{IL}$ *(dB)*	-	-	-	~ 0	1.5	3.6
$\boldsymbol{BW}$ *(MHz)*	-	-	-	170	180	240
$\boldsymbol{FBW}$ *(%)*	-	-	-	2.3	2.4	3.3

HBC bandwidth with only 40 MHz difference.

4.4 Discussion on Capabilities and Limitations

The low to high band filter incorporated several improvements on the design in Chapter 3, several of which depended on each other. To make a higher-order filter, the shape of the SIW cavities in the HBC was simplified for convenience, and the LBC required a higher-order filter to generate the TZ in the high band. The filter operated either in the low band or high band, demonstrated in both the simulated and measured results.

In simulations, the S-parameters displayed Butterworth filter responses, even after accounting for fabrication intolerances such as via distances, sizes,

and structures to work as channels for the liquid metal over the transmission lines. However, it was discovered that smaller vias could not hold the Galinstan. The high surface tension of the metal caused it to either bubble on the surface of the filter, or stick to the metal syringe tip over the substrate. Given a voltage potential, oxidation could cause the Galinstan to fall and take the shape of its container, such as a via. However, a well-developed oxide skin significantly lowers Q_u and increases loss, as shown in Chapter 3. Therefore, a tubing system for each via should be used to fill them with Galinstan. Nonetheless, the copper tape and wires worked as Galinstan substitutes to demonstrate the proof of concept.

There were a few reasons for the larger differences between the measured and simulated results. The wires soldered into the vias impacted the HBC because they slightly changed the sizes of the cavities, but the fabrication tolerances had a much larger effect on both configurations. As previously mentioned, there was mismatch in both configurations due to the CPWs. The milling bit had a pointed tip which caused the transmission lines to be thinner than 0.2 mm as designed. The copper tape also could not be perfectly placed 0.5 mm away from the junction to match the simulated design. Furthermore, addition of the copper tape resulted in more resonance, or higher return loss in stopband areas. For example, the measured results in Figure 4.10(b) shows resonance near 7.9 GHz, although there is no transmission. This means the copper tape was acting as an antenna at that frequency, where it was radiating.

Both the size of the transmission lines and addition of copper tape weakened external coupling into the filter and contributed to an impedance mismatch or higher loss, but the fabricated filters could switch between LBC and HBC with similar FBWs. Each configuration was used to demonstrate

turning off the appropriate frequency band by suppressing the insertion loss to over 14 dB, which exceeded the requirement of at least 10 dB. Chapter 5 adds more complexity by including the DBC, which aligns with the other two configurations.

4.5   Conclusion

The low to high band bandpass filter showed mode-reconfigurability between two unique frequency bands. The design expanded on capabilities from the dual to high band filter in Chapter 3. The low to high band filter used mode-shifting to turn off the low band, but it could also turn off the high band by generating a transmission zero. The filter in Chapter 3 demonstrated reversible switching between configurations with the use of liquid metal, therefore the design in Chapter 4 focused on the higher-order filter presented. The filter was simulated with Galinstan liquid metal, but the fabricated filter applied copper. Copper was used since Chapters 2 and 3 tested the experimental performance of Galinstan, and concluded it to be a good substitute for copper given that the oxide layer is not too thick. The results from the low to high band filter indicated that given a tubing system for the liquid metal, promising results could be expected for reversible switching between the frequency bands.

Chapter 5

Dual to Single Band Bandpass Filter

5.1 Introduction

The dual to single band bandpass filter switches between multiband operation to either low or high band operation, functioning in all the possible states. The states include dual band configuration (DBC), low band configuration (LBC), and high band configuration (HBC). Similarly to the filter in Chapter 4, it operates as second-order in the low band and fourth-order in the high band. The previous techniques to turn off either band are used; mode-shifting by filling vias with Galinstan turns off the low band, and generating a strategically placed transmission zero (TZ) with different external coupling turns off the high band. The simulated results accounted for Galinstan, while the measured results were tested with copper. The slightly different via placement from the filter in Chapter 4 allowed Butterworth bandpass filter responses for all three configurations.

5.2 Theory and Design

The theoretical background of the dual to single band filter is identical to the previous filters, therefore the design process intimately follows those in Chapters 3 and 4. The DBC and HBC build on the design in Chapter 3, while the LBC follows the design from Chapter 4. It demonstrates control of turning off each band and aligns the single band responses with the dual band response. To account for fabrication constraints and fit the single band responses inside the DBC frequency bands, different FBWs were used. This is unlike the filter in Chapter 4, which was designed for equal FBWs. Fabrication constraints for satisfying all three configurations were considered throughout the design process for the dual to single band filter.

The filter is displayed in Figure 5.1 in top and angled views. It has the top dielectric pieces for Galinstan channels 1-4, the copper boundaries to block cross-coupling between the input and output CPWs, and no SIW walls around the CPWs. Removing the vias that guide the CPW is a tradeoff; it reduces insertion loss, but makes the filter more vulnerable to cracking during fabrication and when connected for measurements. Table 5.1 shows which vias and channels need to be filled to activate the DBC, LBC, or HBC. The variables in Table 5.2 follow the same tuning trends as the filter in Chapter 4. The external coupling into the DBC and HBC are the same, so the corresponding variables are labeled $D_{D,H}$ and $D_{D,H}$'.

There are only slight differences between the filter layouts in Chapters 4 and 5. Some of the via radii were decreased in the dual to single band filter to change the internal gap sizes and include a DBC. The smaller vias included the two gray vias in the center and the four gray vias labeled v_{DBC}. The v_{DBC}

Table 5.1: Conditions of Each Configuration for the Dual to Single Band Filter

	DBC	LBC	HBC
Gray vias	Air	Air	Galinstan
Channels 1-2	Air	Galinstan	Air
Channels 3-4	Galinstan	Air	Galinstan

Table 5.2: Filter Tuning Trends for the Dual to Single Band Filter

Variable	**Value (mm)**	**Value too High**	**Value too low**
D_L	12.4	Decreases TZ frequency	Increases TZ frequency
D_L'	4.5	Creates ripple	Increases IL
$D_{D,H}$	1.8	Increases IL	Creates ripple
$D_{D,H}$'	5.0	Creates ripple	Increases IL
g_D	7.9	Increases BW	Decreases BW
g_L	6.2	Increases BW	Decreases BW
g_H	4.5	Increases BW	Decreases BW
g_H'	6.0	Increases BW	Decreases BW

vias could be used in the DBC to increase the resonant frequencies and cause them to align with the LBC and HBC resonant frequencies.

As previously, the top dielectric piece is shown on the right and hidden on the left to show the filter layout underneath. The characteristic impedance (Z_0) is not significantly affected at the boundary of the CPW and the filter, but again it was fine tuned with internal and external coupling after the addition of the top dielectric.

5.2.1   Dual Band Configuration

The unloaded quality factor (Q_u) of the DBC for the first mode was extracted from the same resonator used for the LBC, therefore it is discussed in Section
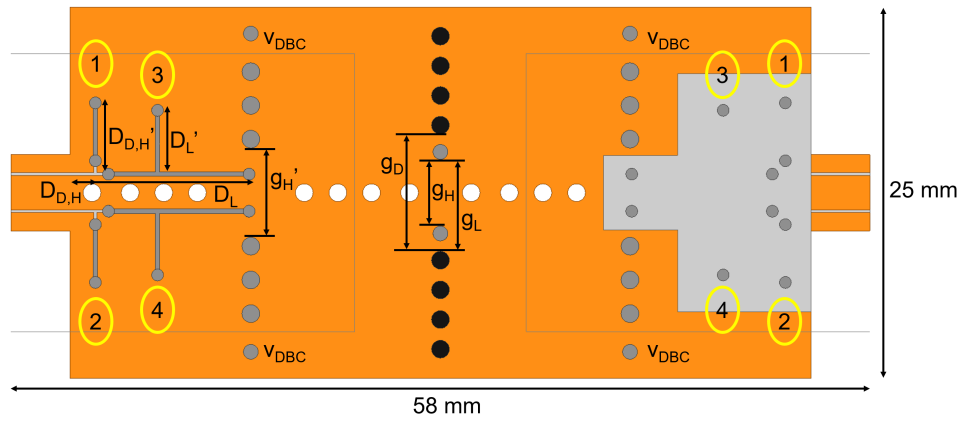
(a) Top view with liquid metal channels numbered 1-4
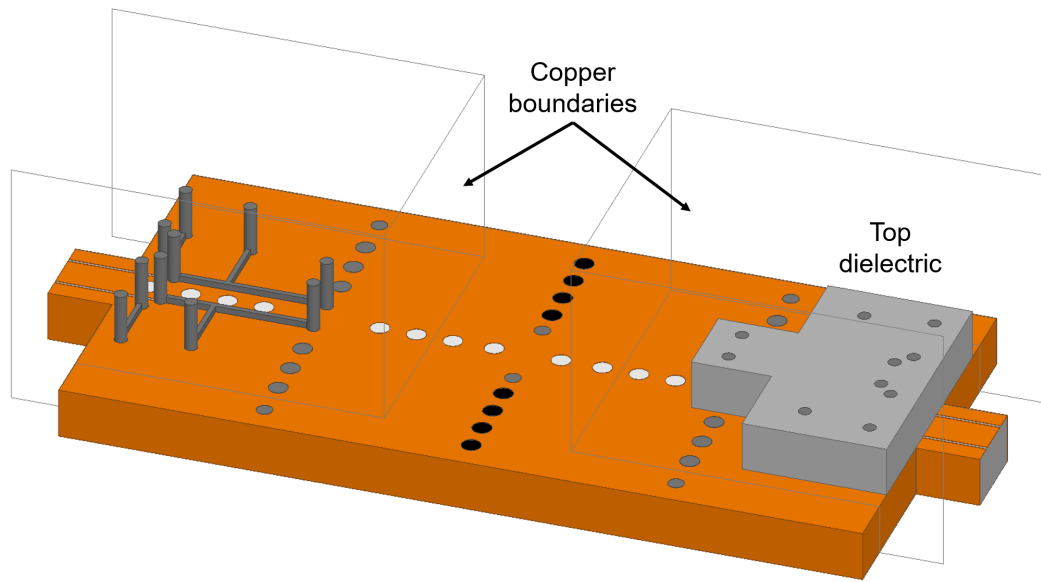
(b) Angled view

Figure 5.1: Layout of the dual to single band filter

5.2.2. They shared the same resonator because both configurations required square cavities. Similarly, Q_u for the second mode of the DBC shares the same resonator layout as the HBC. Therefore, it is discussed in Section 5.2.3 with a rectangular cavity.

The DBC was designed with wider bandwidths than the LBC and HBC partially due to the fabrication constraints. To make the bandwidths narrower would require weaker internal coupling, or a smaller gap between the two resonators. By referring to Figure 5.1(a), making the gap g_D smaller would move the black, copper plated vias closer to the gray vias. Moving them too close could result in cracking between the vias during fabrication. A spacing of 0.5 mm was considered acceptable, but a spacing of 0.7 mm was used for more tolerance.

Another limitation that caused wider bandwidths was the via radii. If the gray vias in the center were smaller, the black vias could be moved closer together, but the gray via was minimized only to a 1 mm diameter since it was designed to be filled with or emptied of liquid metal. Making the via too small could stop the Galinstan from flowing inside. Given the spacing and via radius requirements, the DBC was given wider bandwidths. Although possible to achieve equal bandwidths in simulation, from a practical standpoint it would depend on fabrication capabilities and material. However, the DBC successfully encompassed the LBC and HBC because the frequencies were well aligned. The FBWs of the DBC were twice as large as the single band FBWs.

Alignment of the high band frequencies from the DBC and HBC occurred naturally, especially due to the tolerance of the wide dual band response, but aligning the low band frequencies required a slight frequency shift. Originally, the DBC produced a low band of 4.6 GHz and needed to be increased to
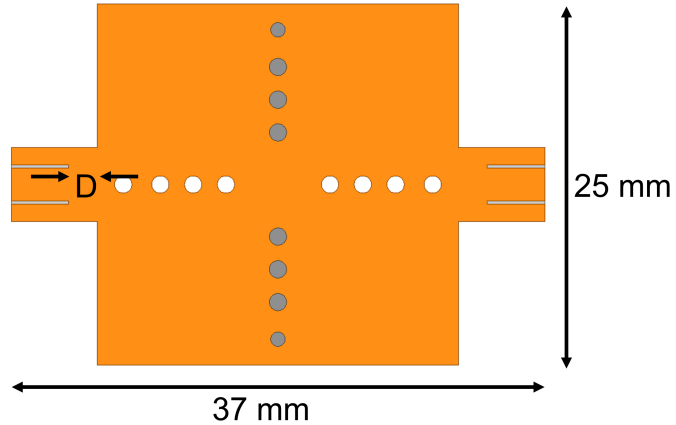
Figure 5.2: Layout of the LBC and low band of the DBC resonator

4.7 GHz to match the LBC. This was accomplished by filling the four gray vias marked v_{DBC}, making the volume smaller and resonant frequency higher.

5.2.2 Low Band Configuration

The LBC was characterized using Q_u, consistent with the previous designs in Chapters 3 and 4. The resonator layout for the LBC and low band of the DBC is shown in Figure 5.2. The gray vias were always empty, in the resonator since the low band utilized the full square structure. Weakly coupling required D to equal 2 mm, in other words the transmission lines stopped 2 mm away from the cavity. The CPWs were lengthened from 4 mm in the filter design from Figure 5.1, to 6 mm to ensure wave generation before entering the cavity.

A TZ was centered over the high band, as shown in Figure 5.3, to suppress the resonance to -40 dB. It followed the same behavior as discussed in Section 4.2.1, so the TZ was tuned using D_L. Then D_L' was used to tune the low band from a Chebyshev filter response to a Butterworth filter response, as indicated in Table 5.2.
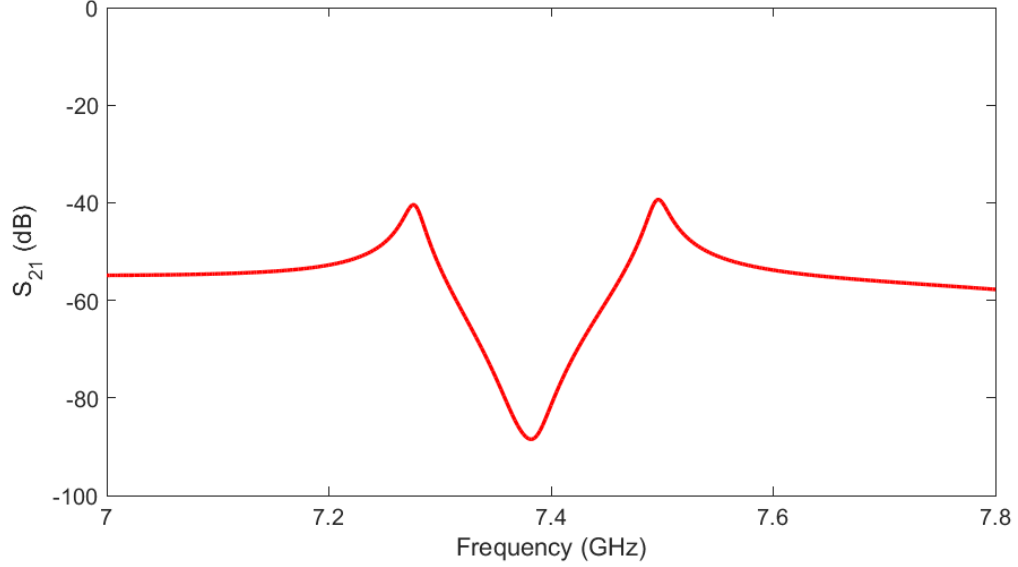
Figure 5.3: High band frequency of the LBC successfully suppressed

5.2.3   High Band Configuration

The same method described in Section 4.2.2 of adjusting the sizes of the cavities was used to combine the four poles in the HBC. The resonator layout for the HBC and high band of the DBC is shown in Figure 5.4, with D equal to 3.5 mm, or the CPW is 3.5 mm away from the cavity to insure weakly coupling into the resonator. The CPW outside of the resonator was lengthened to 6 mm, as in Section 5.2.2, to give the transmission lines more distance for excitation.

5.3   Simulation and Experimental Results

The fabricated filter is shown in Figure 5.5 without the top dielectric pieces and Galinstan. Similar occurrences were seen in the measured results of the filter compared to those in Chapter 4. The configurations are compared in Figure 5.6, and the simulated and measured results are compared in Figure 5.7.
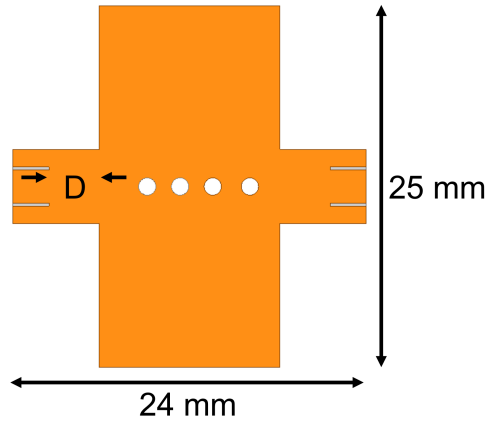
Figure 5.4: Layout of the HBC and high band of the DBC resonator

Differences in the measured results show low band responses resembling a Chebyshev filter and the high band in the HBC with slightly split poles. There is some return loss in the stopband, most likely due to resonance in the copper tape, but the reflection exceeds 10 dB in the passband. Both measured low band responses have ripples of over 10 dB return loss, although they were Chebyshev filter responses. For the measured LBC, the top gray via from Figure 5.1(a) above the gap g_L was left empty like in Chapter 4 for similar reasons. The different external coupling required adjustment of the inter-resonator coupling to better tune the filter. The via was left empty because it resulted in much lower loss, although the bandwidth was wider. The wider bandwidth produced cutoff frequencies that were almost identical to the DBC low band, therefore the modification was a better choice for the measured results.

The LBC high band was turned off to approximately -20 dB transmission. The high band in the DBC is well matched with insertion loss of 1.6 dB, and in the HBC the insertion loss is 2.7 dB. The separation of the poles resulted from the CPWs and soldered wires that affected the cavity sizes, as discussed
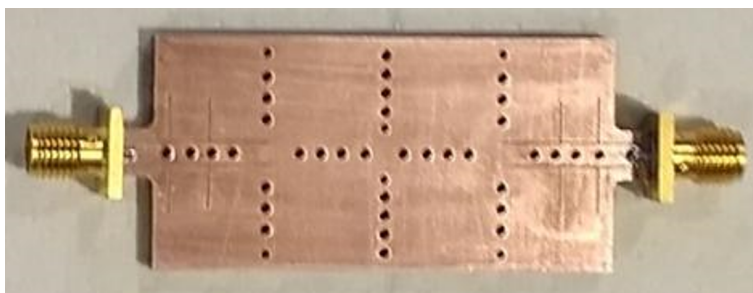
Figure 5.5: Fabricated dual to single band filter

in Chapter 4. As before, copper tape was used over the full transmission lines and the Galinstan would not be contained in the small vias. The measured results overall had lower resonant frequencies than the simulated results, but they correctly turned off the appropriate bands given their configuration, and displayed good insertion and return loss.

The theoretical, simulated, and measured results are listed in Table 5.3, where f_L and f_H refer to the low and high bands, respectively, IL is insertion loss, and BW is bandwidth. It was important for the resonant frequencies between the DBC and single band configurations to align, since the filter can turn off either band. Therefore, the DBC was designed for 4% FBW in the low band and 8% FBW in the high band. This allowed for the vias to be far enough apart for fabrication standards, given their radii. The LBC and HBC were designed to have half the FBW of the DBC for the single band responses to completely fit inside the dual band response. This resulted in a 2% FBW for the LBC and a 4% FBW for the HBC.

When comparing the DBC frequencies with the others, good agreement was seen, which is also shown in Figure 5.6. As previously stated, the fabricated LBC was given a larger bandwidth to reduce insertion loss, which resulted in matching bandwidths between the measured DBC and LBC. When observing
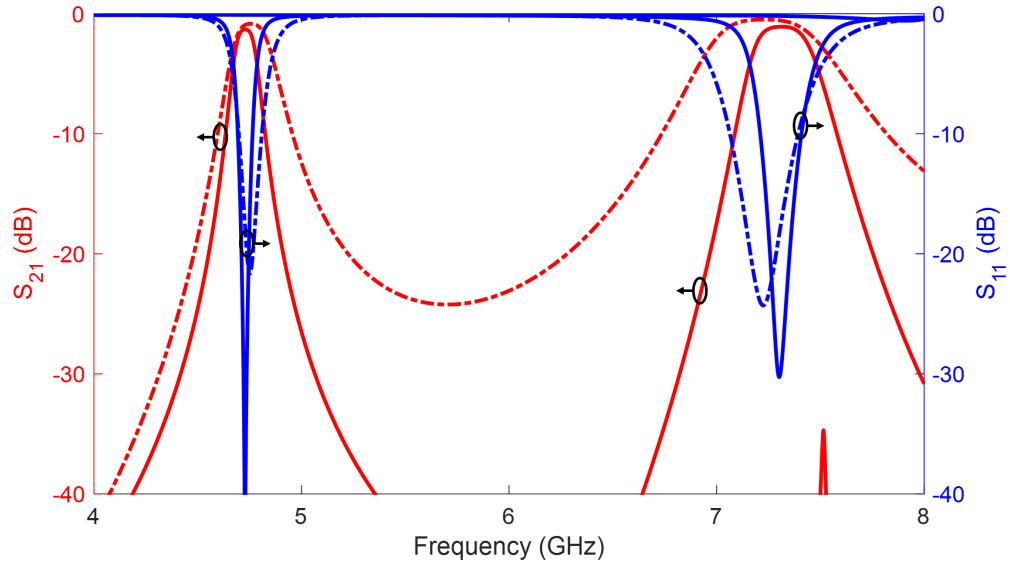
(a) Simulated results of the DBC (dot-dashed), LBC (solid) and HBC (solid)
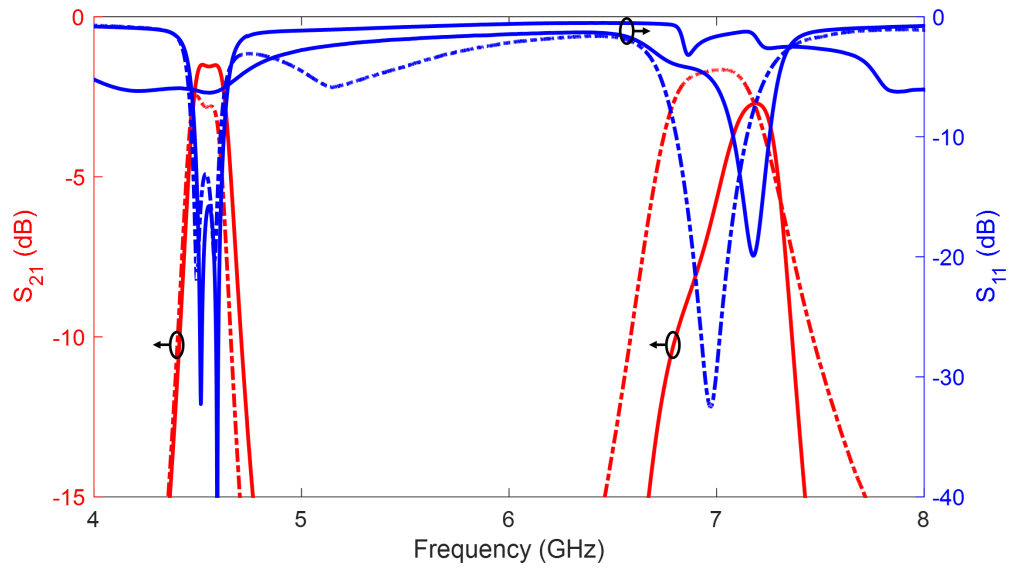
(b) Measured results of the DBC (dot-dashed), LBC (solid) and HBC (solid)

Figure 5.6: Comparison of the DBC, LBC, and HBC results of the dual to single band filter
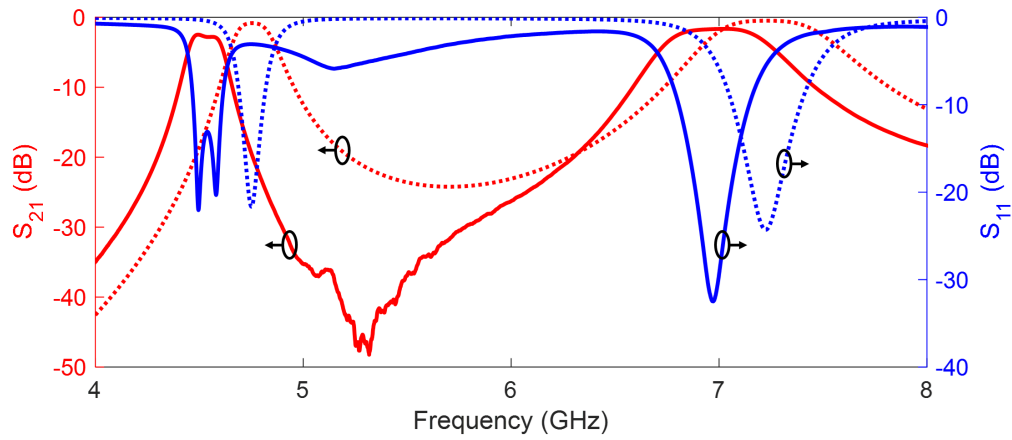
(a) DBC simulated (dotted) and measured (solid)
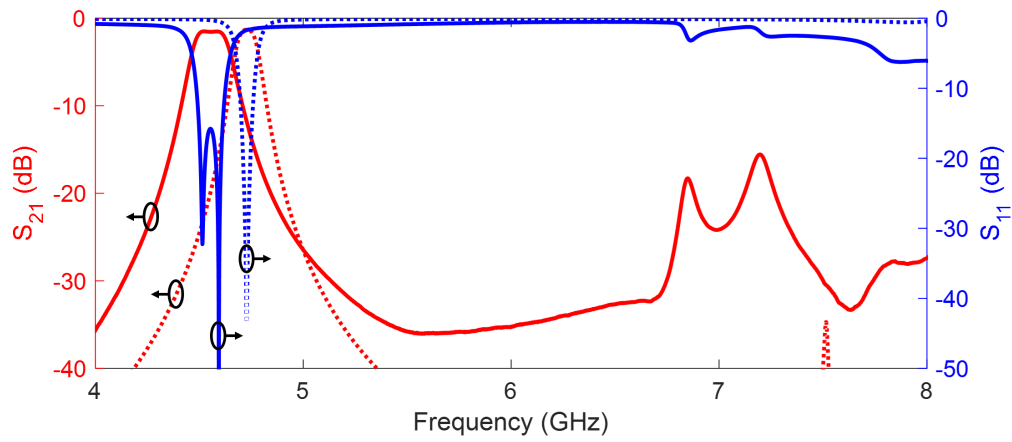
(b) LBC simulated (dotted) and measured (solid)
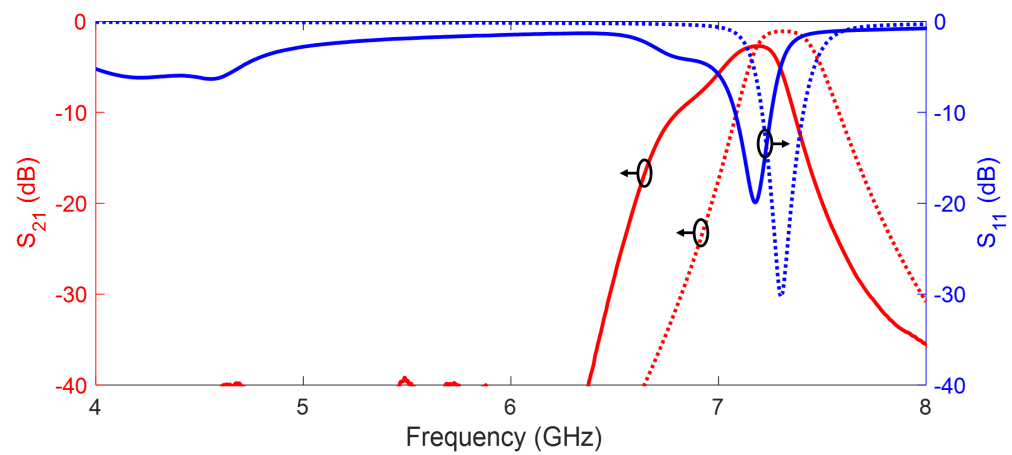
(c) HBC simulated (dotted) and measured (solid)

Figure 5.7: Comparison of the simulated and measured results of the dual to single band filter

Table 5.3: Filter Summary for the Dual to Single Band Filter

	DBC ($N = 2$)			LBC ($N = 4$)			HBC ($N = 4$)		
	Theoretical	Simulated	Measured	Theoretical	Simulated	Measured	Theoretical	Simulated	Measured
f_L *(GHz)*	4.8	4.8	4.5	4.8	4.7	4.6	-	-	-
Q_{uL}	443	416	416	443	416	416	-	-	-
IL *(dB)*	$\sim$0	0.8	2.8	$\sim$0	1.3	1.6	-	-	-
BW *(MHz)*	190	200	190	96	110	190	-	-	-
FBW *(%)*	4.0	4.2	4.2	2.0	2.3	4.1	-	-	-
f_H *(GHz)*	7.5	7.2	7.0	-	-	-	7.5	7.3	7.2
Q_{uH}	431	414	389	-	-	-	431	414	389
IL *(dB)*	$\sim$0	0.5	1.6	-	-	-	$\sim$0	1.1	2.7
BW *(MHz)*	600	600	560	-	-	-	300	320	310
FBW *(%)*	8.0	8.3	8.0	-	-	-	4.0	4.4	4.3

the quality factors, it should be noted that the DBC shared resonator structures with the LBC and HBC depending on the mode, therefore its Q_u values match with the other two configurations.

5.4 Discussion on Capabilities and Limitations

The dual to single band filter was closely related to the low to high band filter from Chapter 4. The filter applied the concept of mode-shifting from Chapter 3, but was higher-order and capable of generating a TZ over the high band like the filter in Chapter 4. It mainly differed from the filter in Chapter 4 was that it included the DBC centered over the other two configuration frequency bands. Due to fabrication constraints, the filters from Chapters 4 and 5 were

trade-offs of each other. One filter could be given equal FBWs, or bandwidths if made wide enough to reduce loss in the HBC, and the other filter was capable of multiband operation.

Accordingly, the design and challenges of the dual to single band filter imitate the filter in Chapter 4. The measured results of the low bands demonstrated ripples, although the insertion loss was very low. The Galinstan would not fill the vias, leading to the use of soldered wires to measure the HBC, which caused slightly incorrect cavity sizes and could have contributed to splitting of the poles. However, the main contributor of mismatch in the measured results was the fabricated CPWs. The transmission lines experienced the same reduction from the pointed milling bit. Nonetheless, the filter performed as required by controlling which frequency band to switch off, and accurately aligning the DBC modes with each single band configuration mode.

5.5 Conclusion

The dual to single band bandpass filter presented switched between three different configurations: dual band, low band, and high band. The design was closely related to the design in Chapter 4, however it expanded on the capabilities available. The dual to high band filter was higher-order, simulated with Galinstan liquid metal to accomplish switching. The measurements utilized copper since it was considered an acceptable replacement for Galinstan in Chapters 2 and 3. Therefore, the filter demonstrated mode-reconfigurability and promise for integrating Galinstan into the fabricated filter to offer reversible switching between the configurations.

Chapter 6

Conclusion

As the RF spectrum grows more crowded, frequency agile technology is in higher demand. This thesis presented three different mode-reconfigurable Butterworth bandpass filters for dynamic frequency access. The filters were designed to use nontoxic Galinstan liquid metal to enable reversible and repeatable switching between the filter configurations. Galinstan was chosen because it could be used to change the active transmission lines and resonator borders of SIW structures. Chapter 2 tested the radiation performance of Galinstan in comparison to copper with the use of monopole antennas. The Galinstan antenna behaved like copper in simulations and measurements in the lower portion of the SHF range where it operated. Previous research has also shown that Galinstan works similar to common solid metals in microwave frequency applications.

The three filters included dual to high band, low to high band, and dual to single band, where single band included both the low and high options. The dual to high band filter from Chapter 3 switched from first-order to second-order, respectively, by filling a diagonal line of vias that bordered two SIW cavities. The filter switched from a single square resonator to two triangular

resonators by applying mode-shifting to the first resonant frequency to overlap with the second resonant frequency for high band operation. The simulations and measurements displayed dual band configuration (DBC) and high band configuration (HBC) behavior, although the filter experienced more loss in the HBC due to the outer oxidation layer of the Galinstan.

The low to high band filter in Chapter 4, and dual to single band filter in Chapter 5, implemented several improvements of the dual to high band filter from Chapter 3. They were higher-order that switched from second-order in the low band and fourth-order in the high band by changing from square resonators to rectangular resonators, respectively. The HBC utilized the same concept from Chapter 3 of mode-shifting, but the low band configuration (LBC) was made possible by centering a transmission zero over the high band from changing the external coupling. The filters had very similar designs, but offered different benefits; the low to high band filter was easily designed for equal FBWs, and the dual to single band filter offered more frequency agility since it included all of the configurations. The simulated and measured results showed similar behavior and demonstrated control of turning off the appropriate frequency bands. However the measured results also showed Chebyshev behavior in the low bands and slight pole splitting in the high bands. This was because the vias of the filter were too small for the Galinstan to stay occupy. Copper wires were used in place of the Galinstan, as well as copper tape across the corresponding transmission lines to switch between the configurations. To incorporate liquid metal, the designs would require additional consideration, such as via tubing, before the simulated design could be fully tested.

Regarding actuation, Galinstan could be injected and removed manually with a syringe into and out of vias, unless they were too small in diameter.

Electrical actuation methods with tubing systems have high potential to move Galinstan through vias, if surrounded by certain carrier fluids such as NaOH.

This thesis presented three unique designs for mode-reconfigurable bandpass filters. To the author's knowledge, this is the first time this method is presented. The filters allow different combinations of switching between configurations: dual band, low band, and high band. To achieve reversible and repeatable operation, Galinstan liquid metal was chosen to enable switching. The designs were all simulated with Galinstan, and one of the filter measurements were taken with Galinstan to realistically demonstrate the idea. The liquid metal could be used to change the SIW cavity boundaries and filter-order, as well as the external excitation into the filters. Therefore, the mode-reconfigurable bandpass filters provide a promising method for spectrum agility in microwave frequency applications.

6.1 Future Direction

Ideally, combining the advantages of the low to high band and dual to single band filters would provide the best design. First, they require Galinstan to be moved into and out of their small vias which can be done by connecting tubes to the filters. Once there is good control in filling the vias, the top dielectric pieces made for Galinstan channels over the transmission lines could be remade with a transparent material such as PDMS or Teflon for convenience and better matching. Visibility through the top pieces would also be necessary to see if any residue is left behind on the transmission lines when they should be activated.

For better understanding of the behavior of Galinstan with electrical ac-

tuation, many experiments can be tested with varrying tube diameters, slug lengths, and input voltage conditions to find where smooth movement occurs. There are several research groups gathering information on the electrical actuation conditions required, also in regards to carrier fluid and tube coatings becuase of its importance.

Finally, designing the filter for equal FBWs while offering all three configurations would be challenging given fabrication constraints, but if good tubing systems are constructed to allow the Galinstan to move through smaller vias, that design would be much easier to accomplish. Overall, further testing on the actuation of Galinstan seems to be most important aspect in moving forward to make the designs possible through simulations, realistically attainable. Closed loops and good carrier fluids can help with movement, minimize oxidation, and optimize contact with other metals such as copper. Once the movement is thoroughly tested and successfully incorporated into designs, much more options can become available in terms of microwave devices, especially for the mode-reconfigurable filters by adjusting the cavities along with the transmission lines to correctly excite each configuration.

6.1.1   *Preliminary Work on Actuation Experiments with Galinstan*

An electrical actuation experiment similar to one in [92] was executed to test the responsive behavior of Galinstan to applied voltage. The metal was injected into deionized (DI) water then the cathode was placed in the water and the anode in the Galinstan, as shown in Figure 6.1. As the cathode approached the metal, the Galinstan repelled away until it formed into a large spherical droplet. Although the probes were able to shape the Galinstan, a voltage of 30 V was applied, and one probe had to be in contact with the Galinstan while
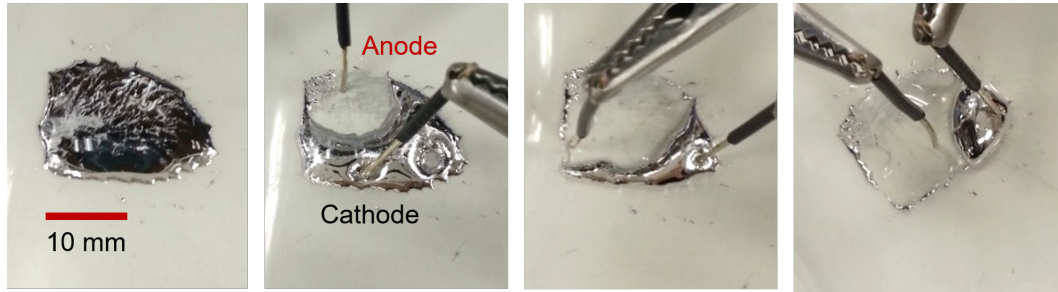
Figure 6.1: Galinstan droplet moving in DI water

Figure 6.2: Representation of a Galinstan slug in an electrolyte solution with an applied voltage potential

the other had to be very close to cause any movement. These conditions were most likely required for the following reasons: the droplet was (1) relatively large, (2) in an open area, (3) not immersed in an electrolyte solution, (4) experienced a steady DC voltage, and (5) was oxidized, which caused it to stick to the container and leave residue behind. Therefore, several follow-up tests were executed to further explore these issues.

Experiments resembling those in [72] and [65] were set up and the findings were relatively consistent. An electrolyte solution of 1% NaOH was injected into a 50 mm Teflon tube with an approximate inner diameter of 0.7 mm. A 10 mm long Galinstan slug was then injected into the tube so that it was surrounded by the NaOH. The experimental set-up is depicted in Figure 6.2, showing the applied voltage potential and expected direction of movement for the liquid metal.

First, a DC voltage was applied in the NaOH across either side of the tube, and was ranged from 1 to 20 V. The DC voltage caused the Galinstan
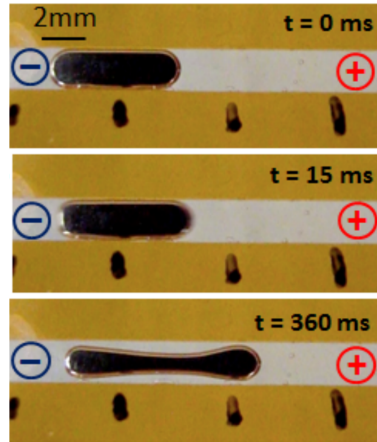
(a) DC voltage applied across the channel
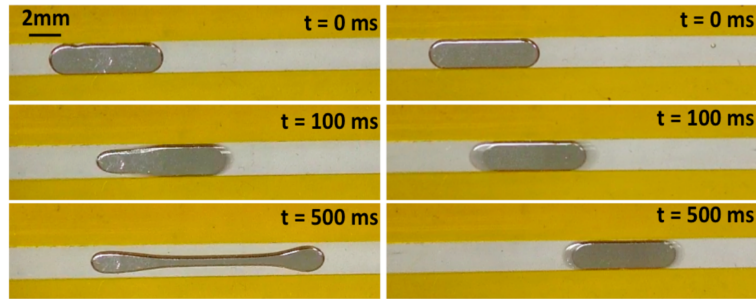
(b) Comparison of DC voltage (left) and AC voltage (right) applied across the channel

Figure 6.3: Examples of applying CEW to Galinstan (from [65])

to slightly move towards the cathode, then stop. As the voltage increased, the slug stretched further towards the cathode, but the other end stayed in place causing the slug to keep its position. When the voltage was turned off, the slug relaxed back into its original form almost in its original position. It did not move across the tube to the other end. This was consistent from the findings in [65], shown in Figure 6.3(a). This phenomenon could be useful in applications that require the metal to be stretched into and out of certain areas, acting like a switch, but not for those that require moving the metal through channels to another location.

That is why, as recommended in [65], an AC signal was considered. In Figure 6.3(b), the comparison between using DC voltage and AC voltage is demonstrated. The figure on the left has a DC voltage applied, so the slug stretches but the oxidation keeps it from moving forward. The figure on the right has an AC voltage applied and moves forward through the channel. Therefore, a DC voltage was first toggled; when it was turned on, the slug stretched forward towards the cathode then when it was turned off, it relaxed but at a slightly offset position forward. As the voltage was toggled, the slug slowly moved forward in jolting movements, showing potential for traveling across the tube. Then a function generator was used to apply a square wave, pulse, and sinusoidal wave. The peak-to-peak voltage was ranged from 1 to 8 V, the offset from 0 to 4 V, the frequency from 1 to 100 Hz, and the duty cycle was set to 50%.

The tests were able to create a back-and-forth movement of the slug, but not the smooth forward movement similar to what was demonstrated in [65] and shown in Figure 6.3(b). This was most likely due to the differences in the set-ups. The diameter of the channel used in [65] was 2mm, which was almost 300% larger, and therefore required different conditions to move the slug. Optimal input settings are required to give the Galinstan enough time to stretch forward on the positive cycle then remove the oxidation that causes the wetting on the negative cycle, as explained in [65].

The experiments showed some promise for certain applications, and challenges for others. Either way, it should be further noted that liquid metal actuation methods were generally tested for temporary operation since the research is relatively new. Some research studies tested longer lasting options, such as in [53] where each test underwent 100 trials to identify superior tube

coating and carrier fluid out of sixteen combinations. However, more research is needed for certainty in long term solutions for actuating Galinstan.

Bibliography

[1] M. Steer, *Microwave and RF design: A systems approach*. SciTech, 2013.

[2] D. M. Pozar, *Microwave engineering*. John Wiley&Sons Inc, 2012.

[3] P. Jarry and J. Beneat, *Advanced design techniques and realizations of microwave and RF filters*. John Wiley & Sons, 2008.

[4] I. Hunter, *Theory and design of microwave filters*, 48. IET, 2001.

[5] R. J. Cameron, C. M. Kudsia, and R. R. Mansour, *Microwave filters for communication systems*. Wiley-Interscience, 2007.

[6] U. D. of Commerce, *United states frequency allocations*, 2016. [Online]. Available: `https://www.ntia.doc.gov/page/2011/united-states-frequency-allocation-chart`.

[7] D. Psychogiou, R. Gómez-García, and D. Peroulis, "Recent advances in reconfigurable microwave filter design", in *Wireless and Microwave Technology Conference (WAMICON), 2016 IEEE 17th Annual*, IEEE, 2016, pp. 1–6.

[8] M. Esmaeili and J. Bornemann, "Novel tunable bandstop resonators in SIW technology and their application to a dual-bandstop filter with one tunable stopband", *IEEE Microwave and Wireless Components Letters*, vol. 27, no. 1, pp. 40–42, 2017.

[9] W. Y. Sam, Z. Zakaria, and M. A. Mutalib, "The investigation of reconfigurable SIW filter using varactor diodes", in *Antennas and Propagation (APCAP), 2016 IEEE 5th Asia-Pacific Conference on*, IEEE, 2016, pp. 167–168.

[10] B. You, S. Lu, L. Chen, and Q. J. Gu, "A half-mode substrate-integrated filter with tunable center frequency and reconfigurable bandwidth", *IEEE*

Microwave and Wireless Components Letters, vol. 26, no. 3, pp. 189–191, 2016.

[11] S. Sirci, J. D. Martinez, M. Taroncher, and V. E. Boria, "Varactor-loaded continuously tunable SIW resonator for reconfigurable filter design", in *Microwave Conference (EuMC), 2011 41st European*, IEEE, 2011, pp. 436–439.

[12] J. C. Bohorquez, B. Potelon, C. Person, E. Rius, C. Quendo, G. Tanne, and E. Fourn, "Reconfigurable planar SIW cavity resonator and filter", in *Microwave Symposium Digest, 2006. IEEE MTT-S International*, IEEE, 2006, pp. 947–950.

[13] H. Joshi, H. H. Sigmarsson, S. Moon, D. Peroulis, and W. J. Chappell, "High-q fully reconfigurable tunable bandpass filters", *IEEE transactions on microwave theory and techniques*, vol. 57, no. 12, pp. 3525–3533, 2009.

[14] T. Yang and G. M. Rebeiz, "Bandpass-to-bandstop reconfigurable tunable filters with frequency and bandwidth controls", *IEEE Transactions on Microwave Theory and Techniques*, 2017.

[15] N. M. Sbrockey, T. S. Kalkur, A. Mansour, H. Khassaf, H. Yu, M. Aindow, S. P. Alpay, and G. S. Tompa, "Switchable and tunable film bulk acoustic resonator fabricated using barium strontium titanate active layer and Ta2O5/SiO2 acoustic reflector", *Applied Physics Letters*, vol. 109, no. 5, p. 052 902, 2016.

[16] J. Ge and M. P. Fok, "Optically controlled fast reconfigurable microwave photonic dual-band filter based on nonlinear polarization rotation", *IEEE Transactions on Microwave Theory and Techniques*, vol. 65, no. 1, pp. 253–259, 2017.

[17] F. Wulschner, J. Goetz, F. R. Koessel, E. Hoffmann, A. Baust, P. Eder, M. Fischer, M. Haeberlein, M. J. Schwarz, M. Pernpeintner, *et al.*, "Tunable coupling of transmission-line microwave resonators mediated by an RF SQUID", *EPJ Quantum Technology*, vol. 3, no. 1, p. 10, 2016.

[18] C. Bockstiegel, Y. Wang, M. R. Vissers, L. F. Wei, S. Chaudhuri, J. Hubmayr, and J. Gao, "A tunable coupler for superconducting microwave resonators using a nonlinear kinetic inductance transmission line", *Applied Physics Letters*, vol. 108, no. 22, p. 222 604, 2016.

[19] K. Entesari, A. P. Saghati, V. Sekar, and M. Armendariz, "Tunable SIW structures: Antennas, VCOs, and filters", *IEEE Microwave Magazine*, vol. 16, no. 5, pp. 34–54, 2015.

[20] K. Bi, W. Zhu, M. Lei, and J. Zhou, "Magnetically tunable wideband microwave filter using ferrite-based metamaterials", *Applied Physics Letters*, vol. 106, no. 17, p. 173 507, 2015.

[21] S. Saeedi, J. Lee, and H. Sigmarsson, "Broadband implementation of tunable, substrate-integrated, evanescent-mode, cavity bandpass filters", in *Microwave Conference (EuMC), 2014 44th European*, IEEE, 2014, pp. 849–852.

[22] S. Saeedi, J. Lee, and H. H. Sigmarsson, "Tunable, high-Q, substrate-integrated, evanescent-mode cavity bandpass-bandstop filter cascade", *IEEE Microwave and Wireless Components Letters*, vol. 26, no. 4, pp. 240–242, 2016.

[23] D. Psychogiou, R. Gómez-García, and D. Peroulis, "Fully-reconfigurable bandpass/bandstop filters and their coupling-matrix representation", *IEEE Microwave and Wireless Components Letters*, vol. 26, no. 1, pp. 22–24, 2016.

[24] P. S. Carter, "Magnetically-tunable microwave filters using single-crystal yttrium-iron-garnet resonators", *IRE Transactions on Microwave Theory and Techniques*, vol. 9, no. 3, pp. 252–260, 1961.

[25] J. Nilsson and S. Riedel, *Electric circuits 9th*. Addison-Wesley, 2010.

[26] N. Instruments, *AWR design environment*, 2016.

[27] M. C. Collodo, A. Potocnik, A. Rubio Abadal, M. Mondal, M. Oppliger, and A. Wallraff, "Nonlinearly coupled superconducting lumped element resonators", in *APS Meeting Abstracts*, 2016.

[28] W. Liao, Q. Zhang, Y. Chen, S. Wong, and C. Caloz, "Compact reflection-type phaser using quarter-wavelength transmission line resonators", *IEEE Microwave and Wireless Components Letters*, vol. 25, no. 6, pp. 391–393, 2015.

[29] V. A. Sydoruk, F. Fiorani, S. Jahnke, and H.-J. Krause, "Design and characterization of microwave cavity resonators for noninvasive moni-

toring of plant water distribution", *IEEE Transactions on Microwave Theory and Techniques*, vol. 64, no. 9, pp. 2894–2904, 2016.

[30] J. Hopwood, S. Dennison, A. Chapman, W. Luo, and M. Lanagan, "Gas breakdown and plasma generation by dielectric resonator arrays", in *Plasma Science (ICOPS), 2016 IEEE International Conference on*, IEEE, 2016, pp. 1–1.

[31] N. Klein, C. Watts, S. M. Hanham, W. J. Otter, M. M. Ahmad, and S. Lucyszyn, "Microwave-to-terahertz dielectric resonators for liquid sensing in microfluidic systems", 2016.

[32] K. F. Raihn, P. J. Turner, and N. O. Fenzi, *Technique for designing acoustic microwave filters using lcr-based resonator models*, US Patent 9,525,393, 2016.

[33] R. Boudot, G. Martin, J.-M. Friedt, and E. Rubiola, "Frequency flicker of 2.3 ghz aln-sapphire high-overtone bulk acoustic resonators", *Journal of Applied Physics*, vol. 120, no. 22, p. 224 903, 2016.

[34] D. Electronics, *Scheme-it*, 2014.

[35] F. Cheng, X. Lin, X. X. Liu, K. J. Song, and Y. Fan, "A compact dual-band bandpass SIW filter", *Journal of Electromagnetic Waves and Applications*, vol. 27, no. 3, pp. 338–344, 2013.

[36] E. Arnieri and G. Amendola, "Analysis of substrate integrated waveguide structures based on the parallel-plate waveguide green's function", *IEEE Transactions on Microwave Theory and Techniques*, vol. 56, no. 7, pp. 1615–1623, 2008.

[37] J. H. Dang, R. C. Gough, A. M. Morishita, A. T. Ohta, and W. A. Shiroma, "A tunable X-band substrate integrated waveguide cavity filter using reconfigurable liquid-metal perturbing posts", in *Microwave Symposium (IMS), 2015 IEEE MTT-S International*, IEEE, 2015, pp. 1–4.

[38] D. Deslandes and K. Wu, "Design consideration and performance analysis of substrate integrated waveguide components", in *Microwave Conference, 2002. 32nd European*, IEEE, 2002, pp. 1–4.

[39] M. Rezaee and A. R. Attari, "Realisation of new single-layer triple-mode substrate-integrated waveguide and dual-mode half-mode substrate-integrated

waveguide filters using a circular shape perturbation", *IET Microwaves, Antennas & Propagation*, vol. 7, no. 14, pp. 1120–1127, 2013.

[40] S. Pinon, D. L. Diedhiou, A.-M. Gué, N. Fabre, G. Prigent, V. Conédéra, E. Rius, C. Quendo, B. Potelon, J.-F. Favennec, *et al.*, "Development of a microsystem based on a microfluidic network to tune and reconfigure RF circuits", *Journal of Micromechanics and Microengineering*, vol. 22, no. 7, p. 074 005, 2012.

[41] A. Anand, J. Small, D. Peroulis, and X. Liu, "Theory and design of octave tunable filters with lumped tuning elements", *IEEE Transactions on Microwave Theory and Techniques*, vol. 61, no. 12, pp. 4353–4364, 2013.

[42] K. Entesari and A. P. Saghati, "Fluidics in microwave components", *IEEE Microwave Magazine*, vol. 17, no. 6, pp. 50–75, 2016.

[43] J. H. Dang, R. C. Gough, A. M. Morishita, A. T. Ohta, and W. A. Shiroma, "Liquid-metal-based reconfigurable components for RF front ends", *IEEE Potentials*, vol. 34, no. 4, pp. 24–30, 2015.

[44] H. E. Ratcliffe, G. M. Swanson, and L. J. Fischer, "Human exposure to mercury: A critical assessment of the evidence of adverse health effects", *Journal of toxicology and environmental health*, vol. 49, no. 3, pp. 221–270, 1996.

[45] C. A. Smolders and E. M. Duyvis, "Contact angles; wetting and de-wetting of mercury: Part i. a critical examination of surface tension measurement by the sessile drop method", *Recueil des travaux chimiques des Pays-Bas*, vol. 80, no. 6, pp. 635–649, 1961.

[46] M. J. Assael, I. J. Armyra, J. Brillo, S. V. Stankus, J. Wu, and W. A. Wakeham, "Reference data for the density and viscosity of liquid cadmium, cobalt, gallium, indium, mercury, silicon, thallium, and zinc", *Journal of Physical and Chemical Reference Data*, vol. 41, no. 3, p. 033 101, 2012.

[47] N. B. Vargaftik, B. N. Volkov, and L. D. Voljak, "International tables of the surface tension of water", *Journal of Physical and Chemical Reference Data*, vol. 12, no. 3, pp. 817–820, 1983.

[48] J. Kestin, M. Sokolov, and W. A. Wakeham, "Viscosity of liquid water in the range - 8 C to 150 C", *Journal of Physical and Chemical Reference Data*, vol. 7, no. 3, pp. 941–948, 1978.

[49] L. C. Cadwallader, "Gallium safety in the laboratory", Idaho National Engineering and Environmental Laboratory, Idaho Falls, ID (US), Tech. Rep., 2003.

[50] M. D. Dickey, R. C. Chiechi, R. J. Larsen, E. A. Weiss, D. A. Weitz, and G. M. Whitesides, "Eutectic gallium-indium (EGaIn): A liquid metal alloy for the formation of stable structures in microchannels at room temperature", *Advanced Functional Materials*, vol. 18, no. 7, pp. 1097–1104, 2008.

[51] S.-Y. Tang, Y. Lin, I. D. Joshipura, K. Khoshmanesh, and M. D. Dickey, "Steering liquid metal flow in microchannels using low voltages", *Lab on a Chip*, vol. 15, no. 19, pp. 3905–3911, 2015.

[52] A. P. Saghati, J. S. Batra, J. Kameoka, and K. Entesari, "A microfluidically reconfigurable dual-band slot antenna with a frequency coverage ratio of 3:1", *IEEE Antennas and Wireless Propagation Letters*, vol. 15, pp. 122–125, 2016.

[53] C. Koo, B. E. LeBlanc, M. Kelley, H. E. Fitzgerald, G. H. Huff, and A. Han, "Manipulating liquid metal droplets in microfluidic channels with minimized skin residues toward tunable RF applications", *Journal of Microelectromechanical Systems*, vol. 24, no. 4, pp. 1069–1076, 2015.

[54] A. I. Abdulagatov, Y. Yan, J. R. Cooper, Y. Zhang, Z. M. Gibbs, A. S. Cavanagh, R. G. Yang, Y. C. Lee, and S. M. George, "Al2O3 and TiO2 atomic layer deposition on copper for water corrosion resistance", *ACS applied materials & interfaces*, vol. 3, no. 12, pp. 4593–4601, 2011.

[55] P. Herrasti, A. I. Del Rio, and J. Recio, "Electrodeposition of homogeneous and adherent polypyrrole on copper for corrosion protection", *Electrochimica acta*, vol. 52, no. 23, pp. 6496–6501, 2007.

[56] B. P. Singh, B. K. Jena, S. Bhattacharjee, and L. Besra, "Development of oxidation and corrosion resistance hydrophobic graphene oxide-polymer composite coating on copper", *Surface and Coatings Technology*, vol. 232, pp. 475–481, 2013.

[57] R. Haneda, H. Nishihara, and K. Aramaki, "Chemical modification of an alkanethiol self-assembled layer to prevent corrosion of copper", *Journal of the Electrochemical Society*, vol. 144, no. 4, pp. 1215–1221, 1997.

[58] A. P. Saghati, J. Batra, J. Kameoka, and K. Entesari, "A microfluidically-tuned dual-band slot antenna", in *Antennas and Propagation Society International Symposium (APSURSI), 2014 IEEE*, IEEE, 2014, pp. 1244–1245.

[59] A. T. Ohta, S. Guo, B. J. Lei, W. Hu, and W. A. Shiroma, "A liquid-metal tunable electromagnetic-bandgap microstrip filter", in *Wireless Information Technology and Systems (ICWITS), 2012 IEEE International Conference on*, IEEE, 2012, pp. 1–4.

[60] J. H. Dang, R. C. Gough, A. M. Morishita, A. T. Ohta, and W. A. Shiroma, "Liquid-metal-based phase shifter with reconfigurable EBG filling factor", in *Microwave Symposium (IMS), 2015 IEEE MTT-S International*, IEEE, 2015, pp. 1–4.

[61] T. Palomo and G. Mumcu, "Microfluidically reconfigurable metallized plate loaded frequency-agile RF bandpass filters", *IEEE Transactions on Microwave Theory and Techniques*, vol. 64, no. 1, pp. 158–165, 2016.

[62] D. J. Hartl, G. J. Frank, G. Huff, and J. W. Baur, "A liquid metal-based structurally embedded vascular antenna: I. concept and multiphysical modeling", *Smart Materials and Structures*, vol. 26, no. 2, p. 025 001, 2016.

[63] D. Rodrigo, L. Jofre, and B. A. Cetiner, "Circular beam-steering reconfigurable antenna with liquid metal parasitics", *IEEE transactions on antennas and propagation*, vol. 60, no. 4, pp. 1796–1802, 2012.

[64] J. D. Barrera and G. H. Huff, "A fluidic loading mechanism in a polarization reconfigurable antenna with a comparison to solid state approaches", *IEEE Transactions on Antennas and Propagation*, vol. 62, no. 8, pp. 4008–4014, 2014.

[65] R. C. Gough, A. M. Morishita, J. H. Dang, W. Hu, W. A. Shiroma, and A. T. Ohta, "Continuous electrowetting of non-toxic liquid metal for RF applications", *IEEE Access*, vol. 2, pp. 874–882, 2014.

[66]   A. M. Morishita, J. H. Dang, R. C. Gough, A. T. Ohta, and W. A. Shiroma, "A tunable amplifier using reconfigurable liquid-metal double-stub tuners", in *Wireless and Microwave Circuits and Systems (WMCS), 2015 Texas Symposium on*, IEEE, 2015, pp. 1–4.

[67]   R. C. Gough, J. H. Dang, A. M. Morishita, A. T. Ohta, and W. A. Shiroma, "Reconfigurable coupled-line bandpass filter with electrically actuated liquid-metal tuning", in *Microwave Conference (APMC), 2014 Asia-Pacific*, IEEE, 2014, pp. 932–934.

[68]   M. R. Khan, C. B. Eaker, E. F. Bowden, and M. D. Dickey, "Giant and switchable surface activity of liquid metal via surface oxidation", *Proceedings of the National Academy of Sciences*, vol. 111, no. 39, pp. 14 047–14 051, 2014.

[69]   M. R. Khan, C. Trlica, and M. D. Dickey, "Recapillarity: Electrochemically controlled capillary withdrawal of a liquid metal alloy from microchannels", *Advanced Functional Materials*, vol. 25, no. 5, pp. 671–678, 2015.

[70]   K. Doudrick, S. Liu, E. M. Mutunga, K. L. Klein, V. Damle, K. K. Varanasi, and K. Rykaczewski, "Different shades of oxide: From nanoscale wetting mechanisms to contact printing of gallium-based liquid metals", *Langmuir*, vol. 30, no. 23, pp. 6867–6877, 2014.

[71]   R. C. Gough, J. H. Dang, A. M. Morishita, A. T. Ohta, and W. A. Shiroma, "Frequency-tunable slot antenna using continuous electrowetting of liquid metal", in *Microwave Symposium (IMS), 2014 IEEE MTT-S International*, IEEE, 2014, pp. 1–4.

[72]   R. C. Gough, A. M. Morishita, J. H. Dang, M. R. Moorefield, W. A. Shiroma, and A. T. Ohta, "Rapid electrocapillary deformation of liquid metal with reversible shape retention", *Micro and Nano Systems Letters*, vol. 3, no. 1, p. 4, 2015.

[73]   X. Liu, L. P. B. Katehi, and D. Peroulis, "Non-toxic liquid metal microstrip resonators", in *Microwave Conference, 2009. APMC 2009. Asia Pacific*, IEEE, 2009, pp. 131–134.

[74]   D. Kim, R. G. Pierce, R. Henderson, S. J. Doo, K. Yoo, and J.-B. Lee, "Liquid metal actuation-based reversible frequency tunable monopole antenna", *Applied Physics Letters*, vol. 105, no. 23, p. 234 104, 2014.

[75] A. M. Morishita, C. K. Y. Kitamura, A. T. Ohta, and W. A. Shiroma, "Two-octave tunable liquid-metal monopole antenna", *Electronics Letters*, vol. 50, no. 1, pp. 19–20, 2014.

[76] C. K. Y. Kitamura, A. M. Morishita, T. F. Chun, W. G. Tonaki, A. T. Ohta, and W. A. Shiroma, "A liquid-metal reconfigurable yagi-uda monopole array", in *Microwave Symposium Digest (IMS), 2013 IEEE MTT-S International*, IEEE, 2013, pp. 1–3.

[77] A. M. Morishita, C. K. Y. Kitamura, A. T. Ohta, and W. A. Shiroma, "A liquid-metal monopole array with tunable frequency, gain, and beam steering", *IEEE Antennas and Wireless Propagation Letters*, vol. 12, pp. 1388–1391, 2013.

[78] A. P. Saghati, J. Batra, J. Kameoka, and K. Entesari, "A microfluidically-switched CPW folded slot antenna", in *Antennas and Propagation Society International Symposium (APSURSI), 2014 IEEE*, IEEE, 2014, pp. 557–558.

[79] A. P. Saghati, J. S. Batra, J. Kameoka, and K. Entesari, "Miniature and reconfigurable CPW folded slot antennas employing liquid-metal capacitive loading", *IEEE Transactions on Antennas and Propagation*, vol. 63, no. 9, pp. 3798–3807, 2015.

[80] G. J. Hayes, J.-H. So, A. Qusba, M. D. Dickey, and G. Lazzi, "Flexible liquid metal alloy (EGaIn) microstrip patch antenna", *IEEE Transactions on Antennas and Propagation*, vol. 60, no. 5, pp. 2151–2156, 2012.

[81] A. P. Saghati, S. B. Kordmahale, J. Kameoka, and K. Entesari, "A reconfigurable quarter-mode substrate integrated waveguide cavity filter employing liquid-metal capacitive loading", in *Microwave Symposium (IMS), 2015 IEEE MTT-S International*, IEEE, 2015, pp. 1–3.

[82] A. P. Saghati, J. S. Batra, J. Kameoka, and K. Entesari, "A miniaturized microfluidically reconfigurable coplanar waveguide bandpass filter with maximum power handling of 10 watts", *IEEE Transactions on Microwave Theory and Techniques*, vol. 63, no. 8, pp. 2515–2525, 2015.

[83] W. G. Tonaki, W. Hu, A. T. Ohta, and W. A. Shiroma, "A reconfigurable, liquid-metal-based low-pass filter with reversible tuning", in *Wireless Symposium (IWS), 2013 IEEE International*, IEEE, 2013, pp. 1–3.

[84] S. Guo, B. J. Lei, W. Hu, W. A. Shiroma, and A. T. Ohta, "A tunable low-pass filter using a liquid-metal reconfigurable periodic defected ground structure", in *Microwave Symposium Digest (MTT), 2012 IEEE MTT-S International*, IEEE, 2012, pp. 1–3.

[85] M. Li, B. Yu, and N. Behdad, "Liquid-tunable frequency selective surfaces", *IEEE Microwave and wireless components letters*, vol. 20, no. 8, pp. 423–425, 2010.

[86] G. Mumcu, A. Dey, and T. Palomo, "Frequency-agile bandpass filters using liquid metal tunable broadside coupled split ring resonators", *IEEE Microwave and Wireless Components Letters*, vol. 23, no. 4, pp. 187–189, 2013.

[87] N. Vahabisani, S. Khan, and M. Daneshmand, "Microfluidically reconfigurable rectangular waveguide filter using liquid metal posts", *IEEE Microwave and Wireless Components Letters*, vol. 26, no. 10, pp. 801–803, 2016.

[88] S. Zhu, J.-H. So, R. Mays, S. Desai, W. R. Barnes, B. Pourdeyhimi, and M. D. Dickey, "Ultrastretchable fibers with metallic conductivity using a liquid metal alloy core", *Advanced Functional Materials*, vol. 23, no. 18, pp. 2308–2314, 2013.

[89] E. Palleau, S. Reece, S. C. Desai, M. E. Smith, and M. D. Dickey, "Self-healing stretchable wires for reconfigurable circuit wiring and 3D microfluidics", *Advanced Materials*, vol. 25, no. 11, pp. 1589–1592, 2013.

[90] C. Ladd, J.-H. So, J. Muth, and M. D. Dickey, "3D printing of free standing liquid metal microstructures", *Advanced Materials*, vol. 25, no. 36, pp. 5081–5085, 2013.

[91] T. Liu, P. Sen, and C.-J. Kim, "Characterization of nontoxic liquid-metal alloy galinstan for applications in microdevices", *Journal of Microelectromechanical Systems*, vol. 21, no. 2, pp. 443–450, 2012.

[92] L. Sheng, J. Zhang, and J. Liu, "Liquid metal transformers", *arXiv preprint arXiv:1402.1727*, 2014.

[93] C. Karcher, V. Kocourek, and D. Schulze, "Experimental investigations of electromagnetic instabilities of free surfaces in a liquid metal drop", in

International Scientific Colloquium, Modelling for Electromagnetic Processing, 2003, pp. 105–110.

[94] ANSYS, *Electronics Desktop*, 2015.

[95] F. T. Ulaby, E. Michielssen, and U. Ravaioli, *Fundamentals of applied electromagnetics 6e*. Prentice Hall, 2010.

[96] A. B. Constantine, *Antenna theory: Analysis and design*. John wiley & sons, 2005.

[97] S. Ramo, J. R. Whinnery, and T. Van Duzer, *Fields and waves in communication electronics*. John Wiley & Sons, 2008.

[98] S. N. McClung, S. Saeedi, and H. H. Sigmarsson, "Single-mode-dual-band to dual-mode-single-band bandpass filter with liquid metal", in *Wireless and Microwave Technology Conference (WAMICON), 2017 IEEE 18th*, IEEE, 2017, pp. 1–4.

[99] D. G. Swanson, "Narrow-band microwave filter design", *IEEE Microwave magazine*, vol. 8, no. 5, pp. 105–114, 2007.